Co-planar Optoelectrowetting (OEW) Device for Droplet Manipulation

Jodi Loo

Electrical Engineering and Computer Sciences
University of California at Berkeley

Technical Report No. UCB/EECS-2020-213
http://www2.eecs.berkeley.edu/Pubs/TechRpts/2020/EECS-2020-213.html

December 17, 2020

Co-planar Optoelectrowetting (OEW) Device for Droplet Manipulation

By

Jodi Tsu-An Loo

A dissertation submitted in partial satisfaction of the

requirements for the degree of

Doctor of Philosophy

in

Engineering – Electrical Engineering and Computer Sciences

in the

Graduate Division

of the

University of California, Berkeley

Committee in charge:

Professor Ming C. Wu, Chair
Professor Ana Claudia Arias
Professor Liwei Lin

Fall 2020

Co-planar Optoelectrowetting (OEW) Device for Droplet Manipulation

Abstract

Co-planar Optoelectrowetting (OEW) Device for Droplet Manipulation

by

Jodi Tsu-An Loo

Doctor of Philosophy in Engineering – Electrical Engineering and Computer Sciences

University of California, Berkeley

Professor Ming C. Wu, Chair

Lab-on-a-chip technologies have seen great advances and development over the past few decades in addressing applications such as biochemical analysis, pharmaceutical development, and point-of-care diagnostics. Miniaturization of biochemical operations performed on lab-on-a-chip platforms benefit from reduced sample, reagent and waste volumes as well as increased parallelization and automation. This enables more cost-effective operations along with higher throughput and sensitivity for faster and more efficient analysis and detection.

The research presented in this dissertation focuses on progress achieved in optoelectrowetting (OEW), an optofluidic technology that allows for the manipulation of discrete droplets. In this work, we present a novel co-planar OEW device for droplet manipulation, which allows for faster droplet movement and a wider range of system integration capabilities than previous generations of OEW devices. First, we discuss the theory and design of the co-planar OEW device and present an optimization model that also accounts for the OEW effect on the droplet's contact line. The OEW effect is experimentally verified by inspection of the contact angle of the droplet. We demonstrate individual and parallel droplet movement along with basic operations such as droplet merging and mixing with actuation speeds of up to 4.5 cm/s on the co-planar OEW device. Next, we investigate how experimental parameters such as applied voltage, frequency, and light intensity can be tuned for optimized OEW operation. Lastly, to showcase the co-planar OEW's advantage for more flexible input/output configurations, we integrate the co-planar OEW platform with a droplet-on-demand dispensing system to form large scale droplet arrays with each individual droplet acting as its own unique microreaction chamber. Overall, the co-planar OEW device expands the ability for OEW technologies to serve as a versatile and adaptable lab-on-a-chip platform for a variety of biological and chemical applications.

To my family:

my sister Jenny
&
my parents Dr. Robert & Mrs. Mabel Loo

Table of Contents

Abstract **1**
Table of Contents ..... **ii**
List of Figures and Tables ..... **v**
Acknowledgments ..... **viii**
1 Introduction **1**
2 Optoelectrowetting (OEW) Principles **5**
2.1 Introduction 5
2.2 Electrowetting 6
2.2.1 How to Move a Droplet 7
2.3 Electrowetting on Dielectric 9
2.4 Optoelectrowetting Principle 11
2.4.1 Traditional OEW Circuit Model 13
2.5 Fabrication of the Traditional OEW Device 16
2.6 Droplet Movement Demonstration 16
2.7 Summary 17
3 Co-planar OEW Design & Optimization **18**
3.1 Introduction 18
3.2 Co-planar OEW Design 19
3.3 Co-planar OEW Circuit Model 21
3.4 Metal Mesh Grid Analysis 26
3.4.1 Metal Mesh Grid 28
3.4.2 Metal Mesh Grid Resistance 29
3.4.3 Metal Mesh Grid Geometry 32
3.4.4 Minimum Droplet Size Requirement 32
3.5 Goals for Optimization 34
3.5.1 Dielectric Layer 34
3.5.2 Photoconductor Layer 36

3.6 Summary 38
4 OEW Contact Angle Analysis 39
4.1 Introduction 39
4.2 Contact Angle 39
4.3 Contact Angle Experiments 40
4.3.1 Hydrophobic Coating 41
4.3.2 Traditional OEW vs. Co-planar OEW 41
4.3.3 Water vs. Surfactant 41
4.3.4 Oil vs. Air 44
4.4 Contact Angle vs. Frequency 48
4.5 Contact Angle Optimization 51
4.5.1 Material Properties 51
4.5.2 Experimental Parameters 51
4.6 Summary 54
5 Co-planar OEW Device Characterization 55
5.1 Introduction 55
5.2 Fabrication & Methods 55
5.2.1 Sample Preparation 56
5.2.2 Experimental Setup 57
5.3 Droplet Actuation Demonstration 57
5.4 Force to Speed Comparison 60
5.5 Frequency Analysis 62
5.6 Voltage Analysis 64
5.7 Light Intensity Analysis 66
5.8 Summary 69
6 Co-planar OEW Manipulation & System Integration 70
6.1 Introduction 70
6.2 Droplet Manipulation Capabilities 71
6.3 Preliminary Integration Example 73
6.4 From Above Droplet Dispensing Capabilities 74
6.5 Large Scale Array 77
6.6 Dilution Capabilities 81
6.7 Summary 85
7 Conclusion 86

Appendix A Optoelectrowetting (OEW) Fabrication 88
A.1 Traditional OEW Device Fabrication 88
A.2 Traditional OEW Top Cover Fabrication 88
A.3 Co-planar OEW Device Fabrication 89
References 90

List of Figures and Tables

Figure 1.1 The two paradigms of lab-on-a-chip microfluidic systems 2
Figure 1.2 Schematic of a traditional optoelectrowetting (OEW) device 3
Figure 1.3 Schematic of the novel co-planar OEW device 4
Figure 2.1 Various digital microfluidics technologies 5
Figure 2.2 The principle of electrowetting 7
Figure 2.3 How to move a droplet using electrowetting 8
Figure 2.4 Electrowetting-on-dielectric (EWOD) schematic 10
Figure 2.5 Traditional optoelectrowetting (OEW) device 12
Figure 2.6 Traditional OEW circuit model 13
Figure 2.7 Traditional OEW droplet movement 17
Figure 3.1 Co-planar optoelectrowetting (OEW) schematic 19
Figure 3.2 From traditional to co-planar OEW device 20
Figure 3.3 Co-planar OEW circuit model 21
Figure 3.4 Metal mesh grid top view 22
Figure 3.5 Co-planar OEW block diagram circuit model 25
Figure 3.6 Normalized force of the co-planar OEW device 27
Figure 3.7 Fill factor effect on co-planar OEW normalized force 28
Figure 3.8 Resistance through a solid 29
Figure 3.9 N x N finite resistor grid 30
Figure 3.10 Effective resistance of metal mesh grid 30
Figure 3.11 Metal grid resistance comparison 31
Figure 3.12 Minimum droplet size requirement 33
Figure 3.13 Minimum droplet volumes in relation to the OEW force 33
Figure 3.14 Force of co-planar OEW device vs. oxide thickness 35
Figure 3.15 Dielectric breakdown 36

Figure 3.16 Force of co-planar OEW device vs. a-Si thickness 37
Figure 4.1 Initial contact angle for the co-planar OEW with CYTOP coating 42
Figure 4.2 Aqueous & surfactant droplet contact angle comparisons on the co-planar OEW device 43
Figure 4.3 Droplet contact angle comparisons for the traditional OEW device in air vs. silicone oil 45
Figure 4.4 Surfactant droplet contact angle comparisons on the traditional OEW device 46
Figure 4.5 Droplet contact angle comparisons on the co-planar OEW device 47
Figure 4.6 Contact angle models for traditional and co-planar OEW devices 49
Figure 4.7 Contact angles of droplets under 1 kHz and 100 kHz 49
Figure 4.8 Droplet contact angle vs. frequency with and without background light in air & silicone oil 50
Figure 4.9 Contact angle studies with changing brightness and contrast ratios 53
Figure 5.1 Fabrication process of the co-planar OEW device 56
Figure 5.2 Co-planar OEW device droplet movement demonstrations 58
Figure 5.3 Co-planar OEW device parallel droplet movement demonstrations 58
Figure 5.4 Co-planar OEW droplet movement motion overlay images 59
Figure 5.5 Co-planar OEW pitch size comparison 61
Table 5.1 Co-planar OEW pitch sizes with corresponding maximum droplet speeds 61
Figure 5.6 OEW operational frequency range 62
Figure 5.7 Co-planar OEW optimal frequency range 63
Figure 5.8 Co-planar OEW device droplet speeds with varying applied voltages 65
Figure 5.9 Projector light source spectrum 66
Figure 5.10 Neutral density filter schematic 67
Figure 5.11 Co-planar OEW speed vs. frequency for various light intensities 68
Figure 6.1 Co-planar OEW device system integration concept schematic 70
Figure 6.2 Droplet merging on co-planar OEW device 71
Figure 6.3 Side view of droplet merging on co-planar OEW device 72
Figure 6.4 Sequential droplet merging on co-planar OEW device 72
Figure 6.5 Droplet merging and mixing in parallel 73

Figure 6.6 Microfluidic and extraction from above prototype demonstration 74
Figure 6.7 Co-planar OEW setup schematic with droplet-on-demand dispenser 75
Figure 6.8 Droplet-on-demand dispensing capabilities 76
Figure 6.9 "Cal" demonstration 77
Figure 6.10 10 x 10 droplet array on co-planar OEW sequence 78
Figure 6.11 Completed 10 x 10 droplet array on co-planar OEW device 78
Figure 6.12 17 x 12 droplet array on co-planar OEW device 79
Figure 6.13 Formation of 20 x 20 droplet array on co-planar OEW 80
Figure 6.14 Completed 20 x 20 array on co-planar OEW device 80
Figure 6.15 Basic dilution demonstration with differing final volumes 82
Figure 6.16 Basic dilution demonstration with same final volumes 83
Figure 6.17 10 droplet 10% resolution dilution array 84
Figure 6.18 5 x 10 dilution array on co-planar OEW device with 2% resolution 84

Acknowledgments

"The correct analogy for the mind is not a vessel that needs filling, but wood that needs igniting — no more — and then it motivates one towards originality and instills the desire for truth."
–Plutarch*, "On Listening"*

After spending ten years at the University of California, Berkeley (UC Berkeley) to pursue my undergraduate and graduate degrees in Electrical Engineering & Computer Sciences (EECS), I have much to be thankful for and many people to thank for this journey. People that I have encountered in my life have all helped shaped who I am today and aspire to be.

First and foremost, I want to express my utmost gratitude to my advisor Professor Ming Wu for his mentorship, believing in me, and giving me the freedom and opportunity to explore various research problems over the years. His vast scientific knowledge and insight has been inspiring and has helped me grow as a researcher and philosopher during my time at UC Berkeley. It has been an absolute pleasure to be part of the Integrated Photonics Laboratory and to learn from all the various, often international, members throughout the years. I am grateful to all of the lab and office mates that have come and gone for their knowledge, perspectives, and conversations on science, optics, engineering, and life. I would like to thank Shao Ning Pei for his mentorship in optofluidics during the first months of my PhD studies and Jose Camacho for the opportunity to mentor an undergraduate student. In addition, I would like to give a shout out to group members Jean-Etienne and Johannes for allowing me to accompany them on cycling and hiking adventures outside of lab and being patient as I climbed hills and mountains at my own pace. I would also like to thank the additional members of my dissertation and qualifying exam committees, Professor Ana Claudia Arias, Professor Liwei Lin and Professor Luke Lee. Their feedback and support have been invaluable especially while finishing up my PhD work. Furthermore, I would like to thank the National Science Foundation Graduate Research Fellowship Program for its financial support during my graduate studies, which also afforded me the freedom to pursue projects of personal interest.

I am appreciative for all ten years spent at UC Berkeley and the EECS department. Attending UC Berkeley has taught me how to be independent while also enlargening my worldview with its diverse offerings and student body. I could not have gotten through my graduate studies without my graduate school cohort, "Gossip Girls" (named after one of my favorite TV shows from high school). Akshay, Benjamin, Carlos, JP, and Lety have been there since the first day of graduate school. Without even knowing me on that first day, they spontaneously organized a birthday dinner for me, and the rest is history. I am grateful for the laughs we shared and being able to rely on them through the thick and thin of graduate school. There are many other graduate school friends such as Andy, Adair, Dan, Dom, Korok, Nishita, Thomas, Varun, and Zain, to name a few, that I attribute my graduate student work-life balance to and I appreciate the many lunches, Berkeley shenanigans and time we have spent together. In addition, exercising, staying active, and getting outdoors has been an integral part of my wellbeing during graduate school. I am

also proud to have expanded my horizons by trying new sports and meeting friends like Sofia and Tiara to workout with and go on cycling and skiing adventures.

My Berkeley experience has also been shaped by the many friends from my undergraduate days at Cal including, but not limited to, Adam, Allan, Anne, Becca, Eric, Jiann, Jody, Joyce, Lu, Matt, Namkyu, Paul, Raymond, Roschelle, Victor, and Weisi. I cherish the fond memories formed during our undergraduate days, which made staying at UC Berkeley for my graduate studies an easy decision. I am very thankful for our continual friendship throughout these years and for their understanding of my intermittent absences yet still keep in touch while being preoccupied with graduate work and research.

I am always grateful for my childhood friends and proud of what they, too, have accomplished. Friends like Erin, Noorean, Patty, Sarah, and Stephanie were probably the best memories of high school. They have also pursued professional or PhD degrees, which is incredibly inspiring. I also want to thank childhood and neighborhood friends Ashley, Beverley, and Carolyn for their friendship and support over the years. Although all of them live in various parts of the country, I am glad that we are able to still keep in touch after all of these years. I am beyond excited to see where life takes all of us.

Finally, I would not be where I am today if it were not for my family. I have them to thank because of their hard work, sacrifices, and determination to provide an enriching and comfortable life for us. They have provided me with tools to succeed and unwavering support to do what I choose—a privilege I do not take lightly. I thank my father, Robert, for instilling his love for research, science and engineering in me, which is the fire that started it all. I also thank him for introducing me to tennis when I was young and for playing with me throughout all these years. I thank my mother, Mabel, for her knowledge of finance and teaching me the importance of budgeting, investing and financial independence from a young age. She has also been one of the best travel companions, always open to exploring the reaches of the earth, and I hope we can continue to travel the world together. But more importantly, without my parents, I would not have the joy of knowing my sister. My autistic sister, Jenny, is the inspiration and motivation for all that I do, and I am especially blessed to have her in my life. As of the year 2020, 1 in 54 children are identified with the autism spectrum disorder (ASD), up from 1 in 150 when I was growing up. To this day, there are still no known causes of autism or single standard treatment for autism. Aiding those with ASD involve a variety of therapies and interventions starting early in life to give them the ability to function as normally as possible. Growing up and living with my sister has had an immeasurable impact on who I am and the reason I chose to pursue this PhD dissertation project. I hope the work and research that I present in this dissertation and that I will continue to pursue throughout my career enable new findings to diagnose, treat, and give insight into diseases such as ASD.

I am not only filled with extreme gratitude and knowledge gained from my academic career and PhD experience, but I am also ignited with a passion to continue learning, teaching, and exploring. I hope the fire that has been kindled lasts throughout my entire life and can also be spread to others.

1 Introduction

At the time of this writing in the year 2020, a global pandemic is underway due to the severe acute respiratory syndrome coronavirus 2 (SARS-CoV-2), which causes the COVID-19 disease. The last major pandemic to be faced by humankind was the 1918 influenza pandemic caused by the H1N1 virus, so only a very small percentage of today's population may have memory of living through a widespread health crisis to this scale [1]. However, from a scientific point-of-view, conquering the COVID-19 disease is not very different from other diseases. Public health guidelines to slow and lessen the spread of the virus across our populations buy researchers time to discover treatments and vaccines to give our bodies the means and knowledge to combat the virus, preventing the virus to find willing hosts for it to continue to survive [1]-[3].

Despite a vast amount of biological and chemical discoveries over the past century, many traditional methods of biological and chemical experimentation are still tedious mechanical, and often manual, operations done in bulk [4]-[6]. The vast majority of these assays are therefore time consuming, inefficient (due to large batch-to-batch variation), low throughput, and high cost. The ability to automate and miniaturize these operations have the potential to increase throughput, increase efficiency due to smaller reaction volumes, reduce chemicals and reagents used, reduce chemical waste, require less human oversight and labor, and, therefore, allow for more cost-efficient operations and products [7][8]. Increased throughput for applications such as drug screening or proteomic profiling allows for more time-efficient and faster means to discovering pharmaceuticals. When time is of the essence, such as during a pandemic, developing viable treatments and vaccines in a timely manner not only saves lives, but can also prevent prolonged disruption of daily life, which lessens the short-term impacts on local and national economies [9]-[16]. Reducing the amounts of chemicals and reagents used from hundreds of microliters and more down to a few nanoliters and less also save materials costs for researchers, creating more affordable drugs for the whole population to benefit from. Miniaturizing the volumes of each chemical reaction also results in the reduction of chemical waste produced, creating a more environmentally friendly process design and development. Even if chemical waste from, for example, the research and development of pharmaceuticals is only a fraction of overall waste including the consumption, excretion, and disposal of commercialized pharmaceutical products, every small effort for reduced waste and emissions is incredibly necessary for the preservation of the world we live in and the future of humankind [17].

The miniaturization and automation of traditional benchtop operations in biological and chemical research and industries is called microfluidics [18]-[20]. By now, microfluidics is by no means a new concept or field, but there is still much room for developing fully integrated, reliable microfluidic systems to be commercialized and widely used [20]-[22]. The integration of microfluidic technologies into a fully working

system is also known as lab-on-a-chip. Lab-on-a-chip technologies can not only be used for discovery phases of research and treatments but can also be used for the purposes of diagnostics [23]-[29]. In addition to the all the previously stated benefits of miniaturization and automation for more cost-efficient and time-efficient discoveries, the ability to manufacture portable and cost-effective lab-on-a-chip systems and deploy them around the world is extremely beneficial to give all humans access to proper healthcare, diagnosis, and treatments.

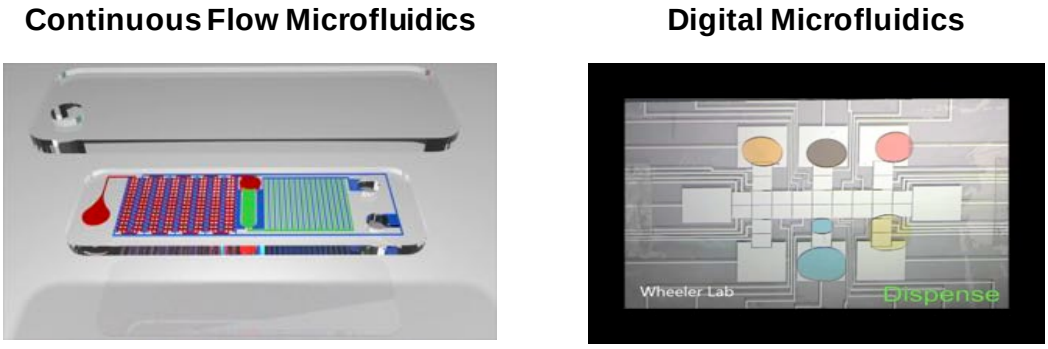

Figure 1.1 The two paradigms of lab-on-a-chip microfluidic systems
Continuous flow microfluidics (left) [30] and digital microfluidics systems (right) [31]. In continuous flow microfluidics, fluids flow along patterned channel geometries and in digital microfluidics, discrete droplets are individually manipulated around the device surface.

There are two paradigms of lab-on-a-chip systems as depicted in Figure 1.1. The first, utilizes continuous flow microfluidics where fluids flow in one-dimensional channels that are engraved, so to speak, into the device [25][30]. Mechanical on-chip pressure components such as pumps and valves help control fluid flow around the chip to perform operations such as mixing. The second paradigm of lab-on-a-chip systems is digital microfluidics where fluid in the form of discrete droplets can move independently around the plane of the microfluidics surface. In most cases, droplets are not restricted to channel geometries and are often actuated by electrical, optical, or magnetic means [31]-[39]. By not needing the mechanical valves and pumps that are required by continuous flow microfluidics, digital microfluidics eliminates the need for complex plumbing. In addition, whereas fluids in continuous flow microfluidic systems are constrained in all directions by channel geometries, digital microfluidic technologies can benefit from having an open top design. Exposed fluidic droplets from above allows for easier access as well as more fluidic operations and integration schemes. In this dissertation, we focus our efforts on digital microfluidics and more specifically, light-actuated digital microfluidics.

Previous research in our group encompasses optofluidic platforms designed for particle and droplet manipulation [40]-[49]. Light-induced particle-in-droplet manipulation is made possible by optoelectronic tweezers (OET), which is based on

the principle of dielectrophoresis. Light-induced whole droplet actuation and manipulation occurs by the principle of optoelectrowetting (OEW) as shown in Figure 1.2, which has its roots in the electrowetting theory. Demonstration of a unified OET-OEW platform to manipulate droplets and the particles within them has been previously reported, creating a multitude of possibilities for lab-on-a-chip applications [49].

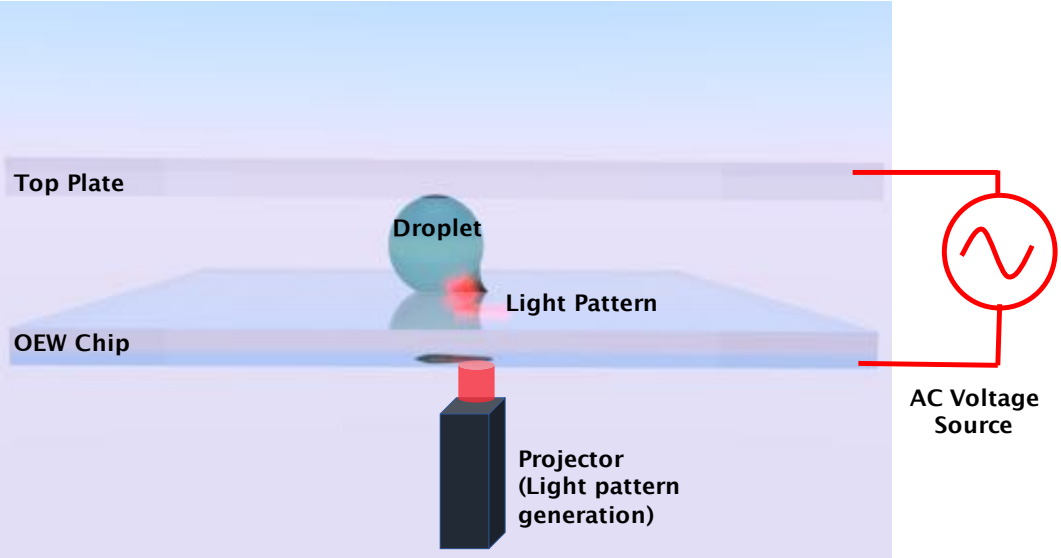

Figure 1.2 Schematic of a traditional optoelectrowetting (OEW) device
In optoelectrowetting, droplets are manipulated on the device surface by means of an optical light pattern generated by a light projector.

In this dissertation, we will present the most recent progress of our OEW platforms—namely, the introduction, analysis, and demonstration of our novel co-planar OEW device as rendered in Figure 1.3. First, we will begin with the basic principle of electrowetting and discuss how electrowetting combined with optical signals can be used to actuate droplets, rather known as OEW. Chapter 2 will revisit the traditional OEW device and discuss the OEW theory and ability for droplet actuation. In Chapter 3, we will introduce the co-planar OEW. The co-planar OEW device improves upon previous generations of OEW devices by integrating the top cover electrode contact onto the OEW device surface itself, opening the OEW platform to an even wider range of integration capabilities and applications. We will present a circuit model of the co-planar OEW device and analysis of the metal ground mesh for optimized performance. Chapter 4 provides an in-depth study of the contact angle change due to OEW. Both traditional OEW and co-planar OEW devices will be studied for comparison and to better understand the physical effect of OEW on the droplet's contact line.

After understanding the working principles of the co-planar OEW device and its effect on the droplet's contact line for movement, we will demonstrate an in-house, working co-planar OEW device in Chapter 5. Experimental operating conditions such as applied voltage, frequency, and light intensity will be studied in order to optimize droplet movement on the co-planar OEW device's surface and verify the co-planar OEW's optimization model. Finally, in Chapter 6, demonstrations of various droplet manipulations will be shown and described. The co-planar OEW device is capable of moving multiple droplets freely around the two-dimensional plane of the OEW surface simultaneously with the possibility for each droplet to have its own unique droplet path. Chapter 6 will also demonstrate the co-planar OEW's key benefit of more flexible integration configurations by integrating our device with a droplet-on-demand system to form a large-scale droplet array. We conclude that the OEW platform, with the traditional OEW and newer co-planar OEW devices, serves as a viable universal platform easily adaptable for a wide range of lab-on-a-chip applications. Through this work, we hope we give the reader a better understanding of the capabilities of the OEW optofluidic platform and a larger idea of what can be accomplished with such microfluidic systems for biological and chemical research to help those in need and humankind as a whole.

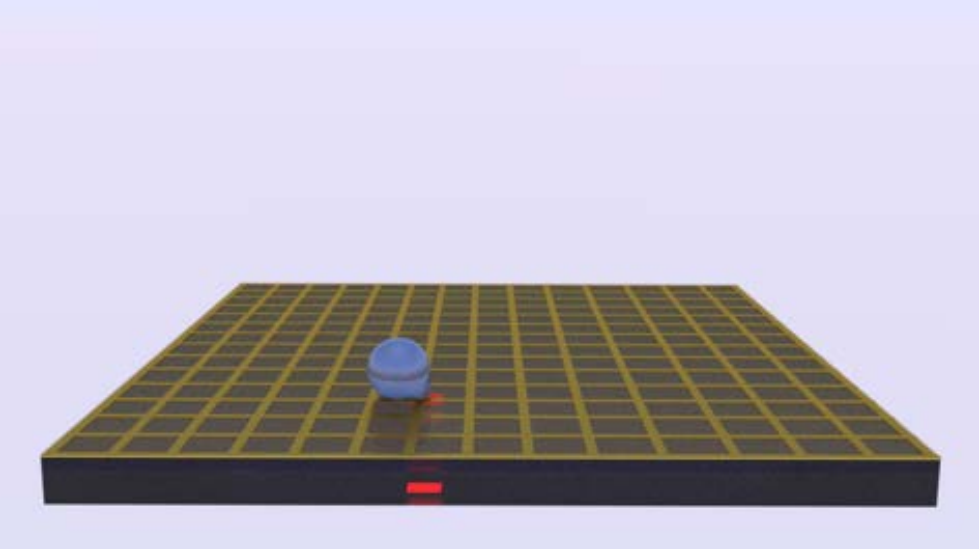

Figure 1.3 Schematic of the novel co-planar OEW device
A rendered depiction of a droplet sitting atop the co-planar OEW device surface that showcases a metal mesh grid that replaces the top cover from the traditional OEW design.

2 Optoelectrowetting (OEW) Principles

2.1 Introduction

Digital microfluidics has seen much development over the last couple decades [51]-[57]. As many of these technologies are becoming further developed and commercialized, the range of applications digital microfluidics and microfluidics as a whole can tackle continue to grow.

Droplet microfluidics as shown in Figure 2.1 can be categorized into two different types. The first is individual water-in-oil emulsions that flow through microfluidic channels such as in the continuous flow microfluidic paradigm [58]-[63]. This type of droplet microfluidics benefits from its high throughput ability to rapidly produce water-in-oil emulsions. However, these droplets must be processed sequentially and customizable operations for unique droplets are not available.

The second type of digital microfluidics is an individually addressable droplet system. This type encompasses several different technologies such as systems based on dielectrophoresis [64][65], acoustic waves [66]-[68], magnetic beads [69][70], electrowetting on dielectric (EWOD) [71]-[82], and optoelectrowetting (OEW) [40]. Whereas droplet microfluidics by channel microfluidics restrict the manipulation and control of independent droplets, droplet actuation by these methods does not depend on channel geometries and are controlled by independently addressing each droplet by each method's respective actuation signal whether it be magnetic, electrical, or optical.

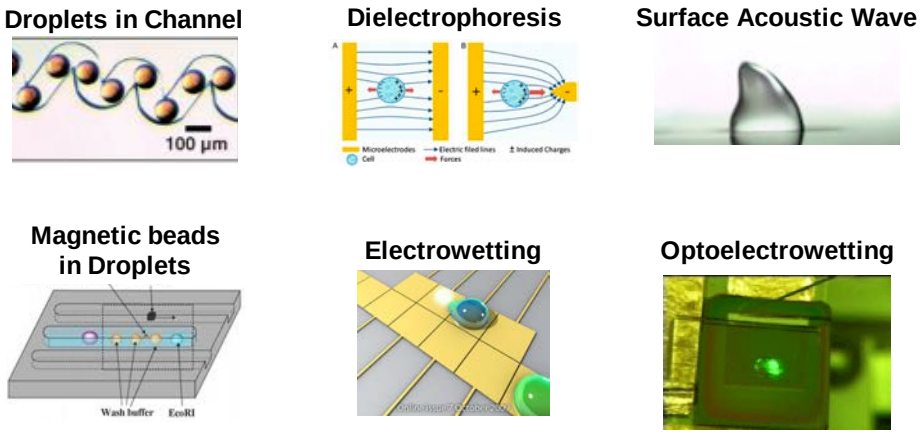

Figure 2.1 Various digital microfluidics technologies
Discrete droplets can be individually processed through various digital microfluidics technologies: droplets in channel [63], dielectrophoresis [58], surface acoustic wave [66], magnetic beads in droplets [69], electrowetting [71], and optoelectrowetting [40].

In this chapter, we will discuss this second type of digital microfluidics with a primary focus on OEW. OEW provides a platform for the independent and parallel manipulation of droplets of varying sizes. OEW shares its roots with EWOD, where both technologies take advantage of electrowetting principles to allow for an apparent contact angle change of a conductive liquid droplet on a solid surface. The following sections will go more in depth to discuss the optoelectrowetting principle, background, and design.

2.2 Electrowetting

The property of wetting is the ability for a liquid to adhere to a solid surface [83]. When observing a liquid droplet sitting atop a solid surface, one may notice that the liquid either spreads across the surface (full wetting) or that the droplet retains a droplet bead shape on top of the surface (partial wetting). The amount of wetting depends on the intermolecular interactions between the solid, liquid, and gas or surrounding media phases. The degree of wetting can be determined by the contact angle between the liquid-vapor and solid-liquid interface. The contact angle, θ, between the liquid and the solid surface it is sitting on top of is determined by the balance of surface energies between the three phases: the solid (surface), the liquid (droplet), and gas (or surrounding media). At the three-phase interface between the solid, liquid and gas there is the liquid-solid interfacial tension, γ_{ls}, the solid-gas interfacial tension, γ_{sg}, and a liquid-gas interfacial tension, γ_{lg}. The balance of these surface tensions along the z-axis and the resulting contact angle can be resolved using Young's equation (Equation (2.1)) [84]:

$$\gamma_{ls} = \gamma_{sg} - \gamma_{lg}\cos(\theta) \tag{2.1}$$

Perfect wetting is when the liquid spreads the solid surface at a contact angle of 0°. On the other extreme, a perfectly non-wetting case is when the contact angle is 180°. A partially wet state is when the droplet maintains a bead shape on the solid surface and has a contact angle between 0° and 180°. Within the partially wetted state, high wettability is when the contact angle is greater than 90° and low wettability is when the contact angle of the droplet is less than 90°.

Electrowetting can actively change the contact angle of the droplet by applying an electric potential between the solid and liquid interface [86]. Applying a voltage between the liquid droplet and solid surface results in a buildup of charge at the double layer of the liquid-solid interface, such as in Figure 2.2. This applied potential supplies electrostatic energy between the solid and liquid interface, which results in a reduction to γ_{ls}. The Lippmann equation (Equation (2.2)) describes the change in γ_{ls} due to the applied voltage, V [85].

$$\gamma_{ls}(0) - \gamma_{ls}(V) = \frac{1}{2}cV^2 \qquad (2.2)$$

where γ_{ls} is the surface energy due to the liquid-gas interface, c is the capacitance per unit area and V is the applied voltage across the dielectric layer.

The reduction in γ_{ls} due to an applied voltage causes the contact angle of the liquid droplet to decrease, which is the electrowetting contact angle, θ_{EW}. We can relate the electrowetting contact angle, θ_{EW}, to the voltage applied by balancing the interfacial tensions along the z-direction in the Young equation (Equation (2.1)) and Lippmann equation (Equation (2.2)), arriving at the modified Young-Lipmann equation, Equation (2.3):

$$\cos(\theta_{EW}) = \cos(\theta) + \frac{1}{2\gamma_{lg}}cV^2 \qquad (2.3)$$

where θ is the initial contact angle without voltage applied, γ_{lg} is the surface energy due to the liquid-gas interface, c is the capacitance per unit area and V is the applied voltage across the dielectric layer.

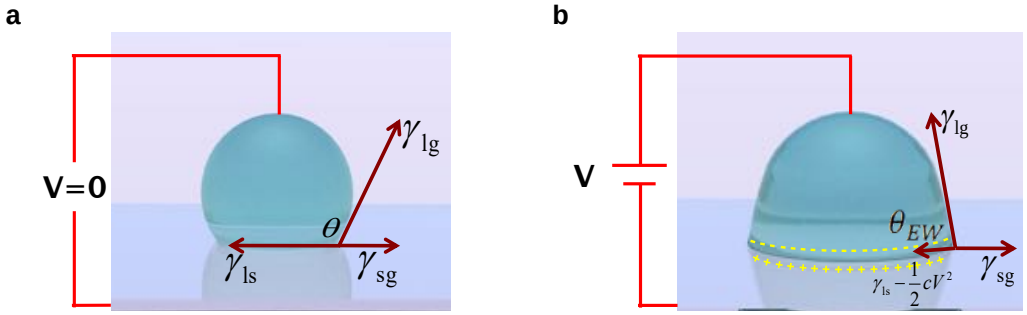

Figure 2.2 The principle of electrowetting
The contact angle, θ, of a liquid droplet sitting on top of a solid surface is dependent on the balance of interfacial energies amongst the liquid, solid, and surrounding medium, such as in (a) with no external voltage applied. When an external voltage is applied (b) between the liquid droplet and solid surface, the contact angle changes due to a change in the liquid-surface interfacial energy. This change in contact angle due to an applied voltage is called electrowetting and the resulting angle is θ_{EW}.

2.2.1 How to Move a Droplet

We now investigate how the effect of electrowetting can cause a droplet to move on a solid surface. Let us consider an example in Figure 2.3, where a single liquid droplet sits on two solid block electrodes placed side by side.

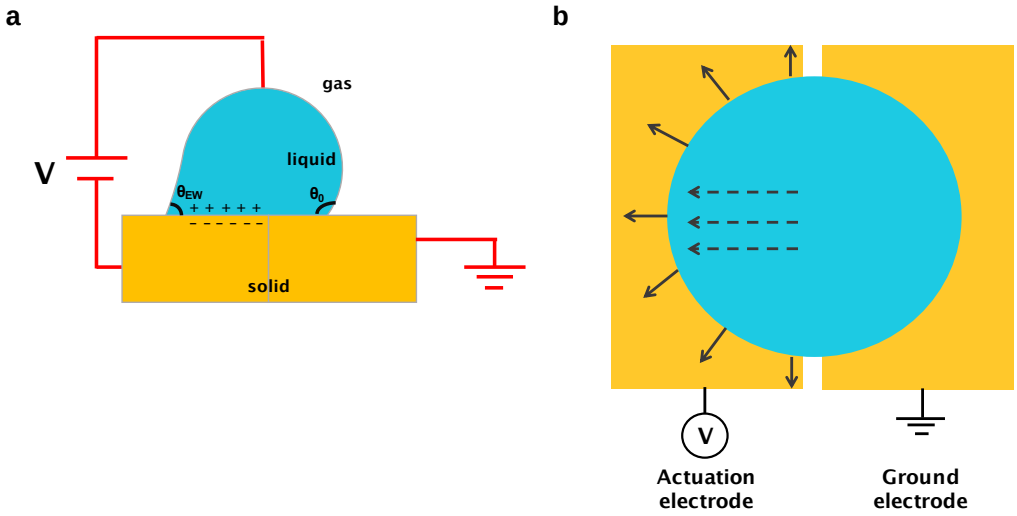

Figure 2.3 How to move a droplet using electrowetting
A droplet sits on top of two metal electrode blocks shown from a sideview (a) and from above (b). If the left electrode is actuated by a non-zero voltage while the right electrode is kept at ground, the half of the droplet sitting on the actuated electrode will experience a contact angle change. The contact angle of the droplet's side sitting on the ground electrode does not change. The creates a force imbalance within the droplet and causes the droplet to move toward the actuate electrode to regain equilibrium. A path of electrodes can be created with each electrode individually addressed to move a droplet along the path.

If we selectively apply a voltage between the liquid and one of the blocks (and keep the other block grounded or at 0 V potential), the electrowetting effect occurs on the electrically active side of the droplet, resulting in a reduction of the contact angle on that half of the droplet. The other half of the droplet sitting on the grounded solid does not see any electrowetting effect and does not experience a change in its contact angle. By selectively electrowetting only half of the droplet, there is a force imbalance within the droplet, creating a net force towards the electrowetting side and causes the droplet to move preferentially towards the electrowetting side. The net force per unit length can be derived from the difference of interfacial tensions along the z-direction.

$$F = \gamma_{lg}\cos(\theta_{EW}) - \gamma_{lg}\cos(\theta) \tag{2.3}$$

We set Equation (2.1) equal to Equation (2.2) for the case of electrowetting. Then, we can substitute Equation (2.3) to derive that the net force per unit length due to electrowetting is:

$$\frac{\text{Force}}{\text{length}} = \frac{1}{2}cV^2 \tag{2.4}$$

where c is the capacitance per unit area (Farad/m^2) and V is the applied voltage [87].

We can also do a similar analysis by instead considering the difference between the surface tensions on the electrowetting and non-electrowetting sides of the droplets due using Equation (2.5):

$$F = \gamma_{ls}(V) - \gamma_{ls}(0) \tag{2.5}$$

If we substitute Equation (2.5) into Equation (2.2), we derive the same previous force equation, Equation (2.4).

2.3 Electrowetting on Dielectric

Before we dive into optoelectrowetting itself, we will discuss how electrowetting can be used to move droplets. In the previous section, we discussed how applying a voltage to half of the droplet and solid interface could impart a positive net force towards the side of the droplet that undergoes electrowetting. And in order for the droplet to achieve equilibrium again, the droplet will move toward the electrowetting side. If a series of these conductive electrodes are created adjacent to each other and we selectively and sequentially apply a non-zero voltage to each of these electrodes as the droplet partially sits on top, we have created a path for the droplet to move through via electrowetting.

In fact, researchers from Duke University [51] and the University of California, Los Angeles (UCLA) [52], pioneered devices based on the electrowetting principle to move droplets and also improved on this basic concept. In their devices, they have added a dielectric layer on top of the conductive material to create what is known as Electrowetting-on-Dielectric (EWOD) devices as shown in Figure 2.4 [88]-[90]. The dielectric layer is added to improve device performance by allowing higher voltages to be sustained. Without this dielectric layer, only a small voltage can be sustained before dielectric breakdown occurs at the electric double layer. To account for the dielectric layer, the force per unit length due to an applied voltage, V, is substituted in Equation (2.4) and can be described as:

$$\frac{\text{Force}}{\text{length}} = \frac{1}{2}\frac{\varepsilon_0\varepsilon_{dielectric}}{t_{dielectric}}V^2 \tag{2.6}$$

where ε_0 is the permittivity of free space, $\varepsilon_{dielectric}$ is the dielectric constant and $t_{dielectric}$ is the thickness of the dielectric layer.

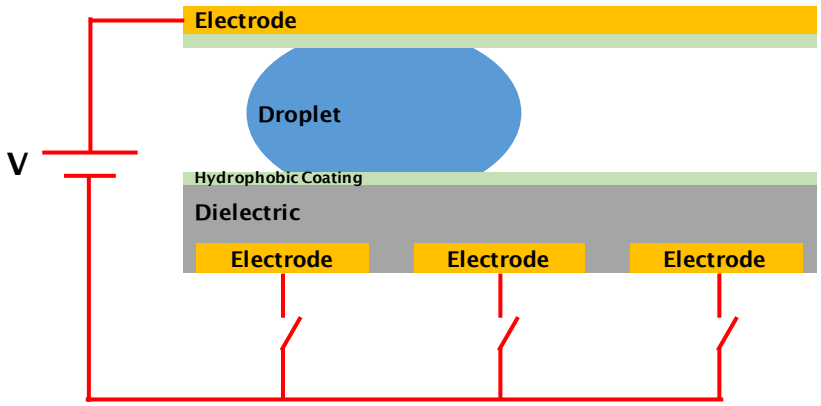

Figure 2.4 Electrowetting-on-dielectric (EWOD) schematic
EWOD devices consist of several electrodes that can be individually addressed and a dielectric layer that allows for higher voltages to be sustained before device breakdown. Droplets can be moved by sequentially activating each electrode to induce electrowetting.

In addition, instead of using a wire contact to the droplet as in our previous example of traditional electrowetting (Figure 2.2), EWOD devices use a planar top electrode cover made out of a conductive material, such as indium tin oxide (ITO). This makes it easier for the droplet to move around a two-dimensional plane without the need to actively move and probe a wire along with the droplet to maintain electrical contact. In EWOD devices, metal electrodes are patterned as an array. These electrode arrays can be programed such that the voltage signal can be applied to individual electrodes sequentially in order to move a droplet.

In previous examples describing the electrowetting effect, we have used air as the surrounding medium. The surrounding medium is not restricted to air or another gas—it can also be a liquid as long as it is immiscible with the droplet medium. For many EWOD device experimental setups (as well as for OEW device setups, which will be discussed later) oil is often used as a filler fluid instead of air. For one, oil lubricates the device surface while reducing the surface energy, reducing the voltages required to move droplets. Higher voltages are generally required to move droplets surrounded by air due to the higher surface tension between the droplet-air interface. In addition, oil as a filler medium prevents aqueous droplets from evaporating as quickly as they would in air alone due to the slow diffusion rate of water molecules in oil in addition to the slow evaporation rate of oil in air.

However, there are a few drawbacks to EWOD technologies. One is that droplets are limited to the size of the electrode pad size. Droplets dispensed cannot be smaller than the pad size, so careful consideration must be taken when designing electrode patterns. The array of electrodes requires N x N array programming for droplet actuation. Moving a droplet spanning multiple electrodes requires the coordination of multiple electrodes to be simultaneously yet sequentially actuated on and off in order to move a droplet, which leads to increased complexity.

2.4 Optoelectrowetting Principle

Now that we have discussed the background and principles of electrowetting and the ability to move droplets using electrowetting principles, we will investigate how we can use light as a driving force to actuate droplets on a solid surface. The combination of electrowetting and light to create a net force imbalance within a droplet to actuate droplets is called Optoelectrowetting (OEW) [41]. OEW is similar to EWOD in which it can manipulate and actuate droplets freely around a two-dimensional plane. However, it improves upon some of the complexities of EWOD devices by using light instead of patterned and programmed electrodes to create an electrowetting effect and actuate droplets.

OEW allows a droplet to undergo a contact angle change with the introduction of a photoconductor layer in its device structure along with incident optical patterns on the device to vary the voltage drop across the dielectric layer. This structure modification and light activation replaces the need for metal electrodes as used in EWOD devices. In order to manipulate droplets laterally across the device surface, a net force imbalance within the droplet needs to be created in order for the droplet to move along this force gradient. Optoelectrowetting achieves this by shining a light pattern on the photoconductor, acting as a virtual electrode, on one half of the droplet's contact line to induce a contact angle change. We refer to the condition when light is incident on a region of droplet sitting on the OEW device as the "light" or "on" state. On the other side of the droplet's contact line where no light is incident, the contact angle does not change. We refer to the condition when no light is incident on a region of the OEW device as the "dark" or "off" state. With half of the droplet's contact line in the off state and half of the droplet's contact line in the on state, a force imbalance is created between the droplet's light and dark regions, causing the droplet to move towards the light activated region.

A cross-sectional view of the traditional OEW device is shown in Figure 2.5 to demonstrate the concept of using light to impart an electrowetting force on part of an aqueous droplet. Figure 2.5 also details the structure and layers of the device. The bottom OEW chip is composed of an optically transparent glass substrate with a conductive indium-tin-oxide (ITO) layer on top. A photoconductive amorphous Silicon (a-Si) layer is deposited followed by a Al_2O_3 dielectric layer. A thin hydrophobic coating such as Teflon is deposited to reduce the surface tension between the water and solid surface interface, and thus increasing the droplet's initial contact angle. The droplet is sandwiched in between the OEW chip and a top cover made out of a glass substrate with conductive ITO that acts as the top electrical contact. To operate the device, an AC voltage is applied between the ITO top cover and the bottom OEW chip.

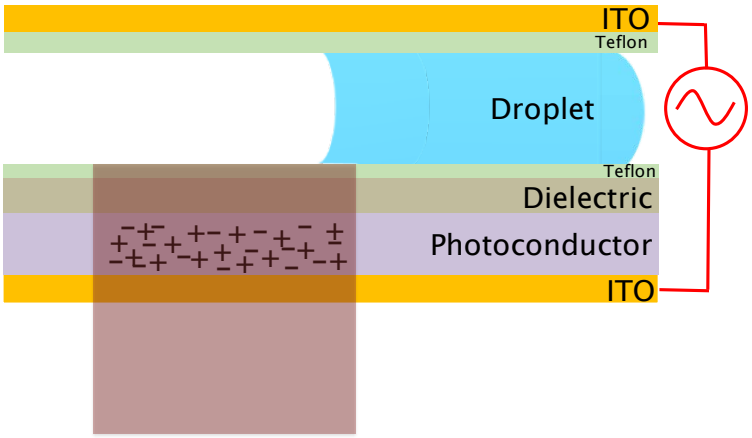

Figure 2.5 Traditional optoelectrowetting (OEW) device
The OEW chip is composed of an optically transparent glass substrate with a conductive indium-tin-oxide (ITO) layer on top. A photoconductive amorphous Silicon (a-Si) layer is deposited followed by a dielectric (Al_2O_3) layer. A thin hydrophobic coating is deposited to reduce the surface tension between the water and solid surface interface, and thus increasing the droplet's initial contact angle. The droplet is sandwiched in between the OEW chip and a top cover made out of a glass substrate with conductive ITO that acts as the top electrical contact. To operate the device, an AC voltage is applied between the ITO top cover and the bottom OEW chip. A light pattern increases the conductivity of the photoconductor layer, resulting in a contact angle change on the portion of the droplet under illumination. The part of the droplet without illumination maintains its contact angle, creating a net force imbalance causing the droplet to move towards the light pattern. Droplets can be moved around the OEW surface by moving the light pattern around the device surface.

When no light is incident on the OEW chip, the applied AC voltage mostly drops across the amorphous silicon photoconductor layer, as the impedance of the amorphous silicon is greater than that of the dielectric. Because of this, in the dark the droplet does not sense any electric potential and its contact angle stays the same. When light is illuminated on the OEW chip, however, the amorphous silicon layer's conductivity increases by more than 100x, measured empirically. The impedance of the amorphous silicon layer is now less than that of the dielectric layer, so the applied voltage now mostly drops across the dielectric layer. In this light state, the droplet now senses an electric potential, which results in a decrease of its contact angle on the OEW device surface. We create a light pattern to shine on part of the droplet's contact line, acting as a virtual electrode. By shining this light pattern on half of the droplet's contact line while keeping the other half of the droplet in the dark state, the droplet moves towards the light pattern. Moving the light pattern on the surface of the OEW device creates a motion path, which moves the droplet around the OEW device's surface. The droplet can move freely in any configuration around the OEW chip and the OEW chip can adapt to handle various droplet sizes by adjusting the size of the optical light pattern.

One significant factor in operating our OEW device is the necessity of an AC voltage signal to operate our devices. This is because when the OEW chip is operated under a DC voltage, the impedance of the dielectric layer is higher than that of the amorphous silicon layer in the dark and light state, so no additional contact angle change will occur between the dark and light state. As reported in previous studies and reconfirmed in this work, the maximum droplet movement response by OEW occurs around the 10 kHz – 20 kHz range [49]. To further investigate the optimal AC frequency range to operate our device, we review the circuit model of the OEW device.

2.4.1 Traditional OEW Circuit Model

We can better understand how various material and experimental setup properties can be tuned to optimize the device's performance such as determining the optimal frequency range to operate OEW devices. A depiction of the OEW device structure is shown in Figure 2.6.

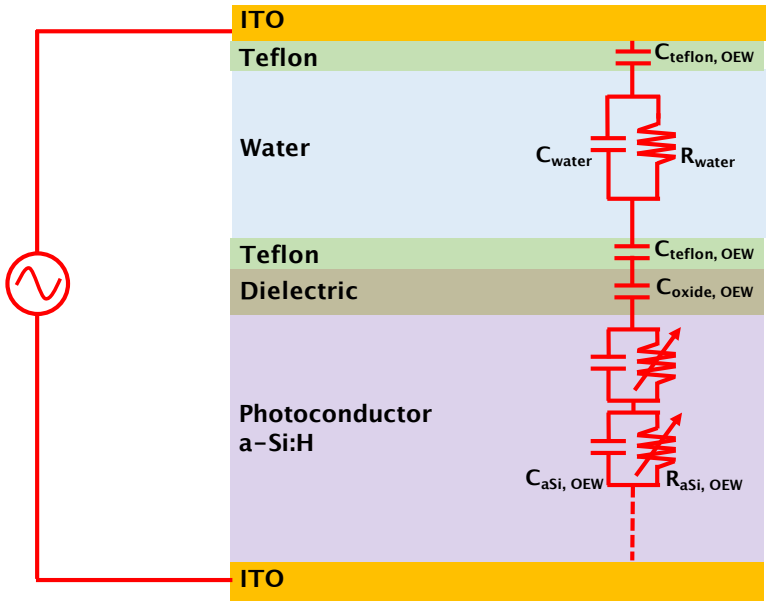

Figure 2.6 Traditional OEW circuit model
The OEW distributed circuit model [50] is used to understand and optimize OEW performance. The dielectric layer is modeled as a capacitor in series with the impedance of the photoconductor. The photoconductor layer is treated as several small slices each as an RC element to account for the absorption profile of light. The aqueous solution is modeled as an RC element.

An AC voltage source that activates the device is connected between the conductive top cover, modeled as a conductive wire, and the ITO layer of the main OEW device.

The aqueous droplet is modeled as an RC element, a resistor and capacitor in parallel. It is important to note that in the region of interest for OEW operation, however, the impedance of water is generally negligible. The dielectric layer is modeled as a capacitor in series with the impedance of the photoconductor. In a simplified case, the photoconductor can be modeled as a variable resistor where its resistance changes with the amount of light incident on the device. However, for a more thorough analysis, the photoconductor layer is modeled as an RC element where the resistance is a variable resistance depending on the amount of light applied [50]. The electron and hole carriers generated from the incident light depend on the absorptivity of the photoconductor material and the absorptivity is a function of the photoconductor's thickness. Therefore, to account for the absorption of light throughout our photoconductor, we break up our photoconductor layer into infinitely small slices of thickness δx. Each slice is its own RC element where its capacitance, $C_{photoconductor}$, at a depth x is:

$$C_{photoconductor}(x) = \frac{\varepsilon_0 \varepsilon_{photoconductor} A}{\delta x} \tag{2.7}$$

where ε_0 is the permittivity of free space, $\varepsilon_{photoconductor}$ is the dielectric constant of the photoconductor, and A is the unit area. The resistance photoconductor layer, $R_{photoconductor}$, at a depth x is:

$$R_{photoconductor}(x) = \frac{\varrho(x)\delta x}{A} \tag{2.8}$$

The resistivity of the photoconductor, $\varrho(x)$, accounting for the generation of electron and hole carriers is:

$$\varrho(x) = \frac{1}{q\mu_n \delta n(x) + q\mu_p \delta p(x)} \tag{2.9}$$

where q is the electron charge, and μ_n and μ_p are the mobility of electrons and holes, respectively. The resistivity at each depth location can be determined by the electron and hole generation concentrations ($\delta n(x)$ and $\delta p(x)$, respectively) due to the light at each depth. (Equation (2.10) and Equation (2.11))

$$\delta n(x) = G_{\delta x}(x)\tau_n \tag{2.10}$$

$$\delta p(x) = G_{\delta x}(x)\tau_p \tag{2.11}$$

where τ_p and τ_n are the hole and electron lifetimes, and $G_{\delta x}(x)$ (Equation (2.12)) represents the generation rate at each depth, x, due to the incident photon flux, N_0, or intensity of the light source. The generation rate is also dependent on the absorption coefficient, α.

$$G_{\delta x}(x) = \alpha N_0 e^{-\alpha x} \tag{2.12}$$

In the case of a monochromatic, single wavelength light Equation (2.12) is satisfactory. However, the generation rate of the photoconductor layer is dependent on the wavelength of light since the absorption of light within the photoconductor layer is dependent on the wavelength of light, accounted for by the absorption coefficient, α. Because white light sourced from a projector is commonly used in our experimental setups, we must account for the generation of carriers across the spectrum of wavelengths. The total generation rate by a broad-spectrum light source is calculated by summing the generation rates due to the photon flux of each individual optical frequency.

The AC impedance of each slice of the photoconductor as an RC element, $Z_{\delta x}$, is:

$$Z_{\delta x}(x) = \frac{\varrho(x)\delta x}{1 + j\omega\varepsilon_0\varepsilon_{photoconductor}\varrho(x)} \tag{2.13}$$

where ω is the AC frequency. The total impedance of the whole photoconductor layer, $Z_{photoconductor}$, is the integration of all the infinite slices of the photoconductor over its total thickness, t:

$$Z_{photoconductor} = \int_0^t Z_{\delta x}(x)\, dx \tag{2.14}$$

The capacitance of the dielectric layer, $C_{dielectric}$, is:

$$C_{dielectric} = \frac{\varepsilon_0\varepsilon_{dielectric}A}{t_{dielectric}} \tag{3.1}$$

where $\varepsilon_{dielectric}$ is the dielectric constant, A is the unit area and $t_{dielectric}$ is the thickness of the dielectric layer. The capacitive AC impedance, $Z_{dielectric}$, is therefore:

$$Z_{dielectric} = \frac{1}{j\omega C_{dielectric}} \tag{2.15}$$

As mentioned earlier, to calculate the net force per unit length on the droplet produced by OEW, we are interested in the voltage drop across the dielectric in the dark and light states. The voltage across the dielectric, $V_{dielectric}$, can be determined by using a voltage divider between the dielectric and the photoconductor layer:

$$V_{dielectric} = \frac{Z_{dielectric}}{Z_{dielectric} + Z_{photoconductor}} V \tag{2.16}$$

V is the applied voltage to the OEW device. To arrive at the net force per unit length in the droplet, F_{OEW}, we find the difference between the force generated by the droplet in the light state and the dark state:

$$F_{OEW} = \frac{1}{2}\frac{\varepsilon_0\varepsilon_{dielectric}}{t_{dielectric}}(V_{dielectric,light}^2 - V_{dielectric,dark}^2) \quad (2.17)$$

where $V_{dielectric,\ light}$ and $V_{dielectric,\ dark}$ are the voltages dropped across the dielectric layer in the light and dark states, respectively.

OEW performance can be optimized by changing material parameters such as dielectric and photoconductor layer thicknesses in our circuit model and analyzing the behavior of the resulting net force. In addition, the circuit model is pertinent in understanding the optimal AC frequency range to operate the OEW device. As previously studied and reported, an optimal combination for the dielectric and photoconductor layer thicknesses are 150 nm and 1 μm, respectively [50]. The resulting frequency range that should provide maximum response occurs around 10 kHz – 20 kHz. This compares well with experimental data [49].

2.5 Fabrication of the Traditional OEW Device

All OEW device fabrication was performed in the Marvell Nanolab at the University of Califorina, Berkeley. A 280 nm ITO coated glass wafer (Thin Film Devices Inc., Anaheim, CA) is used as the glass substrate for the OEW chip. A 1 μm silicon photoconductor layer is deposited (Oxford Plasmalab 80plus) on top of the ITO on glass substrate. Aluminum oxide is deposted via atomic layer deposition (ALD) using the Picosun Sunale R150. A thin 25 nm layer of CYTOP 809A (AGC Inc. Chemicals Company, Tokyo, Japan) is spin-coated at 3000 rpm for 30 seconds as a hydrophobic coating. The top cover of this traditional OEW device is made out of the 280 nm ITO coated glass wafer. The top cover is attached to the bottom OEW chip by using double-sided spacer tape of 500um to form a chamber that sandwiches the aqueous droplet.

2.6 Droplet Movement Demonstration

To operate the OEW device, an AC voltage is applied between the ITO contact layers of the OEW chip and the top cover. A 10 mS/m conductive water droplet composed of deionized water mixed with KCl is used as the aqueous solution. A Dell 4210X DLP digital projector is used as a spatial light modulator for generating light patterns. The light pattern on the chip can be resized but is generally of square shape with side dimensions about the size of the diameter of a droplet. Optical patterns are generated on a computer by darkening all pixels of the projector output and illuminating pixels pertaining to the light pattern. The fluidic chamber is filled with 1 cst silicone oil (DMS Trimethylsiloxy-terminated Polydimethylsiloxane, Gelest Inc. Morrisville, PA). As

previously mentioned, the oil media in which droplets are surrounded by are used to minimize the evaporation of droplets and to reduce the amount of friction during droplet movement. Figure 2.7 demonstrates the basic operation of droplet movement around a traditional OEW device biased at 44 V_{pp} and 10 kHz. Maximum droplet translation speed of 2 cm/s was achieved. The motion path of the light pattern and droplet is depicted by the dashed white line.

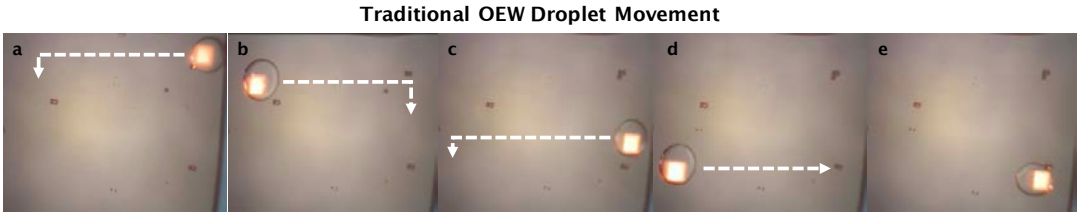

Figure 2.7 Traditional OEW droplet movement
An aqueous droplet (10 mS/m) immersed in 1 cst silicone oil initially sits in the top right of the OEW device (a) and moves through the OEW device (b)-(d). It ends its motion path at the bottom right of the OEW device (e).

2.7 Summary

OEW takes advantage of the electrowetting principle in order to manipulate discrete droplets by using light to induce a contact angle change along the droplet's contact line. Studies of the OEW device structure and circuit model investigate how to optimize OEW performance. Experimental setup conditions such as using a commercially available, digital light projector allows for more energy efficient operation and an attainable cost-effective setup. Reliable and fast droplet movement of around 2 cm/s is maintained throughout the generations of OEW devices. In the following chapters, we will discuss the operation, design, and optimization of a new generation of OEW devices: the co-planar OEW device. In addition, we will further understand the change in contact angles between the light and dark states as it applies to OEW and how optimizing and increasing the difference in dark and light state contact angles can help design future OEW devices to maximize the net force, speed, and movement along the droplet's contact line.

3 Co-planar OEW Design & Optimization

3.1 Introduction

Applications utilizing digital microfluidics span single cell analysis, genomic sequencing, proteomic analysis, stem cell research, and beyond [69], [91]-[102]. The traditional OEW device as presented in Chapter 2 provides a flexible platform to perform these assays with basic droplet manipulation techniques. However, one shortcoming of the traditional OEW device is its limitations in designing input and output configurations for larger microfluidic system integration. Due to the top cover electrode, droplets are sandwiched between the active OEW device and the top cover forcing any droplet dispensing or extraction techniques to be designed from the side openings. Although manageable, this can still prove to be challenging and limiting in scope.

Other digital microfluidic technologies like EWOD have demonstrated the ability to manipulate droplets by two-plated and single-sided designs. Two-plated and co-planar EWOD devices both still have patterned electrode patterns on the surface of the EWOD device, however their implementation differs. Because two-plated EWOD devices utilize the top cover as a ground or reference electrode, the electrodes patterned on the EWOD device surface are solely used for applying voltage for droplet actuation. Single-sided EWOD devices do not have the top cover reference electrode, so the electrode grid on the EWOD surface must also implement the ground electrode network where the droplet's leading edge is sitting on an activated electrode and its trailing edge is sitting on a ground electrode. EWOD's complexity is higher than OEW due to the design, programming and actuation of these electrodes. Droplet volumes are limited by the dimensions of each electrode and the number of droplets that can be accommodated are limited by the number of electrodes patterned onto the device surface. The traditional OEW device does not have patterned electrodes and instead uses an optical pattern generated off chip. The optical patterns generated can range in size and number eliminating the need for complex electrode dressing and providing a more flexible and generic system that can accommodate a wide range of application needs. However, as mentioned previously, the traditional OEW device utilizes a top cover electrode which limits the versatility of the device. Single-sided OEW devices have been previously reported by other groups but these designs result in a reduced OEW force [104]-[106].

In the following sections, we will introduce a co-planar OEW device that eliminates the need for a top cover electrode through the implementation of a conductive metal grid on the OEW surface and benefits from maintaining a high OEW force. Sessile droplets are no longer sandwiched between the main OEW device surface and the top electrode cover and are now accessible from above in addition to the sides. Droplet movement freely around the two-dimensional plane is preserved as movement is not limited to the grid pattern itself. This configuration allows for direct droplet access for

microfluidic system integration and droplet dispensing and extraction. We will discuss the design, theoretical circuit model and optimization of our co-planar OEW device.

3.2 Co-planar OEW Design

The co-planar OEW device, as shown in Figure 3.1, is similar to the traditional OEW structure. However, instead of a separate top cover ground electrode under which the droplet makes contact, the co-planar OEW device has an integrated metal mesh ground network that is fabricated on top of the dielectric layer of the active OEW chip. Figure 3.2 displays how the traditional OEW top cover gets integrated on top of the OEW surface to form the co-planar OEW device. A droplet is placed on the surface of the co-planar OEW device above the metal mesh ground and is exposed from the sides and above. To operate the co-planar OEW device, an AC voltage is applied between the ITO layer on the OEW chip and the metal mesh grid.

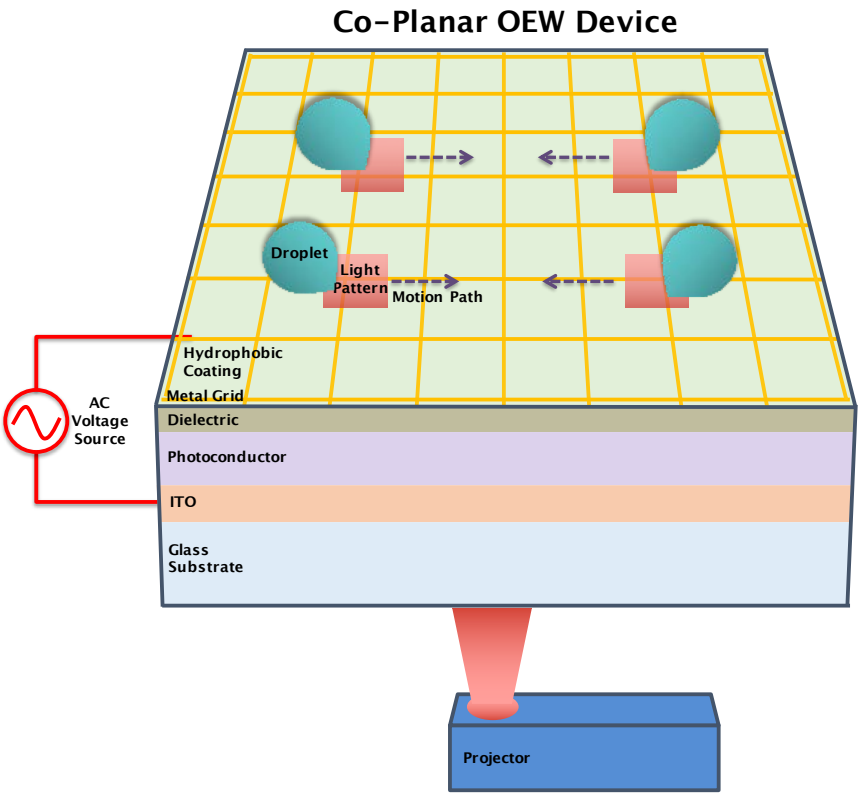

Figure 3.1 Co-planar optoelectrowetting (OEW) schematic
The co-planar OEW device eliminates the need for a ground electrode top cover by replacing it with an integrated metal mesh grid on the OEW surface. Droplets can still freely move around the two-dimensional device surface.

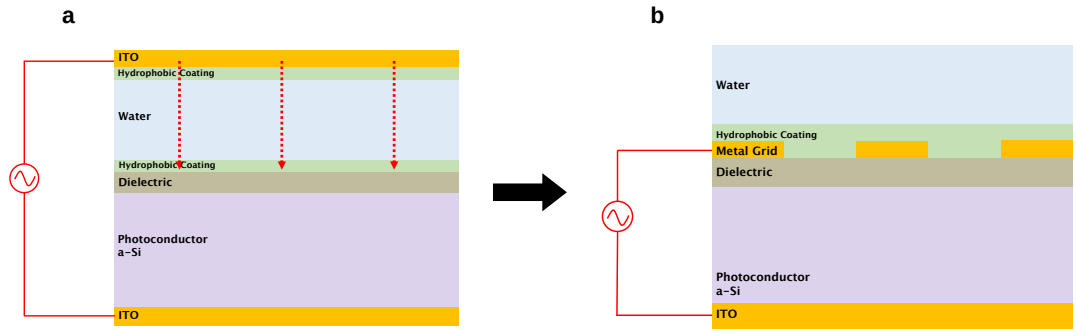

Figure 3.2 From traditional to co-planar OEW device
The traditional OEW device (a) features a ground electrode top cover that sandwiches the droplet on the OEW device. The co-planar OEW device (b) integrates the ground electrode top cover as a metal mesh grid on the OEW chip itself and allows the droplet to be exposed from above.

Droplet actuation of our co-planar device occurs similarly to the traditional OEW device by shining a localized visible light pattern on the OEW chip. In the dark state with no light incident on the device, the applied AC voltage drops primarily across the a-Si photoconductor layer. By shining light on the OEW device, the conductivity of the a-Si increases by 100x under the illuminated areas. Because of this increase in conductivity, the voltage drop under the illuminated areas is mostly across the dielectric layer, creating a "virtual electrode" on the device surface. We selectively shine light on the photoconductor layer under part of the droplet's contact line to achieve an electromechanical force imbalance in the droplet between the light and dark states, which causes the droplet to be attracted towards the light pattern. We can achieve droplet translation by creating a light path for the light pattern to move across the device surface and therefore move the droplet with it.

Previous concepts of co-planar electrodes on OEW platforms have been proposed, but these devices either have a reduced electrowetting force or require a higher actuation voltage or light requirement. Fair et al. [104] has conceptually described a grid electrode pattern on EWOD, but no working device has been demonstrated to the best of our knowledge. Chuang et al. [105] has introduced a continuous OEW device where reference and driving electrodes are alternately patterned. Although similar in concept to our co-planar OEW device, our co-planar OEW device design more directly utilizes and benefits from a higher net force efficiency compared to their continuous OEW design. In addition, Park et al. [106] has reported on a single-sided continuous OEW device that lacks a top ground electrode. In their device design, they do not implement patterned ground electrodes but instead place the actuation and reference electrode on two ends of the device. The voltage path is lateral along the two-dimensional plane which requires light to activate the whole amorphous silicon layer and actuate droplets by introducing dark patterns. This is inverse to our co-planar OEW optical pattern configuration where the device is initially not illuminated and only moves with the activation of an incident light pattern, which is more beneficial

for minimizing surface thermal heating from the light source, preventing photobleaching for light sensitive experiments, and improving energy efficiency. Our co-planar OEW design preserves the functionality and benefits of OEW and maintains a higher operational efficiency.

In the following sections, we will analyze how different materials and device parameters can affect device performance. We will go into detail on how droplet movement can be optimized by analyzing the force per unit length exerted by the device. The next section explains the importance of this force as a way to investigate optimized performance.

3.3 Co-planar OEW Circuit Model

The co-planar OEW device differs from the traditional OEW device due to the addition of the metal grid on its surface. We depict the co-planar OEW cross-section with each layer's corresponding circuit elements in Figure 3.3. The cross-sectional view of the OEW device in Figure 3.3 is of one period of the device.

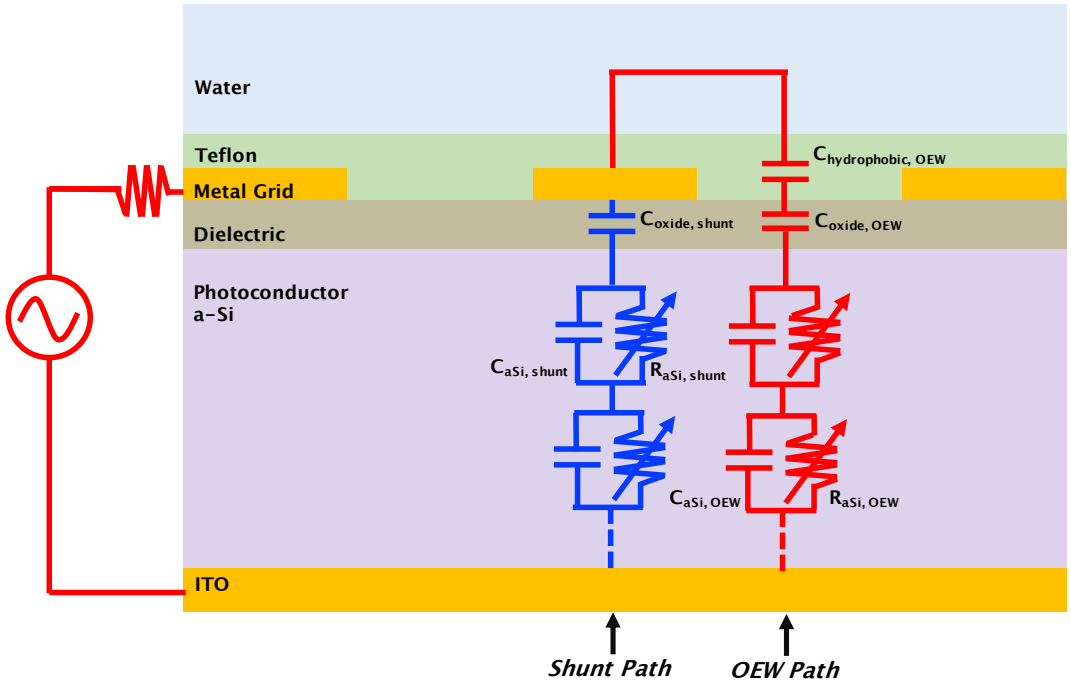

Figure 3.3 Co-planar OEW circuit model
The introduction of a metal mesh grid in the co-planar OEW adds a "Shunt Path" (blue) that discounts the effective OEW force that is produced in the open OEW region noted by the "OEW Path" (red). The co-planar OEW circuit model accounts for one period of the metal mesh grid, so the overall effective resistance of the metal grid is also accounted for by the resistor symbol that connects to the node shared by the shunt path and OEW path.

Looking at a top view of the metal mesh grid for the co-planar OEW in Figure 3.4, we define the metal line having a width, W, and metal pitch between two metal lines as, P. A_{shunt}, the area underneath the metal line width creates a shunt path. The spacing between metal lines, is our active OEW area, A_{OEW}. A_{shunt} and A_{OEW} are defined in terms of the metal line width, W, and metal pitch spacing, P as:

$$A_{shunt} = 2PW - W^2 \tag{3.2}$$

$$A_{OEW} = (P - W)^2 \tag{3.3}$$

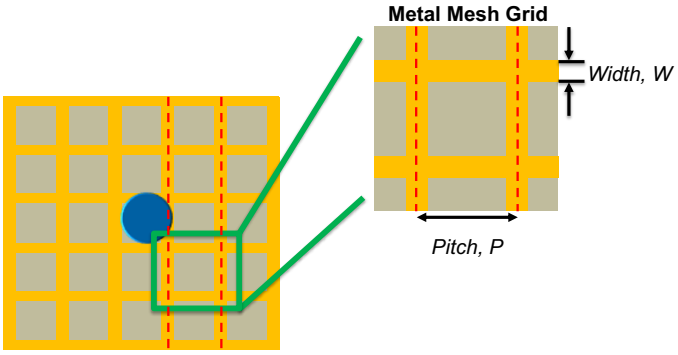

Figure 3.4 Metal mesh grid top view
The metal mesh grid (yellow) of the co-planar OEW is shown above. The metal line width is defined as W. The distance between two metal lines is the pitch size, P.

The liquid droplet sitting on top of the device surface such as water, is modeled as an RC element. Its resistivity in the OEW operation regime is generally very low and negligible. The dielectric layer is modeled as a capacitor, $C_{dielectric}$, with a capacitance of:

$$C_{dielectric} = \frac{\varepsilon_0 \varepsilon_{dielectric} A}{t_{dielectric}} \tag{3.4}$$

where A refers to either A_{OEW} or A_{Shunt}, ε_0 is the permittivity of free space, $\varepsilon_{dielectric}$ is the dielectric constant, and $t_{dielectric}$ is the thickness of the dielectric layer. Its AC impedance operating at an AC frequency, ω, is described as:

$$Z_{dielectric} = \frac{1}{j\omega C_{dielectric}} \tag{3.5}$$

The a-Si photoconductor layer has previously been modeled as an RC element where its resistance is dependent on the light intensity incident on the device and the conductivity change between the dark and light states, which is taken from empirical values of the conductivity through the bulk of the photoconductor layer.

However, in practice and as discussed in Section 2.4.1, carriers generated by light are not uniformly distributed through the photoconductor layer. These carriers are distributed according to the light intensity profile and decay inversely to the absorption coefficient, or exponentially from the surface. In addition, carrier generation is dependent on wavelength, and since we use a white light source via a digital projector, we must account for this wider spectrum of light. In order to determine the power density of the incident light for our experimental setup, we used a spectrometer (Ocean Optics Inc., Largo, FL) to measure the power densities from our projector. The absorption coefficients were taken from literature and for the sake of this circuit model, we have simplified the output spectrum of our projector to be composed of blue (450 nm), green (550 nm), and red (700 nm) wavelengths. It is also important to note that even when the device is in the dark state with all of the projector's pixels turned to black, there is still a minimal amount of background light to account for. The photoconductor circuit element we describe follows a more detailed analysis based off of the distributed circuit model [50].

We model the photoconductor layer as infinitely small slices of photoconductor layers with a thickness δx. Each slice is its own RC element where the resistance, $R_{photoconductor}$, and capacitance, $C_{photoconductor}$, are described in Equation (3.6) and Equation (3.7), respectively,

$$R_{photoconductor} = \frac{\varrho(x)\delta x}{A} \tag{3.6}$$

$$C_{photoconductor} = \frac{\varepsilon_0 \varepsilon_{photoconductor} A}{\delta x} \tag{3.7}$$

where $\varrho(x)$ is the resistivity at a certain depth x, and $\varepsilon_{photoconductor}$ is the dielectric constant of the photoconductor. Therefore, the AC impedance, $Z_{\delta x}$, of each slice per unit area at an AC frequency, ω, is:

$$Z_{\delta x}(x) = \frac{\varrho(x)\delta x}{A(1+j\omega\varepsilon_{photoconductor}\varepsilon_0\varrho(x))} \tag{3.8}$$

In order to determine the resistance, the resistivity at each depth location, x, can be determined by:

$$\varrho(x) = \frac{1}{q\mu_n \delta n(x) + q\mu_p \delta p(x)} \tag{3.9}$$

where $\delta n(x)$ and $\delta p(x)$ are the electron and hole generation concentrations, respectively, due to the light at each depth x, q is the electron charge, μ_n and μ_p is the

mobility of electrons and holes. $\delta n(x)$ and $\delta p(x)$ are represented by the generation rate, $G_{\delta x}$, and the hole and electron lifetimes, τ_p and τ_n:

$$\delta n(x) = G_{\delta x}(x)\tau_n \tag{3.10}$$

$$\delta p(x) = G_{\delta x}(x)\tau_p \tag{3.11}$$

$G_{\delta x}$, the generation rate (Equation (3.12)) is determined by N_0, the photon flux, and α, the absorption coefficient at a depth x. N_0 (Equation (3.13)) is determined by wavelength, λ, and the power density of the light source. In Equation (3.13), c is the speed of light and h is Planck's constant. In the case of using a white light source, we must account for the range of wavelengths and the power density incident on the device in order to determine the total carrier generation.

$$G_{\delta x}(x)=\alpha N_0 e^{-\alpha x} \tag{3.12}$$

$$N_0 = \text{Power Density x } \left(\frac{c}{h\lambda}\right) \tag{3.13}$$

The total impedance of the photoconductor layer, $Z_{photoconductor}$, is the integration of all the infinite slices of the photoconductor through its total thickness, t:

$$Z_{photoconductor}= \int_0^t Z_{\delta x}(x)dx \tag{3.14}$$

The total impedance of the dielectric layer in the OEW region, $Z_{dielectric_{OEW}}$, is a summation of the impedance of the dielectric layers that contribute to the OEW force:

$$Z_{dielectric_{OEW}} = Z_{Teflon_{OEW}} + Z_{oxide_{OEW}} + Z_{Teflon_{shunt}} \tag{3.15}$$

Where $Z_{Teflon_{OEW}}$ and $Z_{oxide_{OEW}}$ are the Teflon and oxide material impedances in the OEW area, and $Z_{Teflon_{shunt}}$ is the Teflon impedance in the shunt area. The net OEW force, F_{OEW}, due to the light and dark states on the droplet during operation is:

$$F_{OEW} = \frac{1}{2}\frac{\varepsilon_0\varepsilon_{dielectric}}{t_{dielectric}}(V_{dielectric,light}^2 - V_{dielectric,dark}^2) \tag{3.16}$$

where $V_{dielectric,\ light}$ is the voltage drop across the dielectric in the light state and $V_{dielectric,dark}$ is the voltage drop across the dielectric in the dark state.

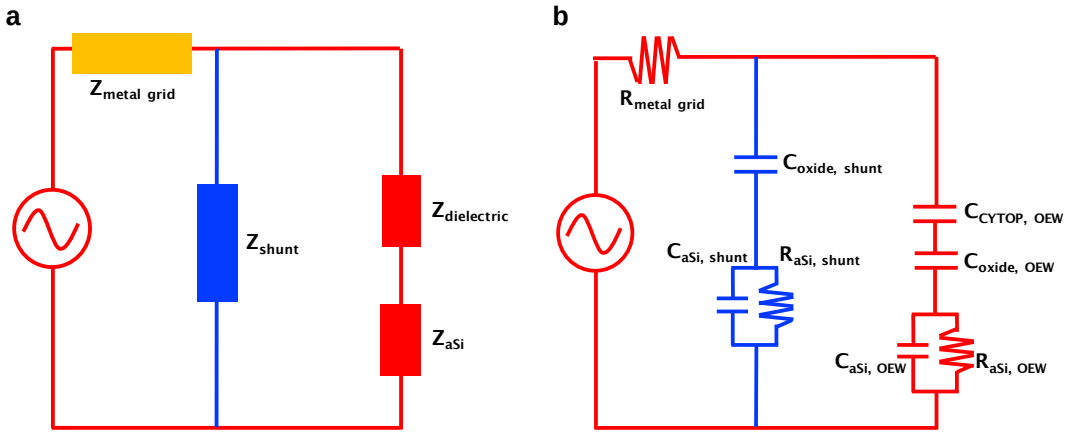

Figure 3.5 Co-planar OEW block diagram circuit model
A co-planar OEW block diagram is shown in (a) to simplify the circuit model diagram. Each of the main elements contributing to the overall co-planar OEW circuit is detailed in (b). The voltage across the dielectric layer, $Z_{dielectric}$, is the element of interest in determining the overall OEW force.

Figure 3.5 depicts the circuit elements of the co-planar OEW as a block diagram where each block is the impedance of the various paths. The co-planar device differs from the traditional OEW device with the introduction of a metal grid that introduces a shunt path, which decreases the effective voltage for electrowetting. Under the metal grid shunt area, there is a shunt capacitance due to the dielectric layer and a shunt RC distributed element due to the photoconductor that contribute to the overall shunt impedance, Z_{Shunt}. We call the impedance in the active OEW area, composed of the capacitance due to the dielectric layer and RC distributed element due to the photoconductor, Z_{OEW}. Z_{Shunt} and Z_{OEW} are parallel to each other, so we can define their parallel impedance relationship as $Z_{OEW + Shunt}$:

$$Z_{OEW+Shunt} = Z_{OEW} \,||\, Z_{Shunt} \tag{3.17}$$

Since the cross-sectional circuit model only accounts for one period of the active OEW area (A_{OEW}) and metal grid area (A_{Shunt}), there is an additional circuit element that shares the node with the OEW path and shunt path. This element is the overall effective metal grid resistance, Z_{metal}. The voltage at the node in between the greater metal network and one period of OEW area, $V_{OEW + Shunt}$, can be determined by:

$$V_{OEW+Shunt} = \frac{Z_{OEW+Shunt}}{Z_{OEW+Shunt}+Z_{metal}} V_{applied} \tag{3.18}$$

where $V_{applied}$ is the applied AC voltage between the ITO layer and metal grid contacts. The voltage across the dielectric in the active OEW region can therefore be described as:

$$V_{dielectric} = \frac{Z_{dielectric_{OEW}}}{Z_{dielectric_{OEW}} + Z_{photoconductor_{OEW}}} V_{OEW+Shunt} \quad (3.19)$$

where $Z_{photoconductor_{OEW}}$ is the impedance of the photoconductor layer in the OEW region. We use this circuit model to study our co-planar OEW device and optimize our metal grid for peak droplet actuation performance.

3.4 Metal Mesh Grid Analysis

Because the co-planar OEW device design replaces the virtual ground top cover of a traditional OEW device with a metal mesh grid integrated onto the surface of the OEW device, we want to study the performance of the co-planar device and optimize droplet movement on our device. We will study how changing the physical parameters of the metal mesh grid affect device performance. The parameters we will look at regarding the metal mesh grid is the metal line width, metal line pitch, shadowing effect due to the metal grid, and the metal grid resistance. In addition, we will discuss how these parameters of the metal mesh grid determine the minimum droplet volumes allowed.

As described in the previous section, the metal mesh lies co-planar to the active OEW region that allows a liquid droplet sitting on its surface to experience electrowetting. Because of this, the metal mesh grid forms a shunt path in the circuit model of the co-planar OEW and reduces the effective voltage sensed by droplet for an electrowetting effect. We aim to look at how the dimensions of the metal mesh affect device performance and how to design the metal mesh to optimize droplet actuation.

To analyze the performance of the co-planar OEW device, we must first derive the effect of the metal mesh grid and derive an equation for the force per unit length the device exerts on the contact line of the droplet. As described in Section 3.3, the area in one period of the device that is covered by the metal mesh grid is called the shunt area A_{shunt} (Equation (3.2)). The area of the active OEW region in one period on our device is called OEW area or A_{OEW} (Equation (3.3)). The total area for one period, A_{Total}, is the active OEW area and the shunt area combined (Equation (3.20)):

$$A_{Total} = A_{OEW} + A_{shunt} \quad (3.20)$$

We call the ratio of the active OEW area over the total area as the fill factor, FF (Equation (3.21)):

$$FF = \frac{A_{OEW}}{A_{Total}} \tag{3.21}$$

The shunt area does not contribute to the electrowetting force, but instead, the metal pattern shields light from the droplet and prevents an electrowetting force to be experienced by the droplet. In order to account for the reduction in active electrowetting, we can multiply the OEW force equation (Equation (2.17)) by the metal mesh grid fill factor (Equation (3.21)). The net force per unit length the droplet experiences by the co-planar OEW device, $F_{co\text{-}planar\ OEW}$, is the force per unit length under light conditions minus the force per unit length under dark conditions:

$$F_{co\text{-}planar\ OEW} = \frac{1}{2}\frac{\varepsilon_0\varepsilon_{dielectric}}{t_{dielectric}}(V_{dielectric,\ light}{}^2 - V_{dielectric,\ dark}{}^2) \times FF \tag{3.22}$$

where $V_{dielectric,\ light}$ and $V_{dielectric,\ dark}$ are the voltages dropped across the dielectric layer from Equation (3.19) for the light and dark states.

With respect to the metal mesh grid, two factors that could affect the force per unit length are the dimensions of the metal mesh grid and the contribution of the resistance from the rest of the grid outside the one period of the OEW area. As modeled and illustrated in Figure 3.6, we will go more in depth on how these two factors affect the optimal performance of our device.

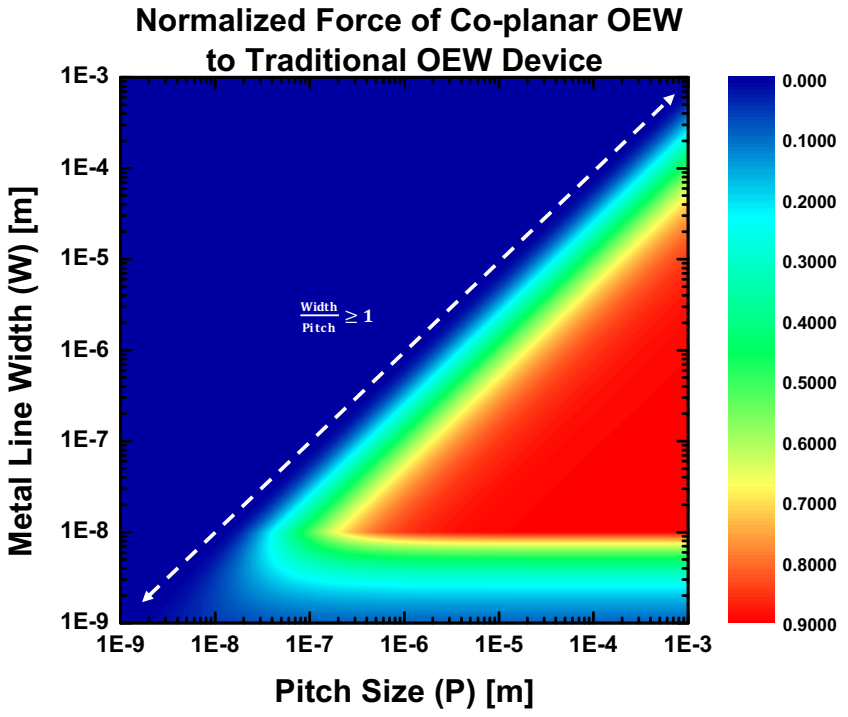

Figure 3.6 Normalized force of the co-planar OEW device
The surface plot compares the OEW force of the co-planar OEW device normalized to the traditional, two-plated OEW device as a function of the metal mesh grid's line width and pitch size. Higher OEW forces are colored in red and low OEW forces are in blue.

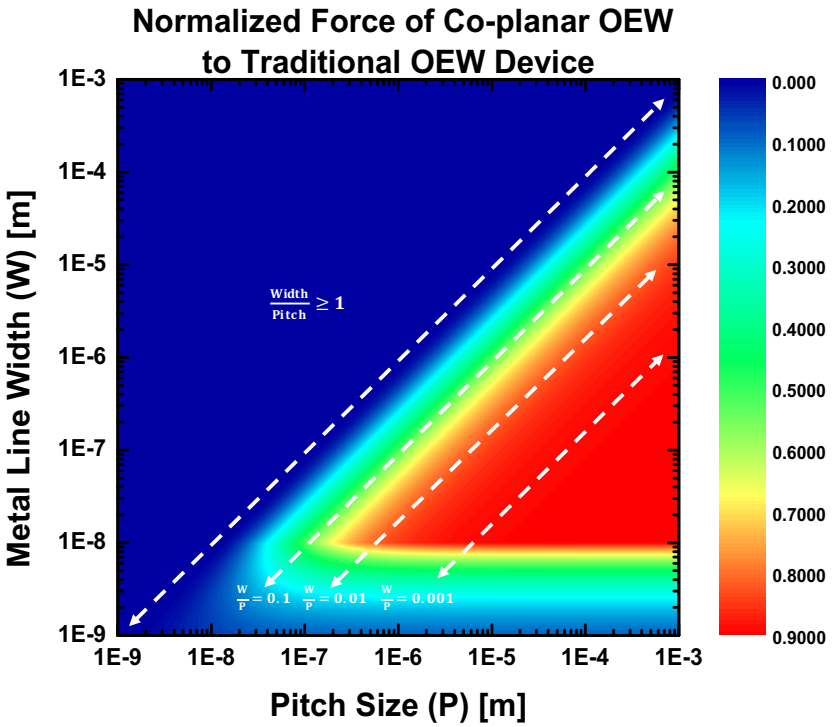

Figure 3.7 Fill factor effect on co-planar OEW normalized force
The surface plot compares the OEW force of the co-planar OEW device normalized to the traditional, two-plated OEW device as a function of the metal mesh grid's line width and pitch size. The upper triangular region of the plot indicates zero OEW force contribution by the co-planar OEW device due to the metal line width dimension being greater than the pitch size, covering the entire effective OEW area. Each dotted diagonal line indicates a fixed width-to-pitch ratio (0.1, 0.01, 0.001). Along the fixed width-to-pitch ratios, the effective OEW force remains constant until the metal line resistance becomes more significant in affecting the OEW force.

3.4.1 Metal Mesh Grid

To study the effects of how the dimensions, namely the width (W) and pitch (P) of the metal lines affect device performance, we vary the width of our metal line and the pitch in between two metal lines. Figure 3.6 represents a surface plot model of the net force per unit length normalized to the net force per unit length of a traditional OEW. The normalized net force per unit length of a traditional OEW device is set to 1, since we expect the force to be the same as it is not affected by any effects of a metal grid (since such grid does not exist). The red color indicates a higher normalized net force per unit length up to 90% and dark blue represents a low normalized net force per unit length down to 0% (or no force). The x-axis represents the metal pitch distance, P, and the y-axis represents the metal line width, W. The upper left triangular region of the plot is dark blue in color representing a 0% net force. This is because in this region of the model plot, the metal line width is larger than the pitch meaning the whole chip would be covered by metal. This case is not meaningful to our study of

our OEW device since it nullifies the OEW operation and implies no electrowetting. We focus our discussion on the lower right triangular region of the surface plot. As the metal pitch size increases at a set metal line width, the normalized force per unit length increases for the co-planar OEW structure as more active OEW area is exposed. Similarly, for a given set metal pitch distance, as the metal line width decreases and becomes thinner, there is an increase in the normalized net force per unit length due to less shielding by the metal shunt area. Because of the fill factor effect, the normalized net force per unit length increases as A_{shunt} decreases compared to the A_{OEW}. Diagonal slices of the surface plot indicate a fixed fill factor ratio, meaning the ratio of A_{OEW} with A_{Total} remains the same. Along fixed fill factor values as shown in Figure 3.7, the normalized force of the co-planar OEW device stays the same compared to the traditional OEW device. The edge cases where the co-planar OEW force starts to drop off relative to the traditional OEW device is the regime where the metal line widths get significantly small and the resistance of the full metal grid become significantly noticeable.

3.4.2 Metal Mesh Grid Resistance

Our circuit model accounts for one period of a metal line shunt area and active OEW region when in fact our device is composed of a larger metal grid network. In order to understand how the overall metal grid resistance affects our device performance, this section focuses on the resistance due to the rest of the grid as shown in our circuit model block diagram. The resistance of a metal segment, R_{metal}, can be calculated using Equation (3.23) using the geometry in Figure 3.8 where ϱ_{metal} is the resistivity of the metal, L is the dimension of the segment parallel to current flow and A is the cross-section of the metal area perpendicular to current flow.

$$R_{metal} = \frac{\varrho_{metal} L}{A_{metal}} \tag{3.23}$$

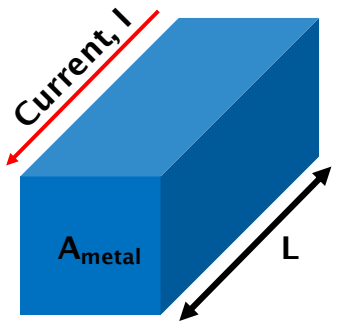

Figure 3.8 Resistance through a solid
A solid block of resistive material is illustrated in this figure. The direction of current flow indicates the dimensions for determining the resistance of the material as defined by Equation (3.23).

We can model our resistive mesh grid network as a finite mesh grid of N x N resistors where N is an integer and is the number of resistors on one side of the square metal grid network that we can fit in a given chip area, as shown in Figure 3.9. We use LTSPICE software to model what the overall grid resistance is as we increase the number of resistors in our N x N grid and see that the overall resistance follows a logarithmic trend (Figure 3.10).

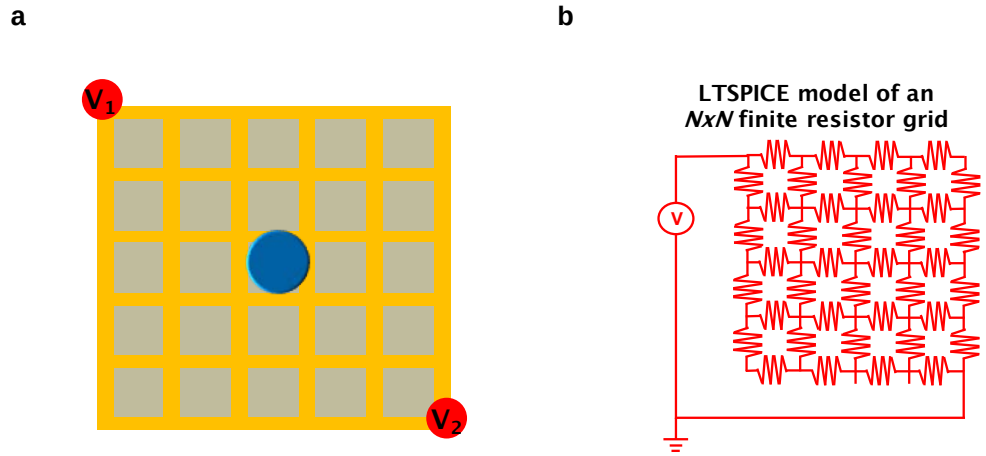

Figure 3.9 N x N finite resistor grid
A top view schematic of the metal mesh grid of the co-planar OEW device is shown in (a). Each grid segment represents an individual resistor, and the metal mesh grid network circuit is depicted in (b). LTSPICE circuit modeling software is used to determine the overall resistance of the metal mesh grid for various sized square N x N grid sizes where N is an integer.

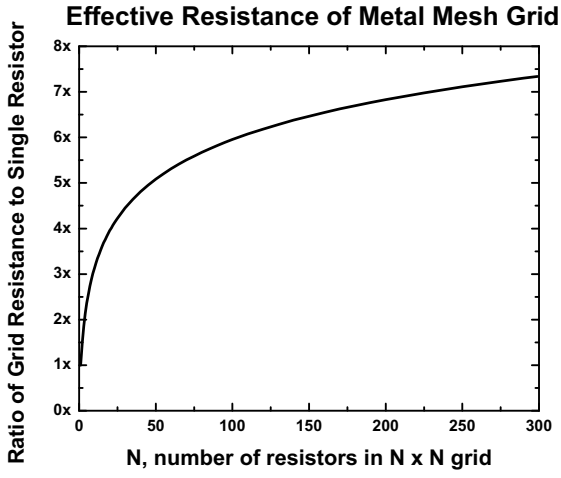

Figure 3.10 Effective resistance of metal mesh grid
The effective resistance of a metal grid is calculated using LTSPICE circuit modeling software. This figure plots the ratio of the total resistance of a N x N metal grid to the resistance of a single resistor segment as a function of the integer number N that defines the dimensions of the N x N resistor grid.

Test structures of metal mesh grids with 3 μm line widths and various pitches of 60 μm, 100 μm, and 300 μm were fabricated with varying N x N grid sizes to measure the resistance of the overall metal grid. The LTSPICE model compared to the fabricated devices is shown in Figure 3.11. We note that for our fabricated devices the overall grid resistance is negligible and does not have a strong effect on the normalized force per unit length. For example, for our 300 μm pitch device with a gold thickness of 100 nm and gold metal line width of 3 μm, the resistance of one line in a square is 24 Ω. According to our LTSPICE model, for the area of our OEW device, this would create an overall grid resistance multiplier factor of 5 (from Figure 3.10) leading to 122 Ω as the overall effective grid resistance. This is also confirmed in the surface plot model from Figure 3.6. Only as the metal line widths decrease below 10 nm do we start to see this overall effective resistance increase and decrease the overall net force per unit length.

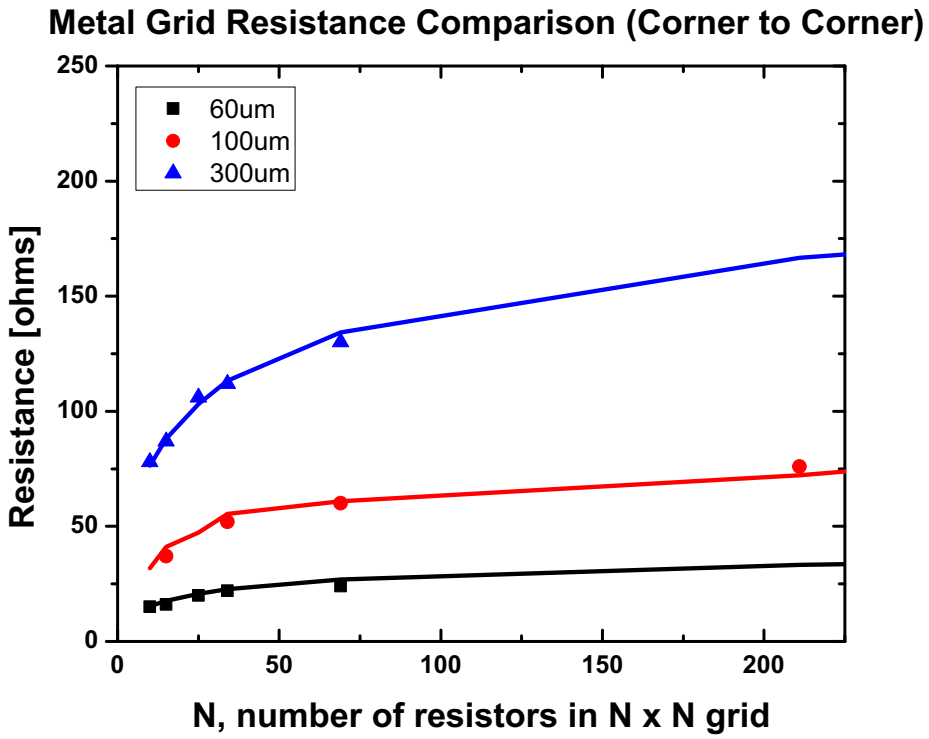

Figure 3.11 Metal grid resistance comparison
Various N x N dimensional metal grid test structures of 60 μm (black), 100 μm (red), and 300 μm (blue) pitch sizes were fabricated and measured for their overall effective grid resistance (squares). These resistances are plotted against the calculated resistances for the corresponding pitch sizes and N x N grid sizes as found by LTSPICE (solid line).

3.4.3 Metal Mesh Grid Geometry

The pattern of the metal design on the OEW device can vary. Our initial design is composed of a square grid network; however, an assortment of metal grid designs could work as long as the droplet meets the actuation requirements: the droplet makes contact with both the metal grid and the active OEW region. In fact, to reduce the footprint of metal on our device, linear stripes of metal lines can be patterned and used. By incorporating this design in the circuit model, we note that although the shunt area reduces due to less metal, the theoretical performance of our OEW device increases marginally. Even though we have not empirically confirmed this finding, we would expect to see a slight improvement in droplet actuation performance.

3.4.4 Minimum Droplet Size Requirement

Although the surface plot model shows that the net force per unit length increases as the metal pitch increases, there is a tradeoff to consider. In order for a droplet to move, it must be on the active OEW region but also in contact with a metal line. As the droplet diameter becomes smaller than the metal line pitch, it can still be moved as long as this condition is met, however, it is also likely the droplet can move into an active OEW area only and lose contact with a metal line. When this happens, the droplet is deemed lost, as we cannot use light to actuate the droplet out anymore and must resort to mechanical means. Therefore, one criterion for droplet size is that the droplet contact area on the surface needs to be at least the size of the metal grid pitch. When the metal pitch distance increases, this increases the minimum size of the droplet required, which could contradict the purpose of using a microfluidics platform for its benefit of decreased droplet reaction volumes.

In order to calculate the minimum droplet volume needed, we model the droplet sitting on the surface as a hemispherical volume as illustrated in Figure 3.12. To calculate the minimum volume needed for various pitch sizes, the metal pitch size, P, is equal to the diameter of the droplet. We can use Equation (3.24) to calculate the smallest droplet volume, $\text{Volume}_{\text{min}}$, that can be moved.

$$\text{Volume}_{\text{min}} = \frac{1}{12}\pi P^3 \tag{3.24}$$

Figure 3.12 plots the minimum droplet volume that correspond to different metal pitch sizes. Looking at the surface plot in Figure 3.13, we note that at various metal line pitches of 10 μm, 100 μm, and 1 mm the minimum droplet sizes required are on the order of 1 pL, 1 nL and 250 nL, respectively. Droplets of this scale are in the scope of interest. Knowing this, we can therefore choose metal line width thicknesses that can correspond with higher net force per unit lengths to actuate our droplets.

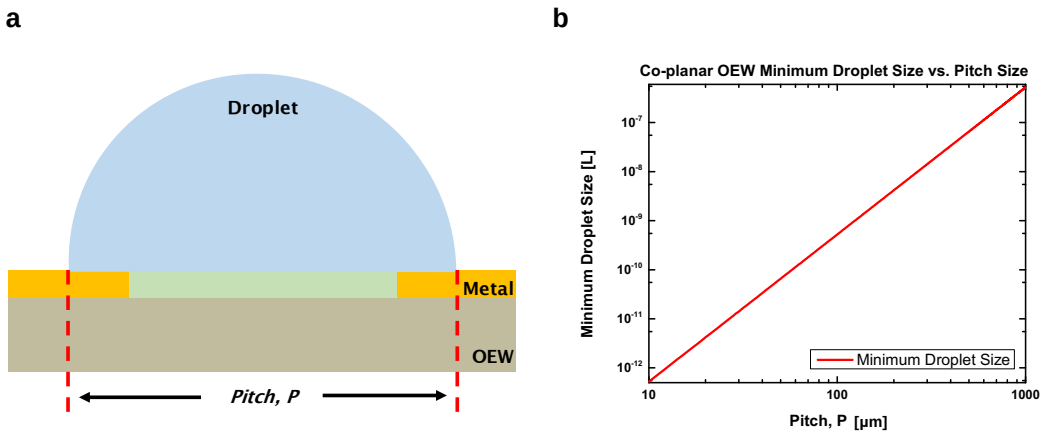

Figure 3.12 Minimum droplet size requirement
A cross-sectional view of the co-planar OEW device is illustrated in (a) with the pitch size of the metal mesh grid defined. The pitch size determines the minimum droplet volume required since the droplet must cover the OEW area and the metal line in order to be able to move. The plot in (b) graphs the minimum droplet volume to the corresponding pitch size. The droplet is modeled as a hemispherical volume sitting on the solid surface.

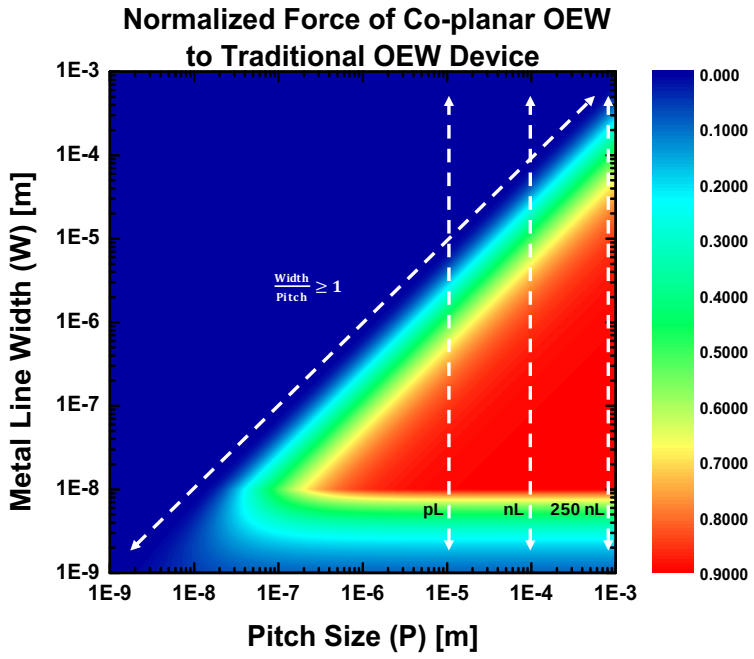

Figure 3.13 Minimum droplet volumes in relation to the OEW force
The surface plot compares the OEW force of the co-planar OEW device normalized to the traditional, two-plated OEW device as a function of the metal mesh grid's line width and pitch size. The vertical dotted lines correspond to a fixed metal mesh pitch size and its corresponding minimum droplet volume.

3.5 Goals for Optimization

The two main layers of interest in the OEW device structure is the photoconductor layer and the dielectric layer. Previous studies have been done to look at the optimization of the photoconductor layer and dielectric layer optimization in the traditional OEW device [50]. In this section, we will recapitulate the discussion on how to determine the optimal thickness of these layers for the OEW device for droplet actuation.

3.5.1 Dielectric Layer

We first look at the dielectric layer, which can be modeled as a capacitor and can be described in Equation (3.25):

$$C_{dielectric} = \frac{\varepsilon_0 \varepsilon_{dielectric} A}{t} \tag{3.25}$$

where ε_0 is the permittivity of free space, $\varepsilon_{dielectric}$ is the dielectric constant, A is the unit area, and t is the thickness of the dielectric layer.

For a given actuation voltage (44 V_{pp}), Figure 3.14 models how the OEW force varies with oxide thickness. OEW force is directly proportional to the capacitance of the dielectric layer and therefore inversely proportional to the thickness of the dielectric layer. As the oxide layer becomes thicker, the OEW force decreases, so it would seem ideal to keep the dielectric layer as thin as possible. However, as we will soon discuss, we must be mindful of the dielectric breakdown limit to determine an optimal thickness for the dielectric layer and operational AC voltage.

If we seek to reduce the actuation voltage applied to our OEW device but maintain the same OEW force for droplet actuation, we can use a material with a higher dielectric constant or reduce the thickness of the dielectric. Not only can we choose a material with a higher dielectric constant, but higher quality dielectric layers can also be deposited via atomic layer deposition (ALD) which aids in the fine scaling of dielectric thickness by increasing the dielectric constants of some materials. However, as beneficial it is to create thinner dielectric layers, there also a limit on how thin the dielectric layer can be, which is governed by dielectric breakdown, E [76]:

$$E \propto \frac{V}{t} \tag{3.26}$$

The voltage, V at which breakdown occurs in the dielectric is linearly proportional to the thickness of the dielectric, t (Equation (3.26)). As shown in Figure 3.15, the thinner a dielectric layer is, the lower the voltage needed at which breakdown occurs. However, the electrowetting voltage is proportional to the square root of the dielectric

thickness. For a certain dielectric thickness, the operating electrowetting voltage can be increased to achieve a bigger electrowetting force until this voltage becomes large enough to reach the dielectric breakdown limit. In other words, to maintain the same amount of electrowetting force, there exists a lower limit for how thin the dielectric can be so that breakdown does not occur. Therefore, applying more voltage to achieve more force to actuate a droplet is only beneficial until the dielectric layer breaks down. Dielectric breakdown causes permanent damage to the dielectric layer and electrolysis in the aqueous droplet rendering the chip unusable once this limit is reached. For the dielectric layer, aluminum oxide (Al_2O_3) deposited by ALD was chosen due to its high dielectric constant and strength.

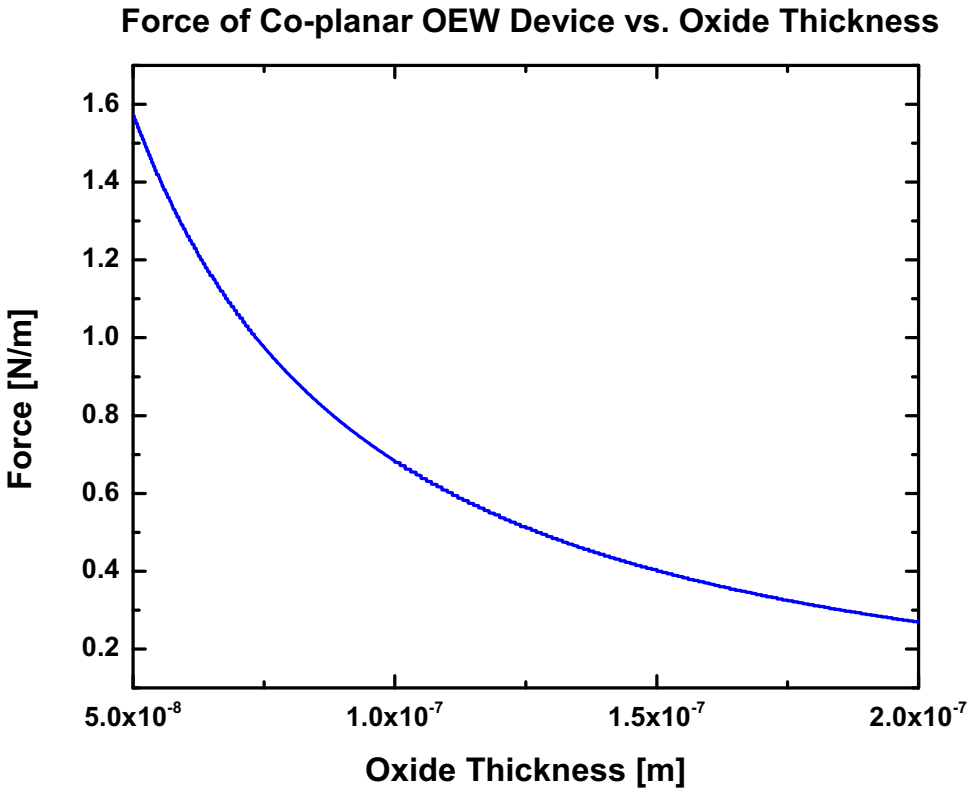

Figure 3.14 Force of co-planar OEW device vs. oxide thickness
As the dielectric layer thickness increases, the OEW force decreases for a given applied voltage, since the dielectric layer's capacitance is inversely proportional to its thickness.

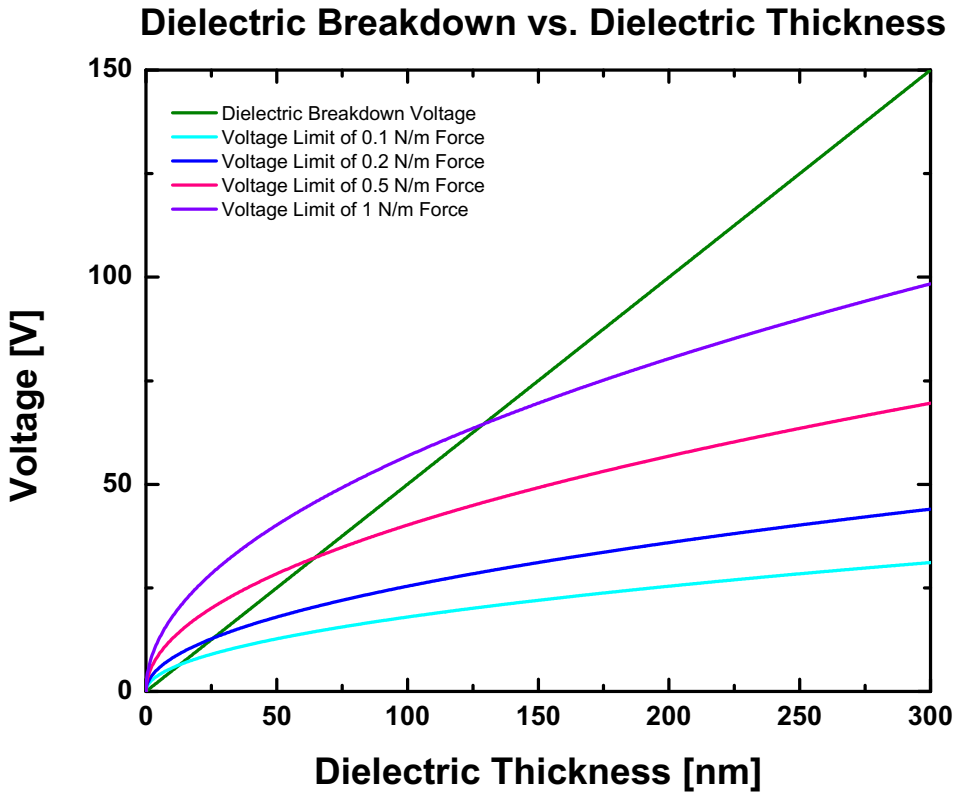

Figure 3.15 Dielectric breakdown
Voltage is graphed against the dielectric layer thickness. The dielectric breakdown voltage limit of Al_2O_3 has a linear relationship with its thickness (green). To achieve a certain amount of OEW force (0.1 N/m, 0.2 N/m, 0.5 N/m, and 1 N/m), the amount of applied voltage needed depends on the dielectric layer thickness. Dielectric layers that are too thin result in device failure due to breakdown before enough OEW force is generated. Dielectric layers that are thick require higher voltages for operation.

3.5.2 Photoconductor Layer

The other layer of interest in the OEW device structure is the photoconductor layer. In order to determine an optimal thickness for the photoconductor layer, we consider how the photoconductor thickness affects the amount of light power absorbed and how to achieve the most electrowetting force while utilizing using a lower powered light source for energy efficiency. Figure 3.16 plots OEW force with increasing a-Si thickness. If our photoconductor layer is too thin, not only is there less overall OEW force, but there will also not be a significant difference in impedance between the light and dark states due to the generation of fewer carriers. However, if the photoconductor layer is too thick, more light power is required to be absorbed through the thickness of the layer to generate carriers and turn on the virtual electrode.

$$I(x)=I_0e^{-\alpha x} \qquad (3.27)$$

Equation (3.27) describes the profile of light intensity, I, at various thicknesses, x, of the photoconductor layer where I_0 is the initial light intensity and α is the absorption coefficient. The intensity of light decreases exponentially with thickness in a material. For a thick photoconductor layer, we would need a stronger initial light source to be sustained throughout the photoconductor. Although a stronger laser could be used as a virtual electrode in a thicker photoconductor, it is also generally beneficial to reduce the amount of power used across our system for better energy efficiency, safer practices, and to create a more easily attainable and commercialized system. The choice of a DLP presentation projector, a generic light source that can be easily programmed, outputs lower power of 1.5 W/cm^2 and is widely commercialized, is attractive. For material selection, amorphous silicon is chosen as the photoconductor material in our OEW devices because it has high absorption in the visible optical range and can absorb most light in a thin film of around 1 μm. In addition, it is widely used in fabrication processes and industry applications such as solar cells.

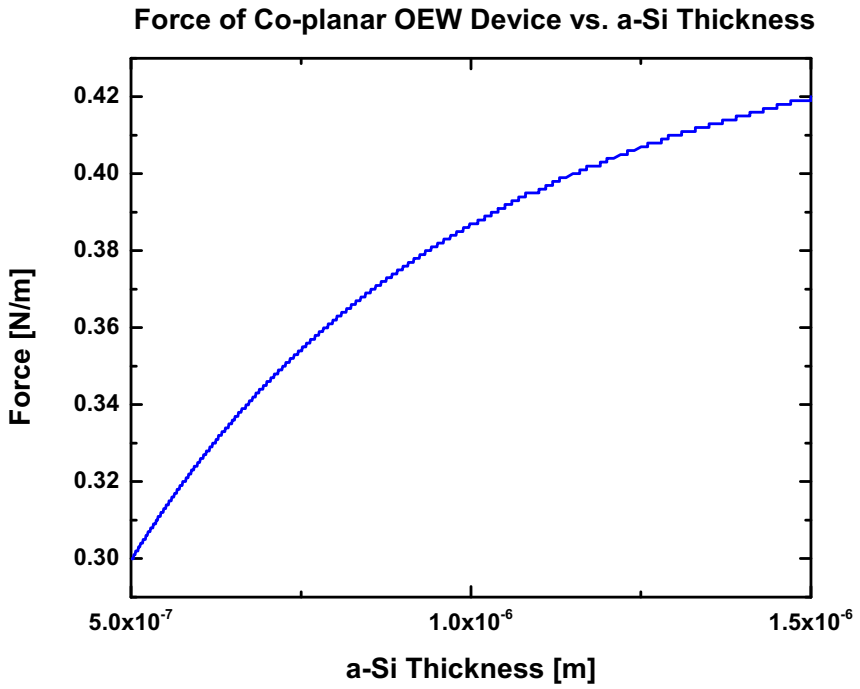

Figure 3.16 Force of co-planar OEW device vs. a-Si thickness
As the a-Si layer thickness increases, more OEW force can be generated for droplet movement. Effective absorption of the light throughout the whole a-Si layer must also be considered for optimal performance.

3.6 Summary

The previous generation traditional OEW device has proven to be reliable and robust in its performance for droplet actuation. However, the top cover electrode limits the traditional OEW device's abilities for input and output configurations for larger system integration. To address this issue, we have presented the co-planar OEW device that benefits from having an open top for more feasible and limitless system integration configurations. The co-planar OEW features an integrated metal mesh grid on the OEW device surface that takes place of the top cover electrode from the traditional OEW device design. The metal mesh grid design still allows for reliable droplet movement freely around the two-dimensional surface plane comparable to the traditional OEW device. Simultaneous actuation of various droplet sizes can still be accommodated on the co-planar OEW device similar to the traditional devices, with size limitation dependent on metal grid design.

4 OEW Contact Angle Analysis

4.1 Introduction

As discussed earlier, the working principles of OEW are based in electrowetting and the physical change in the droplet's contact angle when a voltage is applied to the solid-liquid interface. Manipulating half of the contact angle of the droplet's contact line creates an asymmetry or net force imbalance within the droplet that allows the droplet to move. However, merely changing the contact angle on half of a droplet's contact line may not be enough. The net force produced by the OEW effect must be strong enough to overcome the static and dynamic frictional forces to allow the OEW device to move. Therefore, the contact angle change between the dark and light states of a droplet using OEW must be great enough to produce a significant force for movement.

We have previously analyzed various material and experimental parameters and how they affect the performance and the force output of the co-planar OEW device to move droplets. However, previous OEW studies have not gone as in depth about the physical contact angle change that occurs due to the applied bias and light activation. In this chapter, we will study the effect of the contact angle on both the traditional OEW device and the co-planar OEW device for comparison. We explore how the physical contact line changes with an applied voltage, an applied light pattern, and how we can optimize for even better droplet manipulation.

4.2 Contact Angle

To describe the initial contact angle of a droplet sitting on a solid surface, we can use Young's equation (Equation (2.1)) from Section 2.2. The initial contact angle, θ, of any liquid droplet sitting atop a solid surface is dependent on the difference between the liquid-solid surface energy, γ_{ls}, and the solid-gas surface energy, γ_{sg}, and inversely proportional to the liquid-gas surface energy, γ_{lg}. To reduce the wetting effect and to create a higher contact angle between the droplet and the solid surface, we want to either reduce the surface energy between the liquid-gas medium or to increase the difference between the liquid-solid surface energy and the solid-gas surface energy. Both can be achieved by using oil instead of air as the surrounding medium in addition to using a low energy hydrophobic coating such as Teflon AF or CYTOP. In order to find the contact angle change due to an applied electrowetting voltage we can use the modified Young-Lippman equation as previously discussed in Section 2.2 (Equation (2.3)).

The angle change is dependent on the voltage applied and the interfacial energy between the liquid and filler medium, γ_{lg}, whether it be a gas such as air or liquid such as oil. The surface energy of the solid surface does not play a role for the electrowetting effect itself as its key role is to influence the initial contact angle. An additional contact angle change due to light can be found by the voltage drop across the oxide and hydrophobic layers (that make up the whole dielectric layer) due to the change of photoconductivity in the photoconductor layer under the light state. In order to calculate the voltage drop across the dielectric layer, we look at the voltage divider in Equation (2.16) and Equation (3.19) for the traditional and co-planar OEW, respectively. The electrowetting contact angle due to the voltage drop, θ_{EW}, can be written as:

$$\theta_{EW} = \cos^{-1}\left(\cos(\theta) + \frac{1}{2\gamma_{lg}} \frac{\varepsilon_0 \varepsilon_{oxide}}{t_{oxide} + t_{hydrophobic}\left(\frac{\varepsilon_{oxide}}{\varepsilon_{hydrophobic}}\right)} V_{dielectric}^2\right) \tag{4.1}$$

where θ is the initial contact angle of the droplet, γ_{lg} is the interfacial energy between the liquid and surrounding medium, ε_0 is the permittivity of free space, ε_{oxide} is the dielectric constant of the oxide, $\varepsilon_{hydrophobic}$ is the dielectric constant of the hydrophobic coating, t_{oxide} is the thickness of the oxide layer, $t_{hydrophobic}$ is the thickness of the hydrophobic coating layer, and $V_{dielectric}$ is the voltage dropped across the whole dielectric layer. Equation (4.1) rearranges Equation (2.3) to seek the electrowetting contact angle while also accounting for the dielectric layers.

The main factor influencing the difference between the dark and light states of our OEW chip is the photoconductivity of the a-Si in the dark and light states. The distributed circuit model as discussed in Section 2.4.1 accounts for the absorption of a given light source throughout the thickness of the a-Si layer as broken up into small slices. The distributed model is more sensitive as it is dependent on the incident power of the light source at individual wavelengths, absorption coefficients for individual wavelengths, and the electron and hole lifetimes and mobilities. Being able to tune these parameters more can help optimize the a-Si for future device improvements.

4.3 Contact Angle Experiments

Contact angle experiments were performed to verify projections by the OEW contact angle model. All experiments were performed using a USB camera (Omron Sentech STC-MB152USB, Kyoto, Japan) and image processing by ImageJ (NIH, Bethesda, MD). Both traditional OEW and co-planar OEW devices were used with a-Si thicknesses of 1 μm, an alumina layer of 150 nm, and a 25 nm thick CYTOP hydrophobic layer. For the co-planar OEW device, a metal width line of 3 μm and a metal pitch size of 300 μm design was used.

4.3.1 Hydrophobic Coating

The use of a hydrophobic coating allows for a higher initial contact angle with no external forces applied. This is because the hydrophobic coatings reduce the surface energy of the solid surface. Hydrophobic coatings are often used in consumer applications such as for windows and car windshields to allow for rain and water droplets to quickly slide off the surface. Various hydrophobic coatings such as Teflon, CYTOP, and Aquapel are also commonly used to coat microfluidic devices to allow for smoother droplet flow. Aquapel is commonly used in many, mostly passive, droplet microfluidics [108]-[110]. However, we found that for the applications in OEW, Aquapel suffers from contact line hysteresis where after creating the initial contact angle change, the contact angle becomes saturated and does not change more with light or with the switching of the voltage on and off. Teflon and CYTOP are found to be suitable hydrophobic layers for OEW applications with high contact angles [111]-[116]. The dielectric properties are very similar with dielectric constants of 2.2 and 2.1 for Teflon and CYTOP, respectively. However, CYTOP does have a higher dielectric strength than Teflon showing better long-term electrowetting performance [108]. Experimentally we did not find huge variants in droplet movement or performance for OEW applications—they both exhibit properties and contact angle changes that are similar in nature.

4.3.2 Traditional OEW vs. Co-planar OEW

Using a hydrophobic coating such as CYTOP reduces the surface energy of the solid surface, giving the 10 mS/m aqueous droplet a high initial contact angle of 110° in air for both the traditional OEW and co-planar OEW. The traditional OEW and co-planar OEW devices behaved similarly with regards to the magnitude of a droplet's contact angle change with the operating AC voltage applied and under light conditions. On both devices, aqueous droplets had a contact angle change of around 20° with the applied voltage turned on that enacts an initial electrowetting effect in the dark state. When light was incident on the devices, the contact angles were further reduced by around 10°. We will discuss how changes to individual parameters can affect the contact angle change in the light and dark states.

4.3.3 Water vs. Surfactant

For both traditional OEW and co-planar OEW devices, a 1 μL aqueous droplet mixture of deionized water with KCl to make a 10 mS/m ionic solution was used [107]. Surfactant water solutions were made with F-68 Pluronic (Sigma Aldrich, Burlington, MA) mixed with deionized water to create a 0.2% concentration. As seen in Figure 4.1, with the introduction of surfactant in the droplet, there is a significant drop in the initial contact angle by 10° due to the addition of surfactant, which reduces

the liquid-solid surface energy. However, the change in contact angle with the voltage bias on remains similar to that of water without surfactant at around 19° whereas the light effect reduces the contact angle even further by 9° as shown in Figure 4.2. Both traditional and co-planar OEW devices are capable of moving surfactant in air.

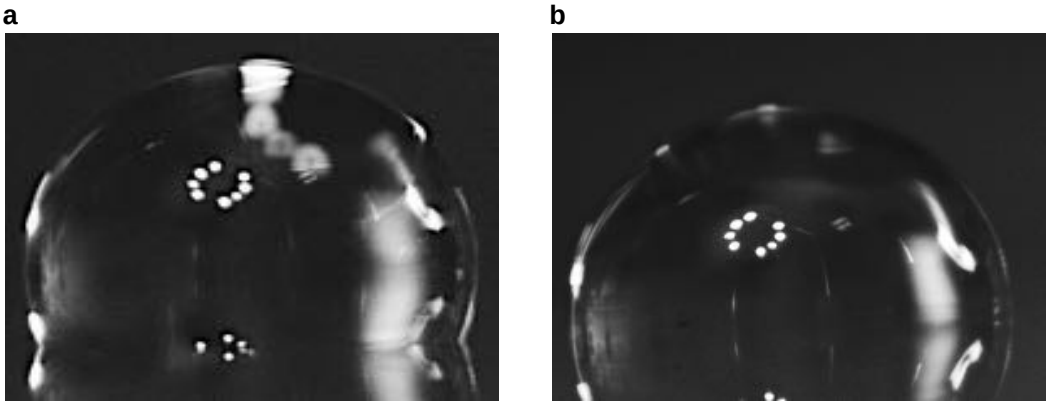

Figure 4.1 Initial contact angle for the co-planar OEW with CYTOP coating
Hydrophobic coatings such as Teflon or CYTOP reduce the surface energy of the solid surface. Because of this, they are used to create a higher contact angle of the droplet on the solid surface. Sideview images of a 10 mS/m water droplet (a) and a 10 mS/m water droplet containing 0.2% Pluronic F-68 surfactant (b) placed on an OEW device coated with CYTOP are pictured above. The water droplet in (a) has an initial contact angle of 110°. The water droplet containing surfactant has a reduced initial contact angle of 95° due to the surfactant's property of decreasing the surface energy of the droplet.

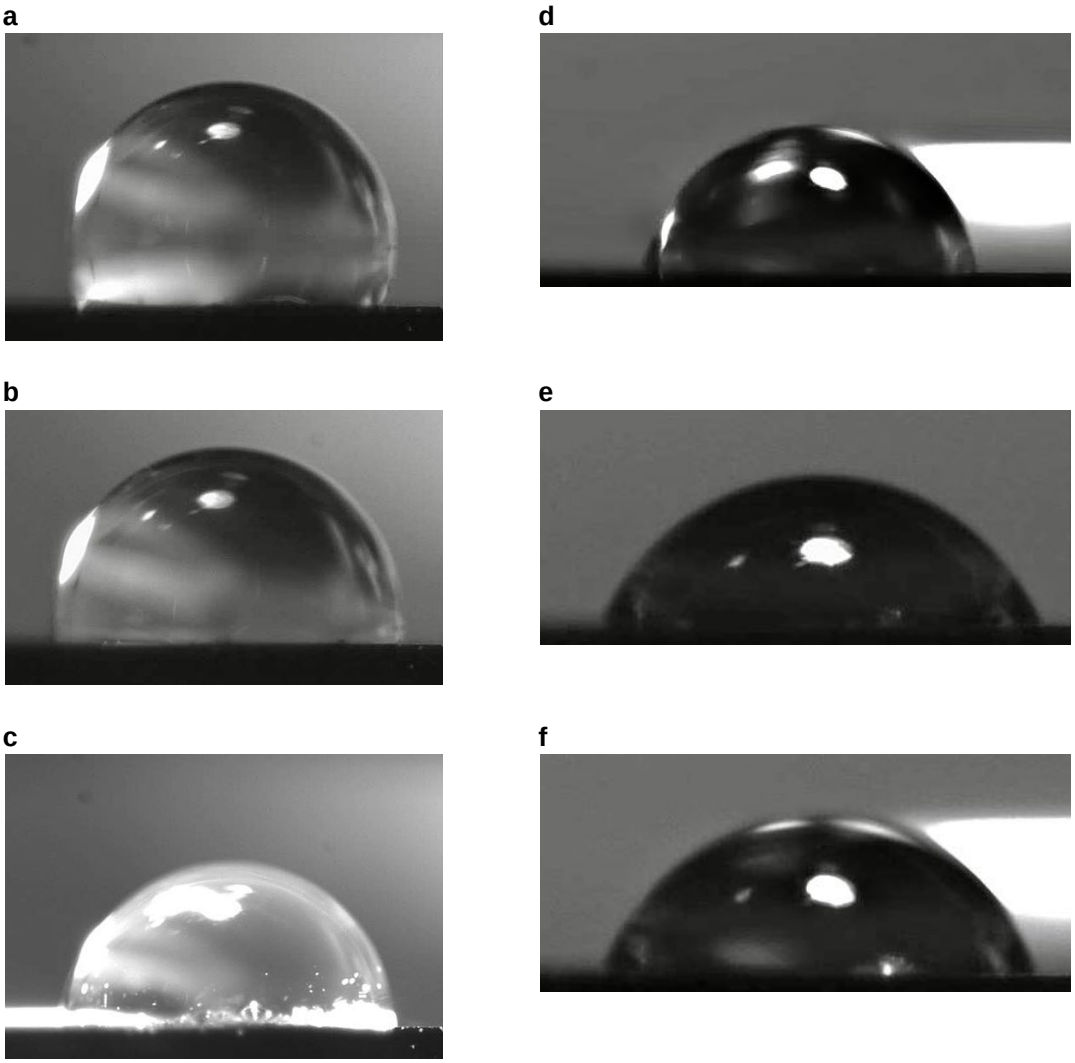

Figure 4.2 Aqueous & surfactant droplet contact angle comparisons on the co-planar OEW device
Side view images of aqueous droplets on the co-planar OEW device coated with CYTOP. Images in the first column (a)-(c) are of a 10 mS/m aqueous droplet surrounded by air in its (a) initial state (no applied voltage or light pattern), (b) dark state (applied voltage of 10 kHz, 44 V_{pp}), and (c) light state (optical pattern incident on droplet). Images in the second column (d)-(f) are of a 10 mS/m aqueous droplet containing 0.2% F-68 Pluronic surfactant surrounded by air in its (d) initial state, (e) dark state, and (f) light state.

4.3.4 Oil vs. Air

Oil as the surrounding medium is used to prevent evaporation in addition to lubricating the surface for easier movement. Part of this is facilitated by the reduction of the surface energy by the oil-droplet and oil-solid surface energy. The use of oil increases the droplet's initial contact angle on the OEW's hydrophobic surface up to around 160°. The reduction of contact angle when the operating AC voltage is applied was measured to be higher to that of air at around 23° for aqeuous droplets and 30° for droplets containing surfactant. The light effect creates an additional 13° change at the droplet's contact line.

For the purpose of our contact angle study, we tested three different oils: silicone oil (Gelest, Morrisville, PA), FC-40 Fluorinert oil (3M, Saint Paul, MN), and a mineral oil (Sonneborn, Petrolia, PA). FC-40 has a higher density than that of water at 1.85g/mL, and therefore causes the droplet to float in the oil instead of making contact with the device initially. Therefore, FC-40 is not suitable for the co-planar OEW device. Applying the initial voltage to operate the OEW devices provides enough force for the droplet to come into contact with and wet the traditional OEW device surface due to the top cover that sandwiches the droplet with the OEW chip. However, movement was not achieved although it is predicted otherwise. Mineral oil, on the other hand, has a density that is lower than that of water at 0.838 g/mL. It also has the capability of reducing the contact angle of both the traditional and co-planar OEW devices initially by 20° and 19°, respectively. With an addition of light incident on the device, the OEW effect is able to further reduce the contact angle by 18° and 8° for the traditional OEW and the co-planar OEW devices, respectively. However, movement of an aqueous droplet has only been achieved using the traditional OEW device and not on the co-planar OEW device. Mineral oil's viscosity is generally moderate around 30 cst at room temperature but the lowest viscosity mineral oil on the market is still around 15 cst at room temperature. Through experimentation, we draw the conclusion that the co-planar OEW does not generate enough force to overcome the viscosity of mineral oil whereas the traditional OEW device does. 1 cst silicone oil has a much lower viscosity than mineral oil and is similarly less dense than water at 0.971 g/mL. Droplets on the surface of traditional OEW and co-planar OEW devices both experience a contact angle change of about 20° with the initial applied voltage and another contact angle change on the order of 15° with light incident on the OEW surface. Figure 4.3 compares aqueous droplets on the traditional OEW device in air and silicone oil media. In Figure 4.4, aqueous droplets containing surfactant on the traditional OEW device in air and silicone oil media are compared. Contact angles of aqueous and surfactant containing droplets on the co-planar OEW device immersed in oil with and without an applied AC voltage are shown in Figure 4.5.

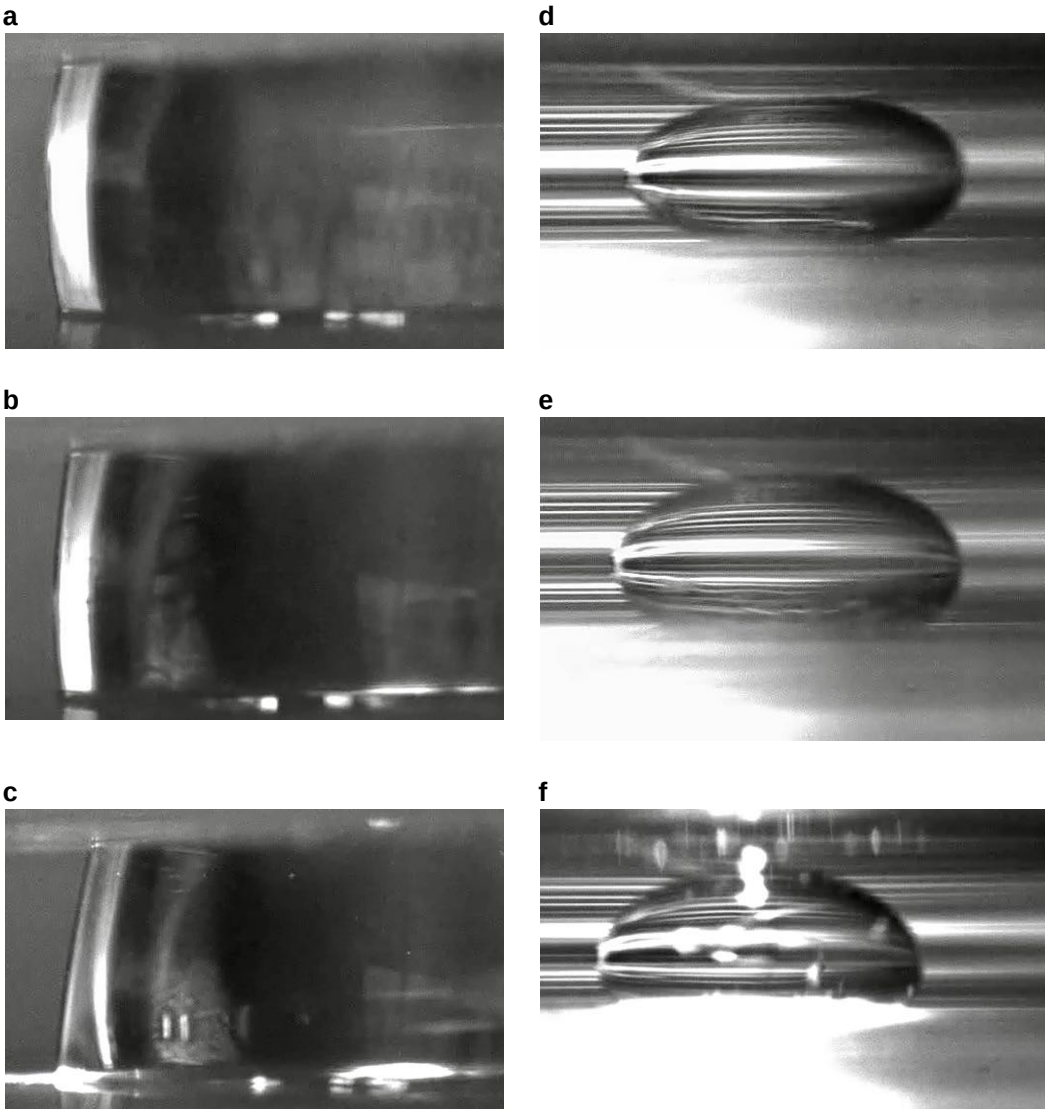

Figure 4.3 Droplet contact angle comparisons for the traditional OEW device in air vs. silicone oil Sideview images of 10 mS/m aqueous droplets on the traditional, two-plated OEW device coated with CYTOP. Images in the first column (a)-(c) are of a droplet surrounded by air in its (a) initial state (no applied voltage or light pattern), (b) dark state (applied voltage of 10 kHz, 44 V_{pp}), and (c) light state (optical pattern incident on droplet). Images in the second column (d)-(f) are of 10 mS/m aqueous droplets surrounded by 1 cst silicone oil in its (d) initial state, (e) dark state, and (f) light state.

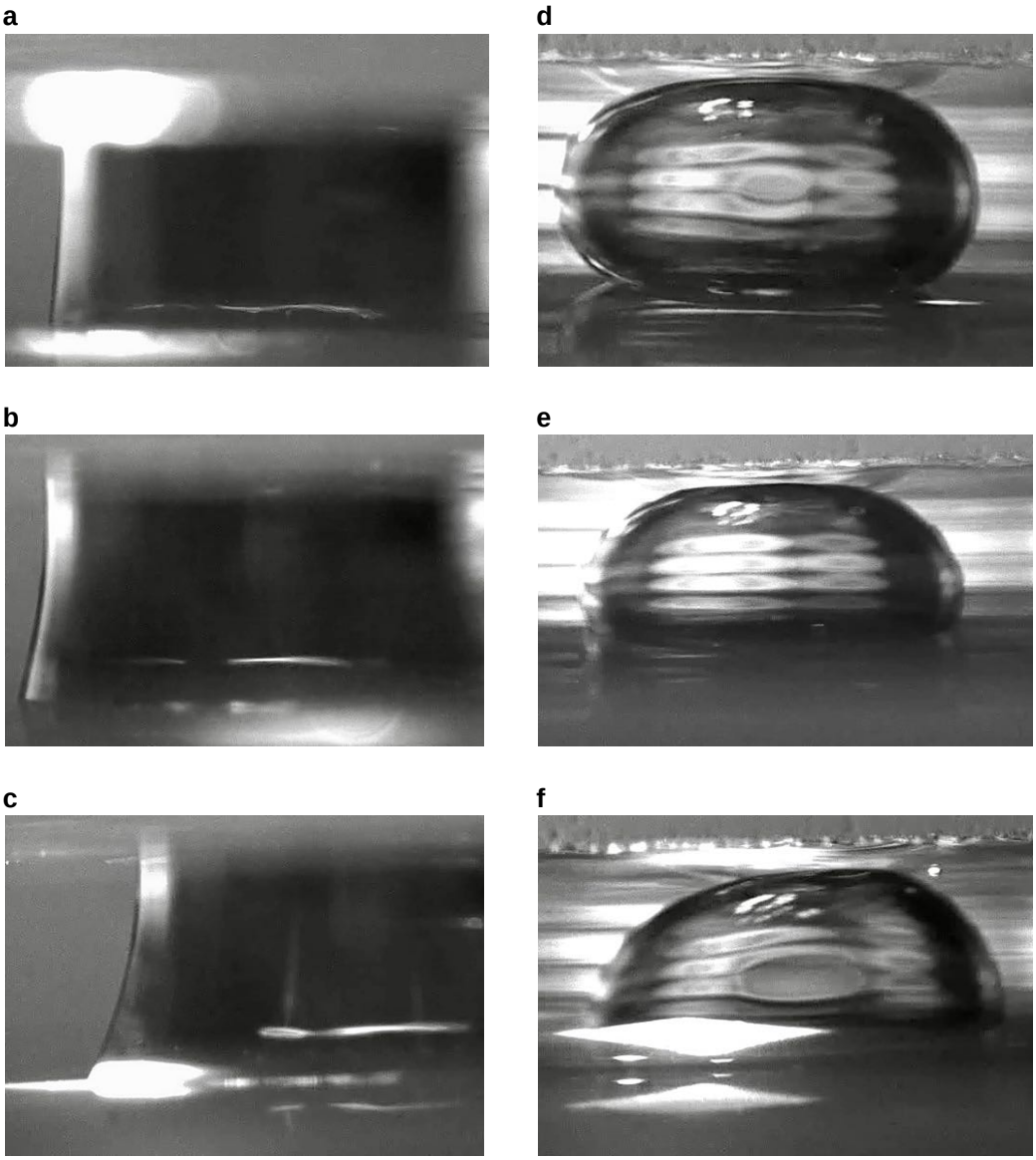

Figure 4.4 Surfactant droplet contact angle comparisons on the traditional OEW device
Side view images of 10 mS/m aqueous droplets containing 0.2% F-68 Pluronic surfactant on the traditional OEW two-plated device coated with CYTOP. Images in the first column (a)-(c) are of a droplet surrounded by air in its (a) initial state (no applied voltage or light pattern), (b) dark state (applied voltage of 10 kHz, 44 Vpp), and (c) light state (optical pattern incident on droplet). Images in the second column (d)-(f) are of 10 mS/m aqueous droplets containing 0.2% F-68 Pluronic surfactant surrounded by 1 cst silicone oil in its (d) initial state, (e) dark state, and (f) light state.

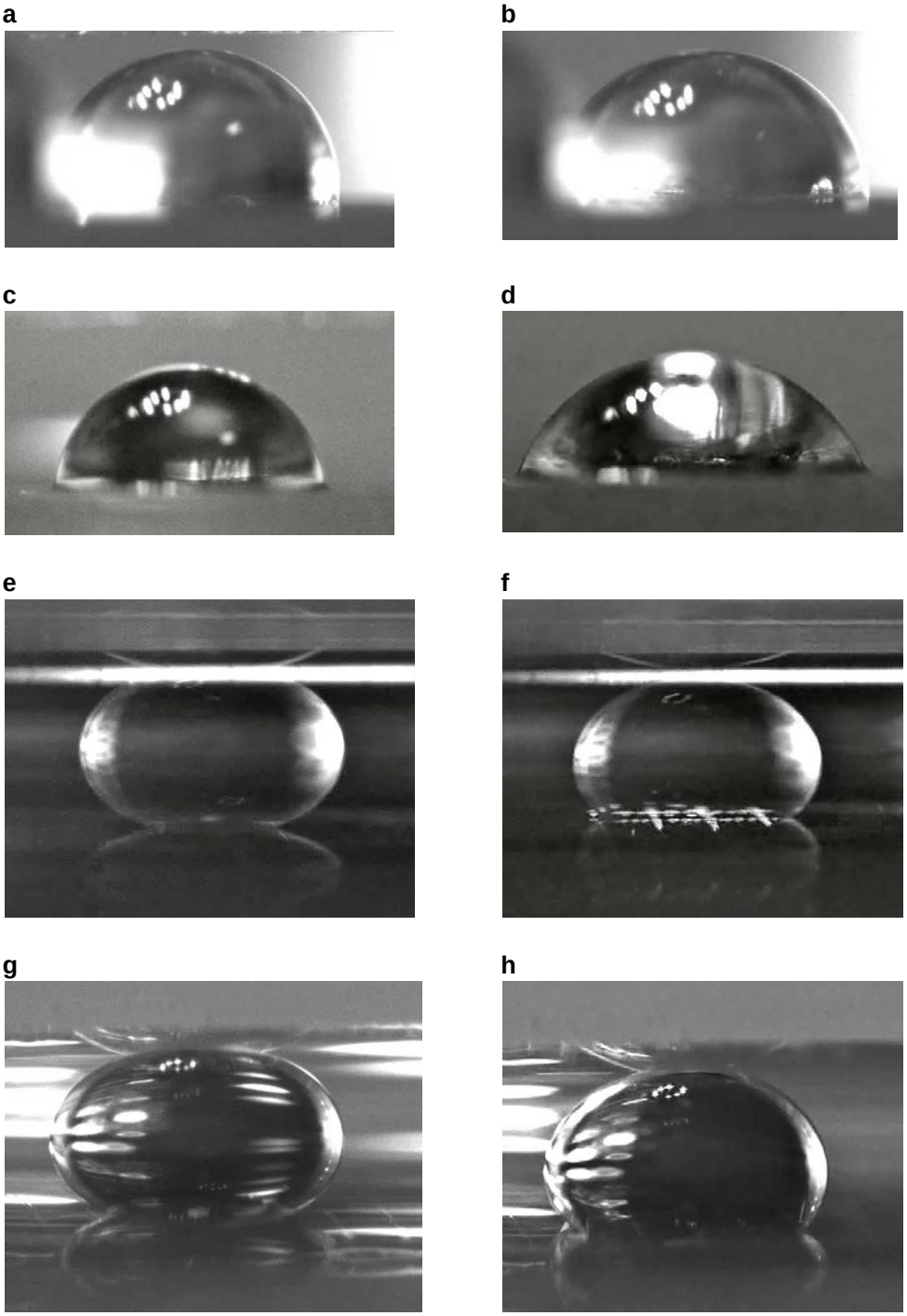

Figure 4.5 Droplet contact angle comparisons on the co-planar OEW device
Side view images of sessile droplets dispensed on the co-planar OEW surface coated with CYTOP. A 10 mS/m aqueous droplet surrounded by air without (a) and with (b) an applied AC Voltage (10 kHz, 44 V_{pp}). A 10 mS/m aqueous droplet containing 0.2% F-68 Pluronic surfactant is surrounded by air without (c) and with (d) an applied AC Voltage (10 kHz, 44 V_{pp}). A 10 mS/m aqueous droplet surrounded by 1 cst silicone oil without (e) and with (f) an applied AC Voltage (10 kHz, 44 V_{pp}). A 10 mS/m aqueous droplet containing 0.2% F-68 Pluronic surfactant is surrounded by 1 cst silicone oil without (g) and with (h) an applied AC Voltage (10 kHz, 44 V_{pp}).

4.4 Contact Angle vs. Frequency

One trend of interest is how the difference in contact angle changes with operational frequency. Previously we have studied how the peak frequency changes due to material parameters as we aim to operate the OEW device at this peak frequency to achieve faster droplet speeds. However, we want to better understand how the contact angle changes as we sweep from low to high frequencies.

The change in contact angle from Equation (4.1) has been implemented into our traditional and co-planar OEW circuit models and plotted in Figure 4.6. At low frequencies, the difference between the dark and light contact angles are very small. We do not expect to get much light effect for OEW in this regime. The absolute contact angle values of the dark and light states are the lowest at or close to DC. At high frequencies, there is little difference in the change between the light and dark state and therefore a low OEW effect is expected. In this case, the dark contact angle does not decrease as drastically at high frequencies as it did for the low frequencies. The contact angle for the light state also does not decrease as drastically in the high frequency range as it does for the low frequency range. Figure 4.7 shows side view images of droplets at 1 kHz and 100 kHz in the dark state.

However, in the mid-frequency range that corresponds with the peak frequency regime for OEW operation, the contact angles change more greatly between dark and light states. In addition, the light and dark contact angles increase more linearly with an increase in the frequency applied. The more dramatic differences between the higher dark contact angle and the lower light contact angle in this frequency range produce enough optoelectrowetting force to move a droplet.

As confirmed by the experimental data in Figure 4.8 on our co-planar OEW device, the lowest contact angles (biggest decrease) do occur at lower frequencies and the highest contact angles (smallest decrease) at high frequencies. The biggest difference in contact angles between the dark and light states occur around the 10 kHz and 20 kHz range, which corresponds to the peak frequency range for droplet movement by OEW.

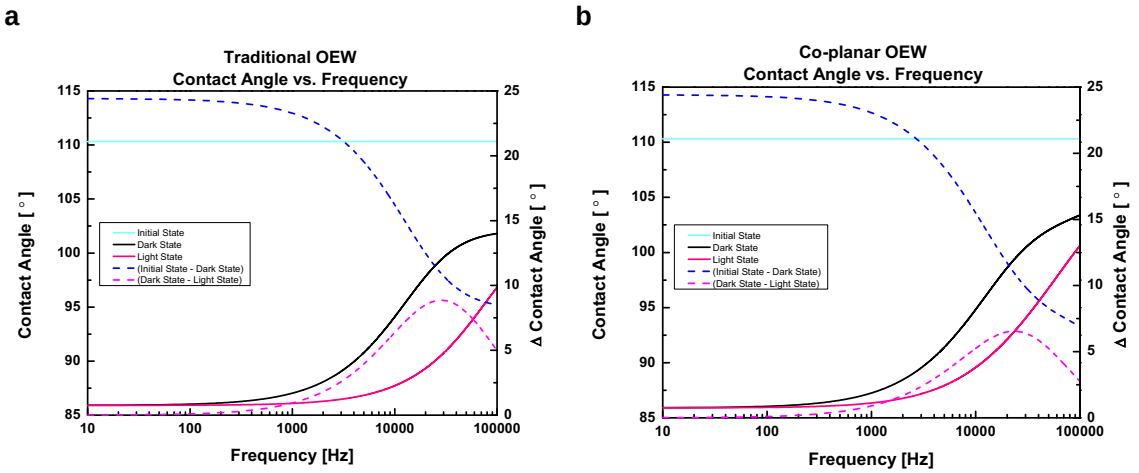

Figure 4.6 Contact angle models for traditional and co-planar OEW devices
Change in contact angle due to OEW is modeled for the traditional OEW (a) and the co-planar OEW (b) devices. For each device, water sitting on a hydrophobic coated surface is used with an initial contact angle at around 110° (initial state). The absolute contact angles (left axis) in the dark (black) and light (red) states are modeled as a function of frequency. The dashed lines correspond to the change in contact angle (right axis) when the AC voltage is initially applied to the dark state (blue) and the change in contact angle between the dark and light state (pink) for OEW force and droplet actuation.

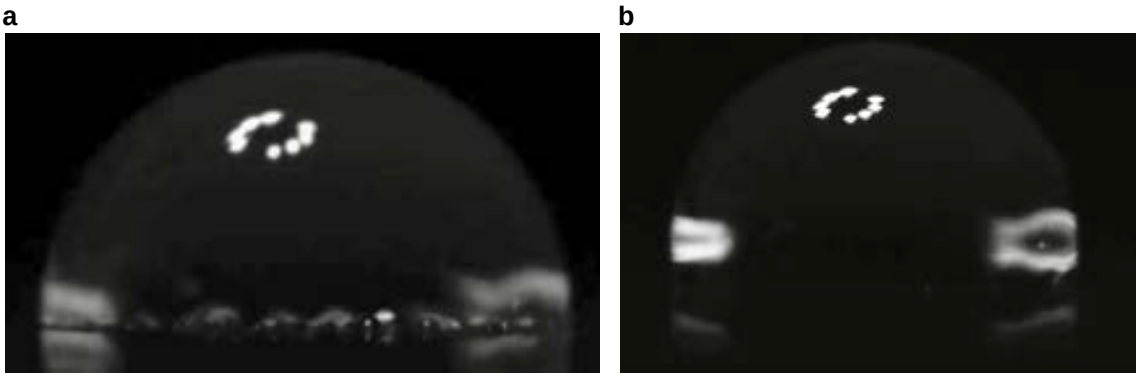

Figure 4.7 Contact angles of droplets under 1 kHz and 100 kHz
Side view images of 10 mS/m water droplets under applied an AC voltage of 44 V_{pp} at 1 kHz (a) and 100 kHz (b) under dark conditions but with ambient background room and brightfield lights on. At 1 kHz (a), the droplet's contact angle changes to 85° and at 100 kHz (b), the droplet's contact angle changes more minimally to only about 100°.

a

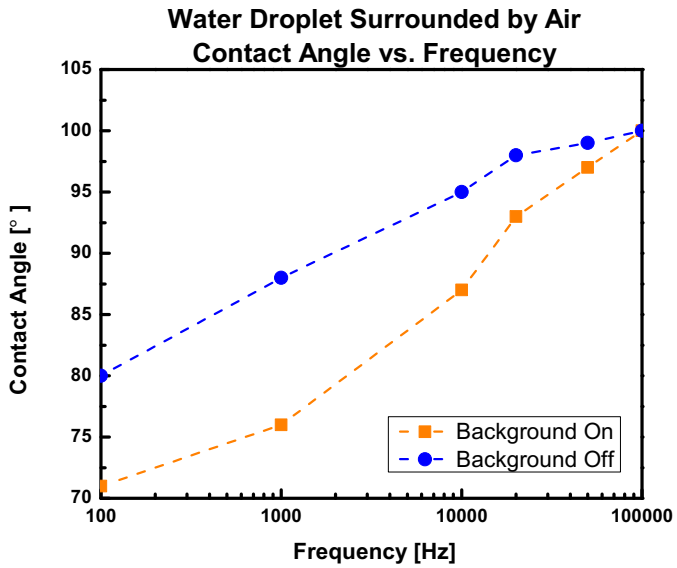

b

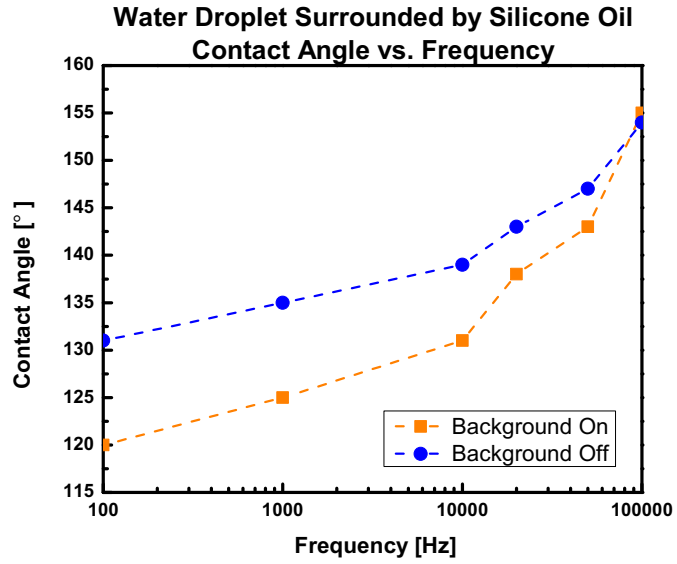

Figure 4.8 Droplet contact angle vs. frequency with and without background light in air & silicone oil Droplet contact angle is plotted against frequency for 10 mS/m water droplets in air (a) and silicone oil (b). In both graphs, droplet contact angles are measured under ambient background light (orange) and without background light (blue) to create a darker dark state.

4.5 Contact Angle Optimization

By implementing the equations that govern contact angle change due to OEW into our circuit model, we attempt to study how to optimize the operation of our device by tuning our material properties and experimental parameters.

4.5.1 Material Properties

Material and design factors that can be tuned for our co-planar OEW device to maximize the OEW force include the a-Si photoconductor layer, the Al_2O_3 dielectric layer, and the metal mesh grid line width and pitch size. As discussed in Section 3.5.2, with an increase in the a-Si thickness, more force will be generated with an increase in the amount of light absorbed. This has direct relationship to the contact angle change, where with an increase in a-Si thickness, the contact angle change between the light and dark states are expected to increase. However, this comes at the cost of requiring a more powerful light source to accommodate for absorption throughout the thicker photoconductor layer. On the other hand, the dielectric thickness is inversely proportional to OEW force as discussed in Section 3.5.1. An increase in the dielectric thickness will result in a decrease of OEW force and an overall decrease in the contact angle change between the light and dark states. However, unlike the a-Si layer, the change in dielectric layer thickness does not have as significant impact in affecting the change in contact angle for OEW operation. The effect of changing the metal mesh grid design would impact the amount of light that gets absorbed by the photoconductor due to its shielding effect. With a wider metal line, there will be a smaller contact angle change between the light and dark states due to the increase in the shunt area, reducing the operational OEW area and fill factor. On the other hand, increasing the pitch distance increases the fill factor and allows for more light to be absorbed by the photoconductor in the OEW area. Therefore, an increase in the contact angle change between the light and dark states is expected. The study of the various material properties of the OEW device structure reaffirm how the contact angle and OEW force are related and how optimization techniques presented in Chapter 3 are also applicable to physical change to the droplet's contact line.

4.5.2 Experimental Parameters

The next study we perform is to understand how altering experimental setup conditions can affect the droplet's contact angle. Experimental parameters we can tune are the applied AC voltage, the medium the droplet is immersed in, and the intensity of the light incident on the OEW device. First, applied voltage has a direct relationship with the OEW force as described in Equation (3.22). Increasing or decreasing the applied voltage directly increases or decreases the resulting OEW force in addition to increasing or decreasing the change in contact angle of the droplets in the light and dark states. Operating the OEW device at a higher voltage could,

therefore, achieve faster droplet speeds until breakdown is reached. However, operating the OEW system at a high voltage is not ideal for energy efficiency. Next, we compare the effects of air versus oil as the droplet's surrounding medium. Because the surface energy of oil allows for a larger contact angle between the droplet and the solid surface, the contact angle difference is also slightly greater in oil than in air. Droplets in oil have an initial contact angle up to 160° degrees. However, changing the medium of the filler fluid from air to oil does not affect the peak frequency nor does it hugely influence the contact angle change in the dark and light states.

One factor that can more significantly affect the change in contact angles between the dark and light states is the contrast between the projector's light and dark states. As mentioned earlier, even when the projector's pixels are all black in the dark state, there is still a minimum background light from the projector in its on state. By creating a darker dark state, we can minimize the angle change when voltage is initially applied. We studied how the background light of the projector, the ambient room lights and the USB camera microscope's brightfield can affect the difference in contact angle between the light state and the dark state. According to experimental data, the ambient room lights produce the least amount of background light compared to the microscope light and the projector's background light. However, there is only a minimal difference between the effect of the ambient room lights and the microscope's brightfield LED lights. The greatest difference in contact angles between the light and dark states is accomplished when blocking the projector's background light completely. Therefore, it is important to maintain a high contrast ratio between the light sources' "on" and "off" states and to ensure that the background level of the off state is as low as possible. We compared these empirical findings with the OEW contact angle model in Figure 4.9. With a darker dark state alone, the contact angle remains higher especially in the mid-frequency range. With an increase in light intensity for only the light state, the model suggests the contact angle in the light state can decrease even more. By increasing the overall brightness but keeping the light to dark contrast ratio the same, the OEW effect is actually reduced. On the contrary, maintaining the same contrast ratio but reducing the overall brightness has a greater OEW effect. In agreement with our empirical findings from Figure 4.8, maintaining a darker background in the dark state is an important factor for achieving a greater OEW force. Therefore, the combination of a darker background dark state and a more intense light state can increase the effects of OEW and produce a stronger OEW force for droplet actuation.

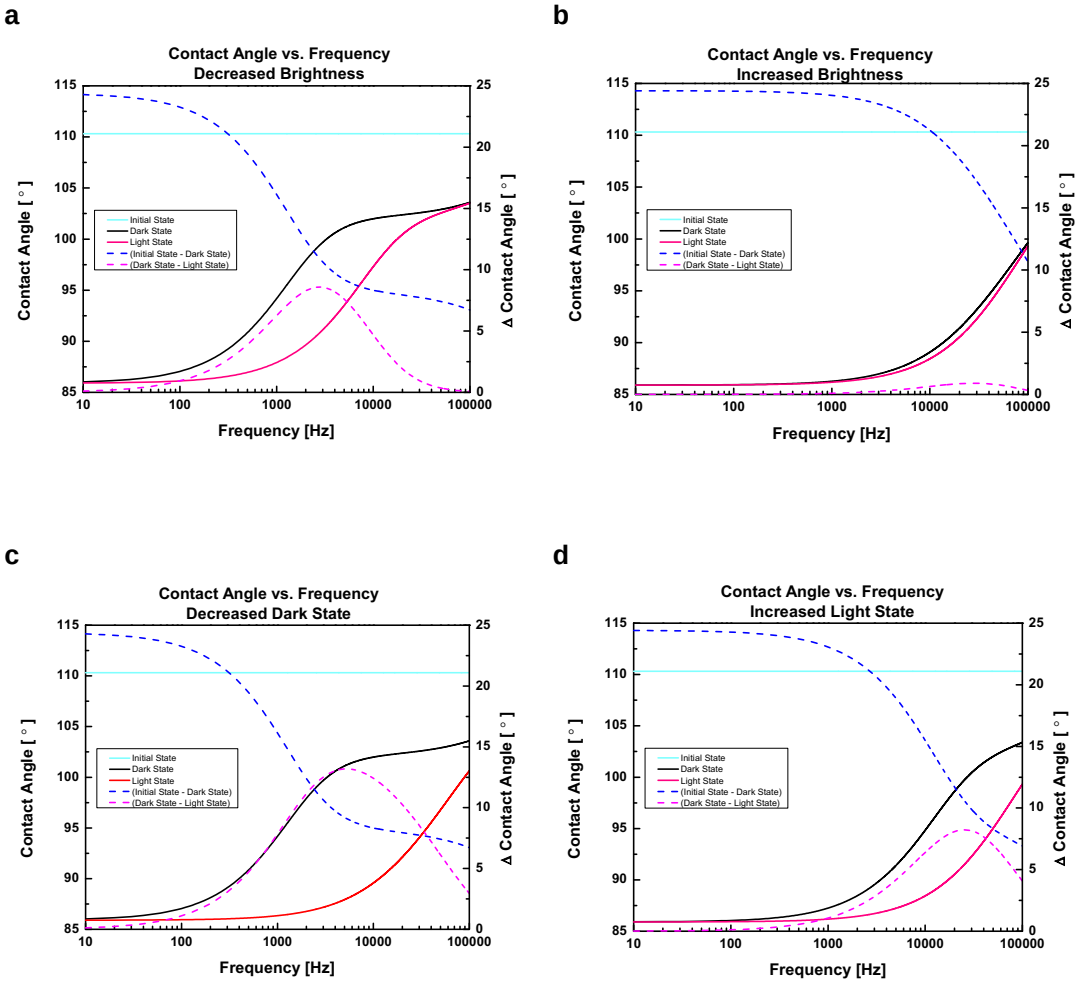

Figure 4.9 Contact angle studies with changing brightness and contrast ratios
These graphs study the effect of the dark and light state brightness and contrast ratio on the droplet's contact angle. Change in contact angle due to OEW is modeled for the co-planar OEW device for the following conditions: (a) both light and dark states absolute brightness decreases (b) both light and dark states absolute brightness increases (c) only the dark state brightness decreases (d) only the light state light increases. For these models, water sitting on a hydrophobic coated surface is used with an initial contact angle at around 110° (initial state). The absolute contact angles (left axis) in the dark (black) and light (red) states are modeled as a function of frequency. The dashed lines correspond to the change in contact angle (right axis) when the AC voltage is initially applied to the dark state (blue) and the change in contact angle between the dark and light state (pink) for OEW force and droplet actuation.

4.6 Summary

The operating principle behind droplet movement for OEW relies on the change of contact angle between the light and dark state. We have performed a thorough analysis of the OEW effect on the droplet's contact line in regard to the change in contact angle. Empirical data matches the theoretical OEW circuit model results where an initial contact angle change is observed with the modulation of an applied voltage to activate the device followed by a further contact angle decrease with light activation. The initial contact angle of a droplet is dependent on the droplet medium, surrounding medium, and the addition of a hydrophobic coating on the solid surface. A contact angle change of around 20° occurs in the dark state with the AC voltage initially applied and around an additional 10° change is observed under light conditions.

Further study of the droplet's contact angle response to varying material properties and operating conditions aids in understanding how to maximize the contact angle effect of the light state for even better OEW device performance. One significant way to do so as proposed in this study is to reduce the background dark state while also increasing the amount of light in the light state. Nonetheless, the findings of our contact angle analysis aid in improving droplet actuation and manipulation on all OEW devices.

5 Co-planar OEW Device Characterization

5.1 Introduction

In previous chapters, we have proposed and derived a detailed theoretical model for a co-planar single-sided OEW device that eliminates the need for a top cover electrode. Our theoretical model indicates that the co-planar OEW device behaves similarly to the traditional OEW device, allowing droplets to still move freely around the two-dimensional plane. With a thorough understanding of the role of electrowetting and its effect on the contact angle of a droplet's contact line, we note that the traditional OEW and co-planar OEW devices undergo similar contact angle changes, which allow for droplet movement. However, due to the metal grid ground mesh feature on the co-planar OEW device, we must analyze the experimental parameters for operating our co-planar OEW device to maximize droplet movement performance.

In this chapter, we will thoroughly discuss empirical characterizations of our co-planar OEW device based off of fabricated devices. Devices were fabricated following device structure suggestions described back in Chapter 3 for optimal theoretical device performance. The following sections will discuss approaches to optimizing droplet movement on our co-planar OEW device by varying experimental conditions such as frequency, applied voltage, and light intensity and comparing them to our theoretical findings. Basic droplet movement with speeds up to 4.5 cm/s will be demonstrated with further detailed demonstrations of droplet actuation capabilities described in Chapter 6.

5.2 Fabrication & Methods

The co-planar OEW device as shown in Figure 5.1 is fabricated using a 280 nm ITO coated glass wafer (Thin Film Devices Inc., Anaheim, CA). A 1 μm silicon photoconductor layer is deposited (Oxford Plasmalab 80plus) on top of the ITO on glass substrate, followed by a 150 nm aluminum oxide (Al_2O_3) Atomic Layer Deposition (ALD) layer (Picosun Sunale R150). However, instead of a separate top cover ground electrode under which the droplet makes contact, the co-planar OEW device has an integrated metal mesh ground network that is fabricated on top of the dielectric layer of the active OEW chip. A 50 nm gold metal mesh grid is deposited by e-beam evaporation (Ultek E-beam Evaporator). A thin 25 nm layer of CYTOP 809A (AGC Inc. Chemicals Company, Tokyo, Japan) is deposited as a hydrophobic coating.

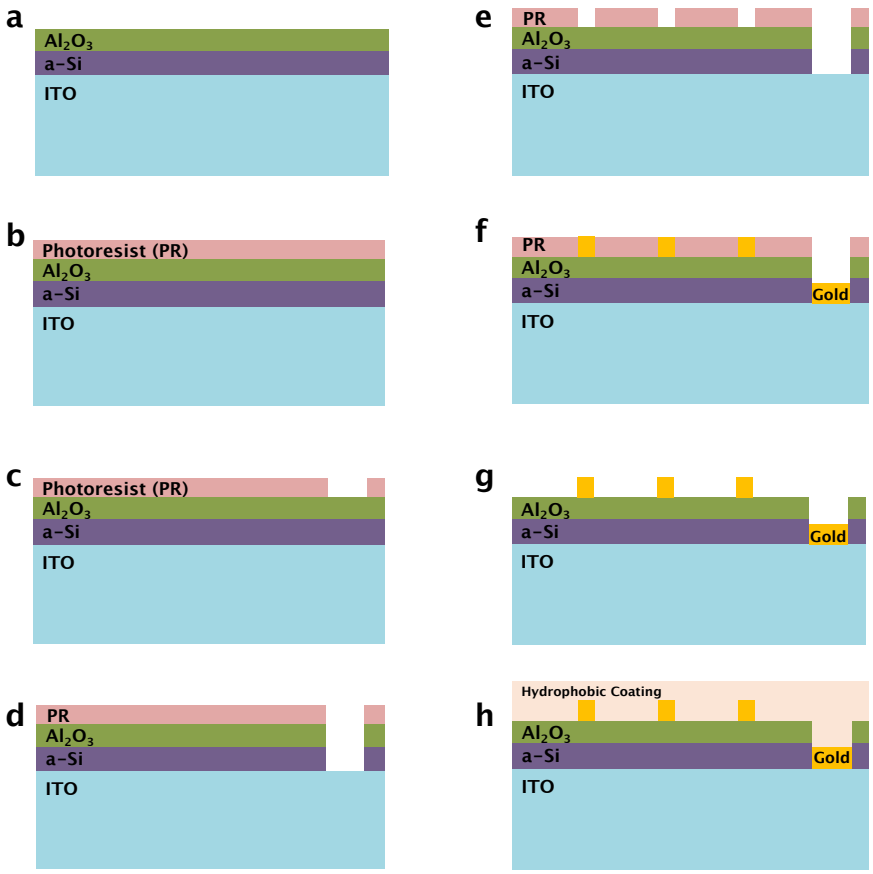

Figure 5.1 Fabrication process of the co-planar OEW device
Both traditional and co-planar OEW share the same basic fabricated structure in (a). A 1 μm a-Si layer is deposited by PECVD on an ITO coated glass substrate followed by 150 nm Al_2O_3 ALD layer deposition. In order to achieve contact to the base ITO layer, photoresist is deposited and patterned (b), (c). The alumina is etched via a 5:1 HF buffer etch, and a-Si is etched using XeF_2 (d). The metal grid patterns are created by photolithography (e) and the metal grid deposited by e-beam evaporation (f) followed by a lift off process to remove the residual photoresist (g). Lastly, a hydrophobic coating is spin coated on the whole device (h).

5.2.1 Sample Preparation

Deionized water is mixed with KCl to create a 10 mS/m solution to be used as aqueous droplets introduced using a syringe needle. Brightfield illumination and a USB microscope camera (Dino-lite Premier AM4113T) is used for visualization and recording. 1 cst silicone oil (DMS Trimethylsiloxy-terminated Polydimethylsiloxane, Gelest Inc. Morrisville, PA) is used to minimize evaporation of droplets in addition to lubricate the device surface to aid droplet movement.

5.2.2 Experimental Setup

Device activation occurs by applying an AC voltage (Agilent 33220A) between the ITO layer and the metal mesh grid contacts. This is different than the traditional OEW structure where AC voltage is applied between the ITO layer of the OEW chip and the ITO of the top cover. We generally operate our devices at 44 V_{pp} (Tegam 2348). Actuation voltage is inversely proportional to the capacitance of the dielectric layer, so voltage can be reduced by using a thinner insulator or a higher-k dielectric material as discussed in Section 3.5.2. ALD, which is how our dielectric layer is deposited, is one method to produce a high quality, conformal, pinhole free layer of dielectric with higher dielectric constants.

A consumer grade digital projector (Dell 4210X) is used to project optical patterns for OEW activation. The projected area is about 1 cm x 1.5 cm and an illuminated pixel from the projector is approximately 10 μm x 10 μm on the device. Optical patterns are generated on a computer which are outputted through the connected projector. Optical patterns for droplet movement can be composed of multiple pixels and can be customized to the size of the droplets. Contact angle experiments were performed using a CCD camera (Omron Sentech STC-MB152USB, Kyoto, Japan) to view the device and droplet's cross section. Viewing and recording were performed using software (Omron Sentech) and further image processing and analysis performed using ImageJ software (NIH Image).

5.3 Droplet Actuation Demonstration

Using the aforementioned setup described above, we experimentally demonstrate the capability of our co-planar OEW devices to actuate droplets. With a 1 μL droplet dispensed onto the device surface, we shine a square white light pattern on the OEW substrate under half of the droplet's contact line and move the droplet across our surface by moving our light pattern around the device surface. The droplet is able to follow the incident light pattern in any formation such as a square or circular light path Figure 5.2. In addition, multiple droplets can be moved in parallel. Figure 5.3 demonstrates four individual droplets being moved in circular and rectangular light paths. An overlay of the motion frames from droplet movement demonstrations to illustrate each droplet path from Figure 5.2 and Figure 5.3 are shown in Figure 5.4.

To seek the maximum velocity droplets could be actuated across the OEW surface, a 1 μL water droplet was moved across the device's surface in a straight-line trajectory. Operating our OEW devices at 44 V_{pp}, we were able to achieve a maximum speed of 2.9 cm/s, which is faster than that of the traditional two-plated OEW devices at 2.0 cm/s. One contribution to this increase in speed for co-planar OEW devices is due to the reduced shear friction contribution by the top cover. In order to optimize device operation and droplet speeds, we further analyze device operation conditions such as frequency, voltage, and light intensity.

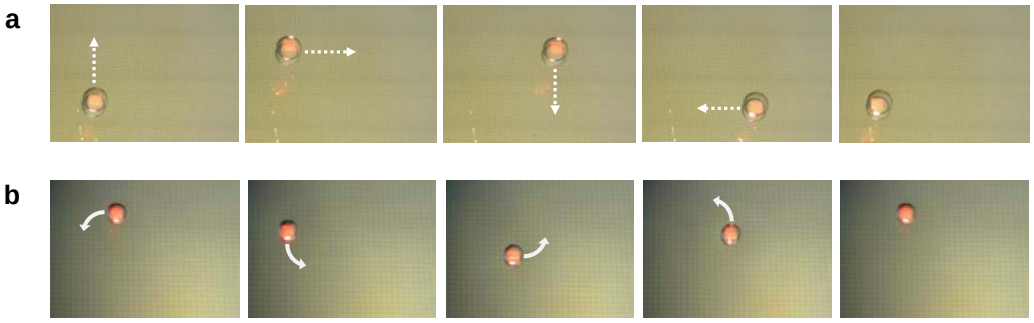

Figure 5.2 Co-planar OEW device droplet movement demonstrations
Basic movement of a single 10 mS/m 1 µL aqueous droplet is demonstrated in the time sequential images captured from above. Droplets can freely move around the two-dimensional plane in a rectangular (a) or circular (b) pattern. The demonstrations were performed on our 3 µm metal line width and 60 µm metal pitch size OEW device (a) and our 3 µm metal line width and 300 µm metal pitch size OEW device (b).

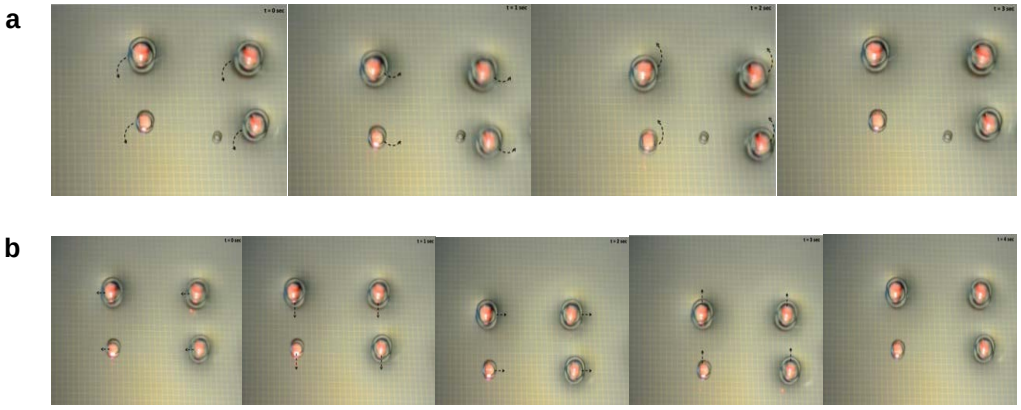

Figure 5.3 Co-planar OEW device parallel droplet movement demonstrations
Parallel movement of four 10 mS/m aqueous droplets are demonstrated in the time sequential images captured from above. Multiple droplets can simultaneously move around the two-dimensional plane in a rectangular (a) or circular (b) pattern. These demonstrations were performed on our 3 µm metal line width and 300 µm metal pitch sized OEW device.

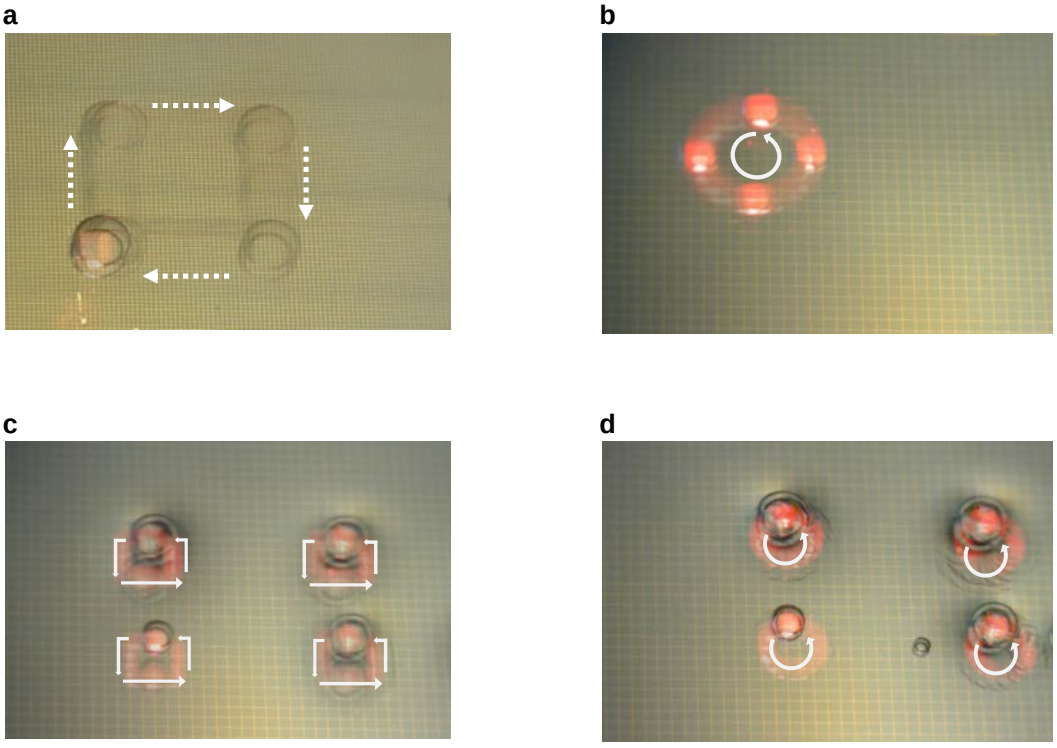

Figure 5.4 Co-planar OEW droplet movement motion overlay images
The images in this figure are motion overlay images of droplet motion paths from the same droplet demonstrations shown in Figure 5.2 (a), (b) and Figure 5.3 (c), (d). Video frames from the motion videos recorded were overlayed on each other to illustrate the rectangular and circular motion paths of the droplet demonstrations.

5.4 Force to Speed Comparison

In the following sections, we will discuss the theoretical models and vary operating conditions such as frequency, voltage, and light intensity in order to seek the maximum force for droplet movement. In our experimental studies, however, we measure the speed of the droplet.

Previously we discussed in the circuit model how to relate movement to the force imbalance to achieve droplet movement. In our experimental studies, we measure the speed of the droplet. We use speed as a figure of merit to compare to force since the force needed to move a droplet is a balance between frictional forces (fluid density, shear stress, and contact line friction) and the actuation forces generated by the OEW device (Equation (5.1)) [117]. When the droplet is in motion with zero acceleration, the frictional velocity can be calculated by setting the acceleration equal to zero and rearranging Equation (5.1) to seek out the droplet speed, v_{OEW} in Equation (5.2).

$$m\frac{d^2x}{dt^2} = F_{OEW} - F_{hysteresis} - F_{surface} - F_{contact\ line} - F_{filler\ fluid} \tag{5.1}$$

$$v_{OEW} \approx \frac{F_{OEW} - F_{hysteresis}}{(4\pi ra)+(\frac{6\mu\pi r^2}{d})} \tag{5.2}$$

where m is the mass of the droplet, F_{OEW} is the force generated by OEW, r is the droplet radius, a is the proportionality constant, μ is the droplet viscosity, and d is the droplet height.

$F_{hysteresis}$ is the initial threshold force needed to get the droplet to move. The hysteresis force is a static force that is not dependent on the velocity of the droplet. It is proportional to the contact angles with and without an applied voltage and the difference in the advancing and receding contact angles. $F_{surface}$ is the total shear force exerted by the top and bottom walls. (In the case of the co-planar OEW, the top wall plate does not exist.) It is directly proportional to the droplet's velocity, viscosity, and surface area. $F_{contact\ line}$ is the contact-line friction force which is proportional to the droplet velocity and the circumference of the droplet. $F_{filler\ fluid}$ is the viscous shear force due to the filler fluid with the assumption that the droplet is a rigid body moving through the filler fluid. It is directly proportional to the velocity squared of the droplet, the filler fluid density, drag coefficient, and cross-section of the droplet body in the filler fluid.

As discussed in Chapter 3, we model the net force per unit length and discussed how varying the metal line widths and pitches would affect our device performance. Devices with different pitch sizes of 60 μm, 100 μm, and 300 μm were fabricated with metal line widths of 3 μm. To measure the fastest droplet actuation speed, a 1 μL water droplet was dispensed on the device surface with a 1 mm layer of 1 cst silicone

oil. An optical square pattern was programmed to translate in a straight-line path across the whole width of the projector window at different speeds. The fastest speed was achieved by measuring the velocity at which the droplet could still fully follow the optical pattern. The square optical pattern was translated as fast as the program and projector limits would allow. It is possible that with a larger projection area onto the device or with faster computer and projector abilities to translate the optical pattern, even faster droplet speeds could be achieved at its peak. For the 60 µm, 100 µm, and 300 µm metal line pitches, maximum droplet speeds of 0.3 cm/s, 1.5 cm/s, and 2.9 cm/s at 44 V_{pp} and 10 kHz were achieved (Table 5.1). Figure 5.5 compares the experimental speeds to the expected peak forces for these varying metal pitch designs. We do see that this trend follows the expected model with larger pitch widths resulting in faster speeds and therefore higher forces capable of moving droplets.

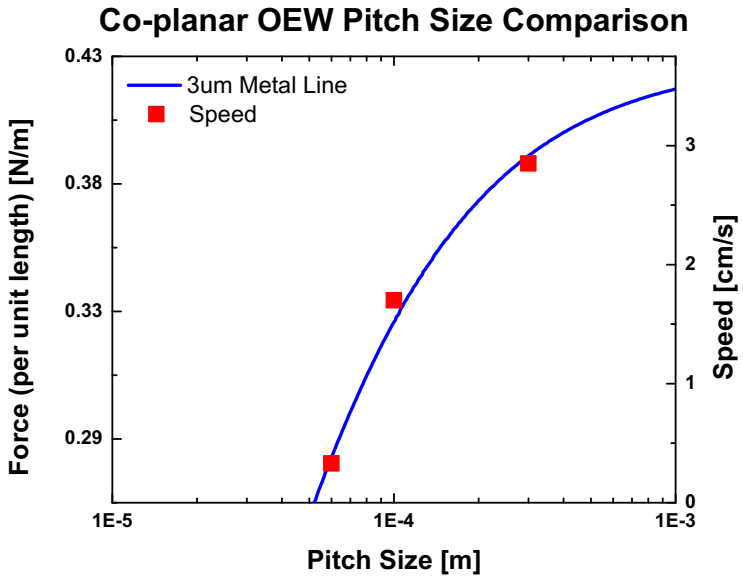

Figure 5.5 Co-planar OEW pitch size comparison
The co-planar OEW force (left axis) is plotted against the pitch size of the metal mesh grid based on the co-planar OEW model described in Chapter 3. Co-planar OEW devices with varying metal grid pitch sizes (60 µm, 100 µm, 300 µm) were designed and fabricated. 1 µL droplets were dispensed on the surface of these devices and their maximum speeds were recorded (right axis).

Pitch Size [µm]	Maximum Droplet Speed (44 Vpp, 10 kHz)
60	0.3 cm/s
100	1.5 cm/s
300	2.9 cm/s

Table 5.1 Co-planar OEW pitch sizes with corresponding maximum droplet speeds

5.5 Frequency Analysis

The fastest droplet actuation speed was measured against a range of frequencies. Since an AC voltage is required to operate the OEW devices, it is important to understand the frequency response of the OEW device. The co-planar OEW circuit model was initially used to determine the frequency response of the device and corroborated with experimental speed measurements.

A conceptual graph shown in Figure 5.6 depicts the impedances of the various key layers in the OEW structure as a function of frequency. Below a minimum critical frequency, the impedance of the dielectric layer is higher than that of the amorphous silicon in the light and dark states, preventing any difference in contact angle change in these two states and therefore preventing droplet movement. Applying a purely DC bias is also not beneficial for the device since it can also add effects of electrolysis and harm the device due to breakdown. Frequencies beyond a maximum critical frequency are not useful for optoelectrowetting operations since, at these higher frequencies, the water impedance becomes more significant compared to the dielectric impedance and thus creates a gradient electric field between the liquid medium, an effect also known as dielectrophoresis. Between the minimum and maximum critical frequencies lies the operational OEW frequency range. In this range of frequencies, the dielectric impedance is lower than the impedance of the photoconductor in the dark state, but higher than the impedance of the photoconductor in the light state. This allows for effective OEW switching between the light and dark states.

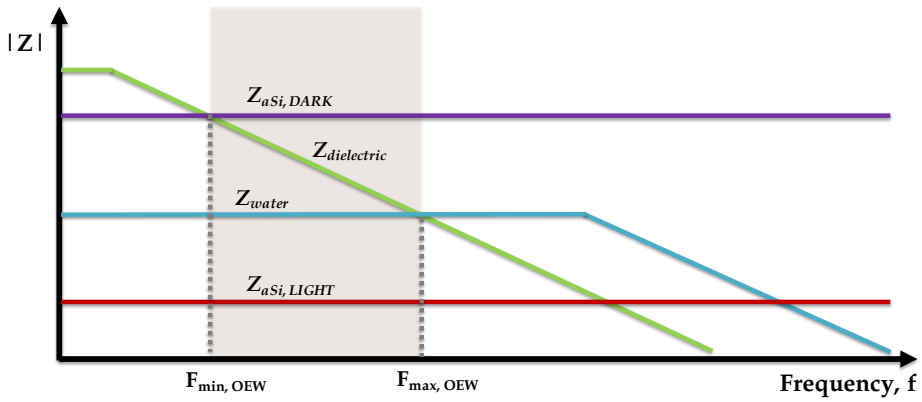

Figure 5.6 OEW operational frequency range
The operational frequency range to achieve OEW is in the shaded region noted by the minimum frequency, $F_{min,}$ and the maximum frequency, F_{max}. In this region, the impedance of the dielectric layer is greater than the impedance of the a-Si layer in the light state and less than the impedance of the a-Si layer in the dark state allowing for OEW to take effect. In frequencies lower than the minimum frequency, the dielectric impedance is greater than the a-Si layers in the dark and light states, effectively turning the device fully "on", so there is no OEW effect under illumination. For frequencies above the maximum OEW frequency, the water impedance becomes more significant than the dielectric impedance resulting in dielectrophoresis and optoelectronic tweezer operation.

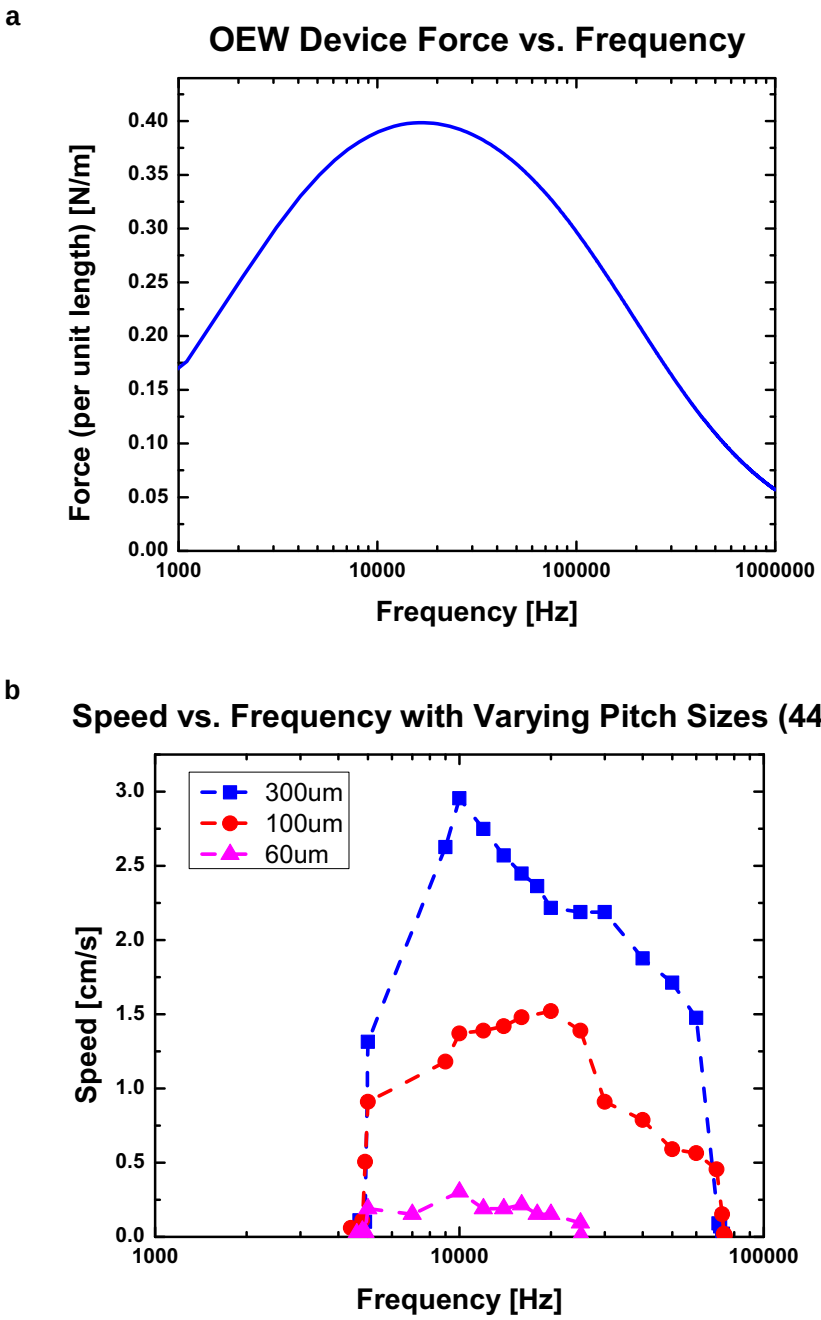

Figure 5.7 Co-planar OEW optimal frequency range
The co-planar OEW force is plotted against frequency according to the model based in Chapter 3 (a). Predicted optimal OEW performance occurs around the 10 – 20 kHz range. Co-planar OEW devices with 3 µm metal grid widths and various metal pitch sizes of 60 µm, 100 µm, and 300 µm were fabricated. 1 µL 10 mS/m aqueous droplets were dispensed and actuated to find the maximum speeds that could be achieved on these devices across a frequency range of 1 kHz to 100 kHz with an applied AC voltage of 44 V_{pp} (b). Maximum speeds for all devices occurred around 10 kHz as predicted with the 300 µm device achieving a maximum speed of 2.9 cm/s.

For experimental tests, OEW devices of varying pitch sizes (300 μm, 100 μm, and 60 μm) were used. According to the OEW circuit model in Figure 5.7, within the frequency range for OEW operation, the optimal force per unit length is achieved at a frequency around 10 kHz. Droplets with volumes of 1 μL were dispensed on chip submerged in a 1 mm thick layer of 1 cst silicone oil. Operating the OEW devices at 44 V_{pp} and varying the AC frequencies applied from 1 kHz to 100 kHz, droplet speeds peaked at 10 kHz as seen in Figure 5.7, confirming the theoretical model.

5.6 Voltage Analysis

The force per unit length of our moving contact line is highly dependent on the voltage difference across the dielectric layer with and without light incident on our device. Lower voltage operation is ideal for avoiding dielectric breakdown, safer operation, and being more energy efficient. Increasing the voltage applied to our OEW device will generate a greater OEW force. We expect that as we increase the voltage applied to our device, the droplet speed will increase until the voltage is high enough and reaches the dielectric breakdown limit.

Using the 300 μm pitch size OEW devices, a 1 μL droplet was dispensed on the surface of the OEW device submerged in a 1 mm thick layer of 1 cst silicone oil. Setting the operational frequency to the peak value at 10 kHz, droplet speed was measured as a function of applied voltage as shown in Figure 5.8. Droplet speeds increased to a maximum speed of 4.5 cm/s at 53 V_{pp} and droplet actuation was still realized at an applied voltage as low as 16 V_{pp} with a speed of 0.2 cm/s.

In addition, at different operating voltages, the droplet speed over a range of frequencies from 1 kHz to 100 kHz were also measured. The peak droplet speeds occurred around 10 kHz confirming the previous frequency analysis in Section 5.5. With an increase in voltage, there is an overall increase in speed across the full frequency range. As Figure 5.8 shows, consistent droplet movement across the full OEW operating frequency range was in between the 35 V_{pp} to 53 V_{pp} range.

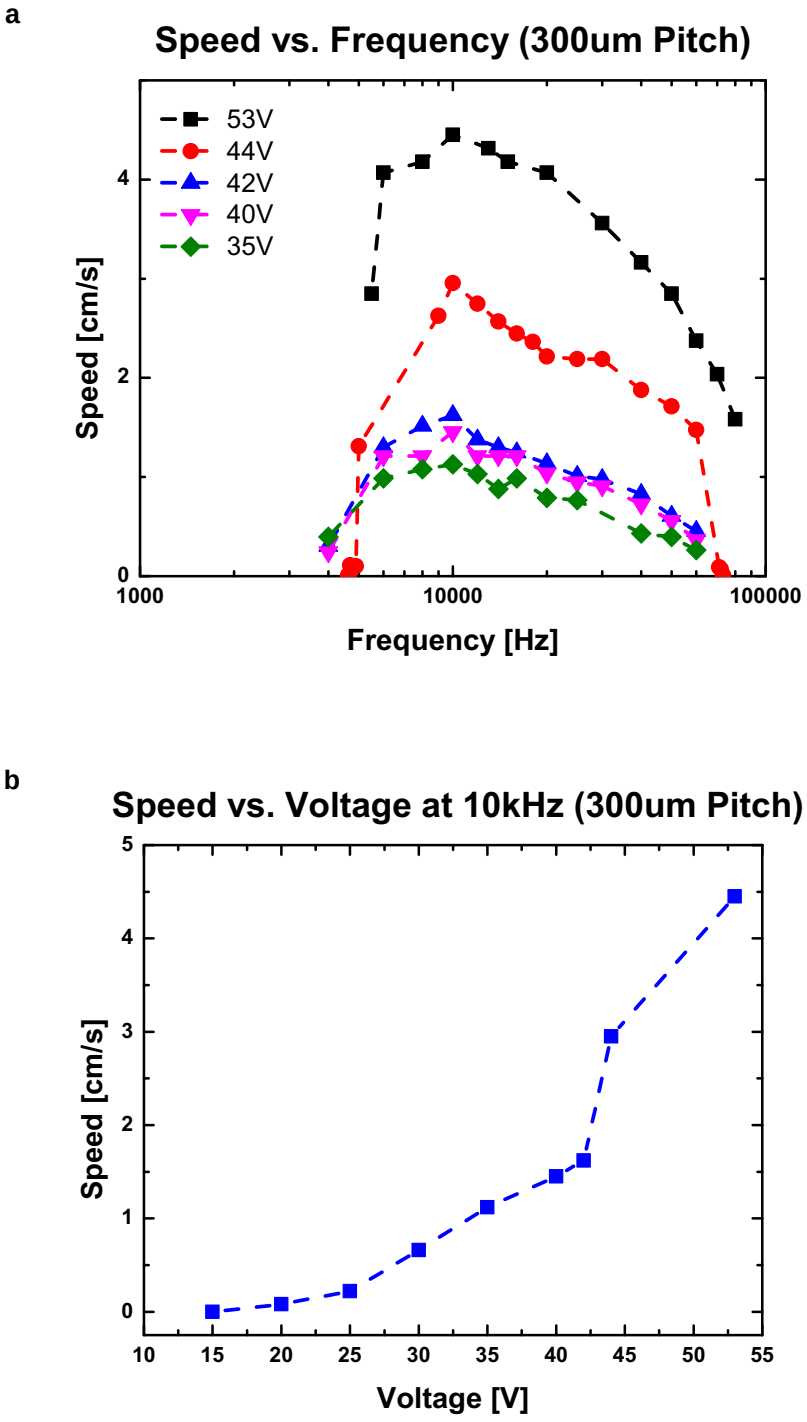

Figure 5.8 Co-planar OEW device droplet speeds with varying applied voltages
The 3 μm metal line width and 300 μm metal pitch size co-planar OEW device was used to measure maximum speeds attainable with various applied voltages across a spectrum of frequencies (a). Maximum speeds peaked at around 10 kHz across all voltages applied. With an increase of voltage, droplet speeds generally increased for the full spectrum of frequencies. Setting the applied frequency to 10 kHz, maximum droplet speeds were tested for a range of voltages (b). Droplet actuation was still realized at a voltage as low as 16 V_{pp}.

5.7 Light Intensity Analysis

In this section, the effect of light intensity on droplet actuation speed will be investigated. Due to the photoconductive nature of our amorphous silicon layer in our device structure, the amount of photocarriers generated is dependent on the incident light intensity as previously explained by Equation (2.12). At lower light intensities, lower amounts of carriers will be generated, and our amorphous silicon layer will not be as conductive compared to higher light intensities incident on our device that will generate a higher number of carriers. Therefore, with less incident light on our device, we expect less force to actuate our droplets, resulting in slower droplet speeds. Higher light intensities of light will result in a higher amount of force generated by our OEW device, and therefore, higher droplet speeds.

Faster droplet speeds are more desirable in order to process a high number of droplets in parallel and for sequential assay applications, but a high-power incident light source itself is not so ideal. High power light sources result in more heat generation thereby increasing the rate of evaporation of droplets. Too high of light power could also be harmful for certain OEW applications where live cells are encapsulated in individual droplets as the high light power can damage the cell itself. Using a low power light source is also more energy efficient and ensures safer practices by the user. Because of this, we want to study the lower limits of the light source that can still be use without compromising the operation of the OEW device.

Previous generations of OEW and their experimental setups utilized a monochromatic 5 mW laser pointer to manipulate droplets with an optical intensity of 250 W/cm^2 [40]-[42]. In order to reduce the light intensity, a commercially available DLP projector replaced the use of a higher-powered laser [50]. The projector light source (Dell 4210x) is equipped with a white light source and a measured intensity of 1.5 W/cm^2 at our device surface.

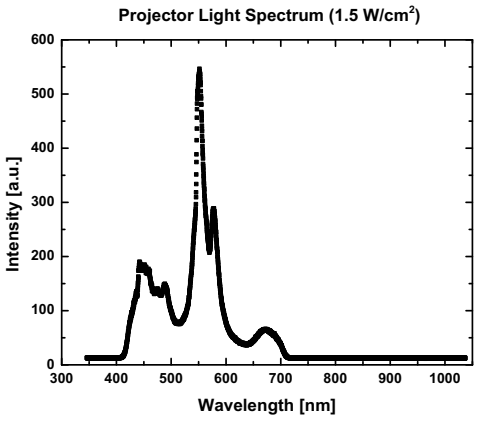

Figure 5.9 Projector light source spectrum
The output power spectrum of the projector light source (Dell 4210X) used for OEW device experimentation. The total power density from the projector output is calculated to be 1.5 W/cm^2.

In order to alter the intensity of light incident on our device, neutral density (ND) filters (Figure 5.10) were used between the projector output and the OEW device to reduce transmission of light evenly across the visible spectrum of light emitted by the projector bulb. The amount of transmission allowed by each filter can be determined by using Equation (5.3):

$$\% \text{ Transmission} = 10^{-OD} \times 100 \tag{5.3}$$

where OD is the optical density of the neutral density filter. If multiple neutral density filters are used, OD is the sum of those filter numbers.

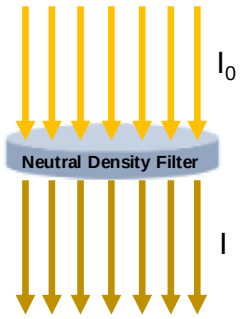

Figure 5.10 Neutral density filter schematic
A diagram of a neutral density filter. Incident light with initial intensity, I_0, passes through the filter and the light leaving the filter is reduced to intensity, I, throughout its whole spectrum. The percent of transmission allowed is determined by the filter's optical density, OD, and can be found using Equation (5.3).

To perform light intensity experiments, a 1 μL aqueous solution droplet was dispensed on the surface of our OEW device in a 1 mm thick layer 1cst silicone oil. Various ND filters or combinations of filters were used to achieve different light intensities on the device. The speed of the 1 μL droplet traveling across the OEW device for each light intensity was measured across a range of frequencies from 1 kHz to 100 kHz at 53 V_{pp} as graphed in Figure 5.11. Maximum speeds were consistently attained around 10 kHz no matter the light intensity incident on the OEW device. Droplets were still consistently and reliably able to move across a large range of frequencies on our device surface with light intensities as low as 5% transmission, or 0.075 W/cm^2. At this intensity of light, we can reach peak droplet speeds of 1.9 cm/s. Even at 16% transmission or 0.24 W/cm^2, we can achieve peak speeds of 3.3 cm/s at 10 kHz.

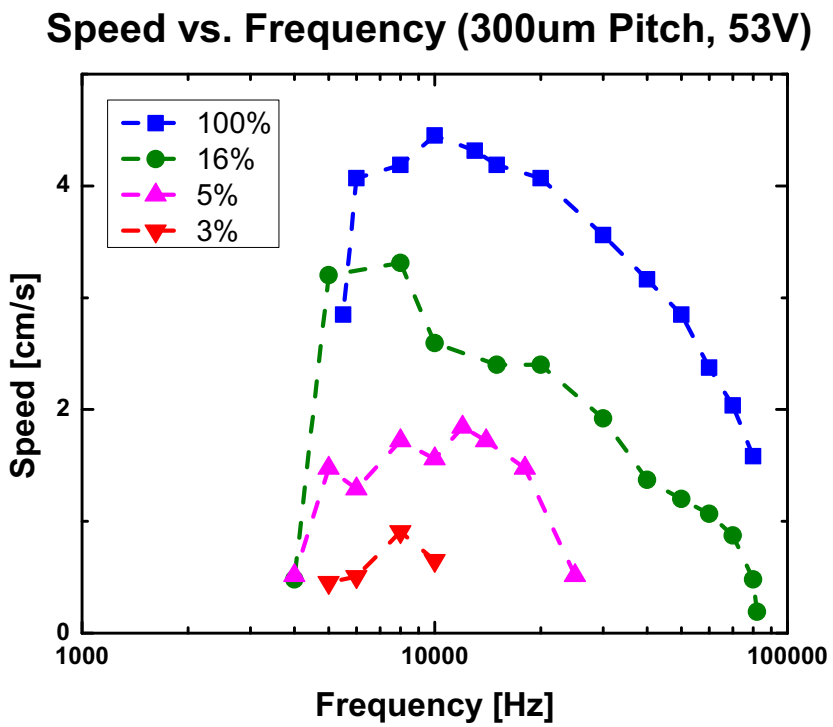

Figure 5.11 Co-planar OEW speed vs. frequency for various light intensities
Droplet speed vs. frequency is plotted for the 300 μm metal pitch size co-planar OEW device. 1 μL 10 mS/m aqueous droplets were used and operated at 53 V_{pp}. Neutral density filters with various optical densities were used, sometimes in combination, to reduce the incident light intensity on the OEW device surface. Maximum speeds of droplets were measured as a function of frequency for various respective light intensities from 100% (no filter) down to 3% light transmission.

Referencing back to Section 4.5.2, we discussed the effects of the dark and light intensities with the contact angle change. One observation made was that increasing the light intensity for the light state could increase the electrowetting effect and the contact angle change in the light state. However, lowering the dark state baseline would help lessen the initial contact angle change when the initial operational voltage is applied and help create an even bigger electrowetting effect. That is, lowering the dark state background intensity plays a key importance along with increasing the light state intensity for creating a bigger OEW effect. By using neutral density filters, we are effectively maintaining the same contrast between the light and dark states but decreasing the light intensity baseline for both states simultaneously. The lower light intensity in the dark demonstrates that droplets can still move consistently and at relatively high speeds even when the light state intensity is also lessened significantly. This indicates that the baseline of the dark intensity is indeed an important factor in addition to a bigger contrast between dark and light states.

5.8 Summary

We have presented a fabricated and operational novel co-planar OEW device. The co-planar OEW device differs from previous OEW generations with an integrated metal mesh grid on its surface. Device performance is comparable to previous generations, if not improved, with faster droplet speeds due to reduced friction from the lack of the top cover electrode. Single droplet actuation speeds on the co-planar are as high as 2.9 cm/s at 44 V_{pp} and 4.5 cm/s at 53 V_{pp} while the traditional OEW device maximum recorded droplet speed is 2 cm/s at 44 V_{pp}. Optimization of operational conditions of applied voltage, light and frequency were performed for the co-planar device to produce peak droplet speeds and movement. This novel OEW device allows for faster droplet processing and more flexible droplet system integration configurations, opening up an exciting world of application possibilities.

6 Co-planar OEW Manipulation & System Integration

6.1 Introduction

In order for digital microfluidics and microfluidics as a whole to be successful, they must be able to demonstrate utility and the ability to handle the processing techniques used in conventional biological and chemical applications. The miniaturization and automation of such applications reduces volumes of chemicals and reagents used and reduces the reaction time needed per droplet resulting in reduced costs, reduced chemical waste, higher experimental and time efficiencies, and higher throughput. With the miniaturization of droplets and the capability to handle an increased number of droplets in parallel, the ability for increased analysis can occur, allowing researchers to find solutions to problems faster. Demonstrations of previous generations of OEW device technologies have proven the ability to process droplets and to perform biological and chemical analysis with the use of basic droplet manipulations [49][50].

In the following sections, we demonstrate the versatility of the co-planar OEW device and its ability to manipulate several droplets simultaneously. We will discuss the ability for basic droplet manipulation, parallel and individualized droplet movement, and the ability to handle varying droplet volumes without changing device design. Then, we will showcase the co-planar OEW device's capabilities for macro- to micro- fluidic system integration from above and the capacity for a large-scale array of droplets. The functionalities of the OEW device prove that it is capable of handling the miniaturization and automation of biological and chemical processes currently handled by traditional benchtop and mechanical means.

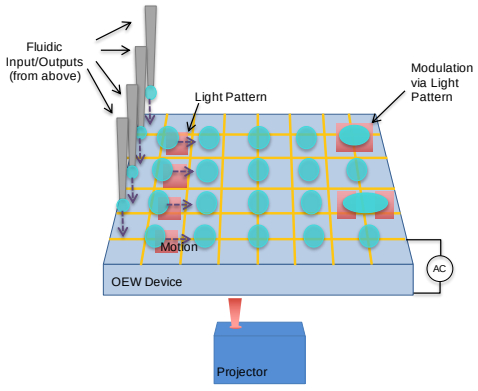

Figure 6.1 Co-planar OEW device system integration concept schematic
In this schematic, droplets are dispensed from above and moved around the chip by optical light patterns created by a digital light projector. This schematic illustrates the capability of input and output functions from above for the co-planar OEW device.

6.2 Droplet Manipulation Capabilities

As discussed throughout the preceding chapters, a droplet can move on the OEW surface as long as the droplet is in contact with the active OEW area and a metal mesh ground line. Because of this, OEW has the ability to move a droplet around the chip in not only a rectangular path, but also a circular path. This demonstrates the ability of the droplet to freely move in any path desired around the two-dimensional plane. The advantages of the co-planar OEW device does not end there. Movement of multiple droplets in parallel, also following any programmed light path configuration can be performed as demonstrated in Figure 5.4. To accommodate more droplets on the surface of the chip, additional light patterns are illuminated on the photoconductor layer by our optical projector setup by turning on various pixels on and off under the droplets. The size and movement pattern of each light pattern can be accommodated for various independent droplet sizes and paths.

Not only can individual droplets be moved about the OEW surface, but droplets can also merge with other droplets by moving two (or more) droplets towards each other. Shown in Figure 6.2, one droplet on the left is stationary while the droplet on the right moves towards and merges with it to become one larger droplet. Figure 6.3 is a side view of two droplets coming together and merging. Similarly, as seen in Figure 6.4, multiple droplets can be sequentially moved around to merge with each other. This demonstrates how we can not only merge droplets together, but also move the merged droplet that now contains a greater combined volume with the same light pattern. OEW's flexibility allows for a wide range of droplet sizes and motion paths to be moved around on its surface.

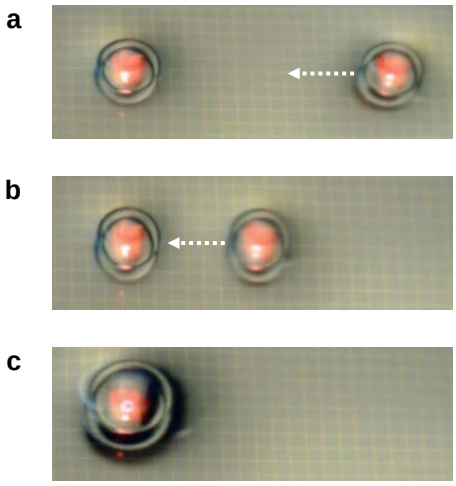

Figure 6.2 Droplet merging on co-planar OEW device
Two 1 μL aqueous droplets sit opposite from each other on the co-planar OEW surface (a). The droplet on the right is moved using a light pattern to the droplet on the left (b). The two droplets merge upon contact with each other creating a resulting 2 μL aqueous droplet (c). This demonstration was performed on our 3 μm metal line width and 300 μm metal pitch size OEW device.

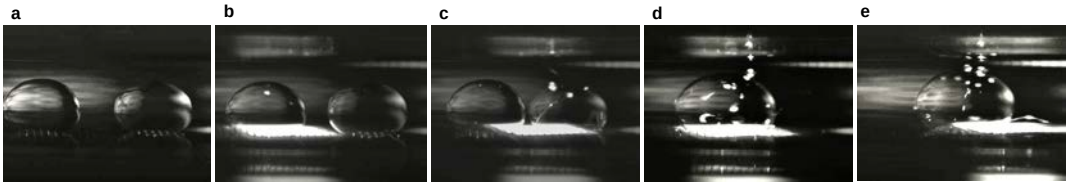

Figure 6.3 Side view of droplet merging on co-planar OEW device
This sequence of images show two 1 μL aqueous droplets merging from a side view perspective. Two droplets sit opposite of each other on the co-planar OEW device (a). The droplet on the left is moved towards the right by OEW (b), (c). The two droplets merge upon contact (d) and the resulting droplet volume moves towards the right by OEW (e).

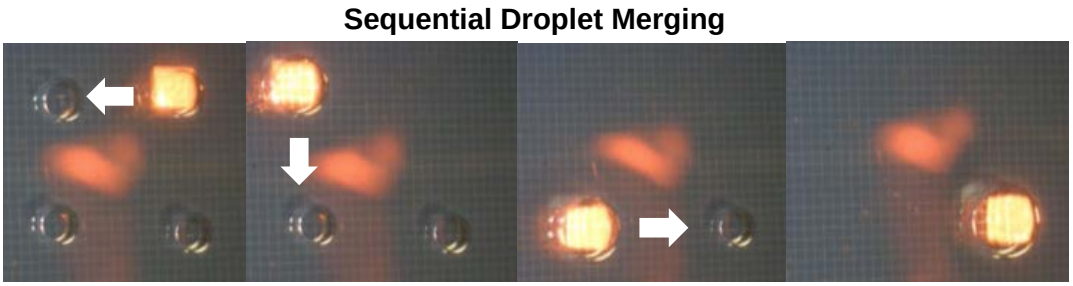

Figure 6.4 Sequential droplet merging on co-planar OEW device
Four droplets are sequentially merged and moved across the co-planar OEW device demonstrating the OEW device's ability to move and merge droplets as well as its flexibility for moving droplets of different volumes. The droplet from the top right corner is moved to the top left droplet. The resulting droplet is moved down to merge with the droplet in the bottom left and finally moved to merge with the droplet on the bottom right.

Droplets can also be moved and merged in parallel to create unique mixtures. In Figure 6.5, there are six 1 μL aqueous droplets each containing a unique dye color (McCormick Food Coloring, Baltimore, MD) of either red, yellow or blue. The column on the left contains droplets (from top to bottom) with red, blue and yellow dyed 1 μL aqueous droplets and the column on the right contains 1 μL droplets (from top to bottom) with blue, yellow, and red color dye. The two droplets from the same row (one droplet from the left column and one droplet from the right column) move at the same time towards each other. The two droplets eventually meet in the middle (in between the two columns) and combine to form a single droplet of a combined 2 μL volume. This occurs for all three rows simultaneously to form a resulting single column made out of 3 droplets with the resulting mixed colors purple (red mixed with blue), green, (blue mixed with yellow), and orange (red mixed with yellow). The mixing of the colors not only demonstrates the ability to merge droplets, but that the OEW device can support a variety of unique droplets and mixtures in parallel on our chip for further processing.

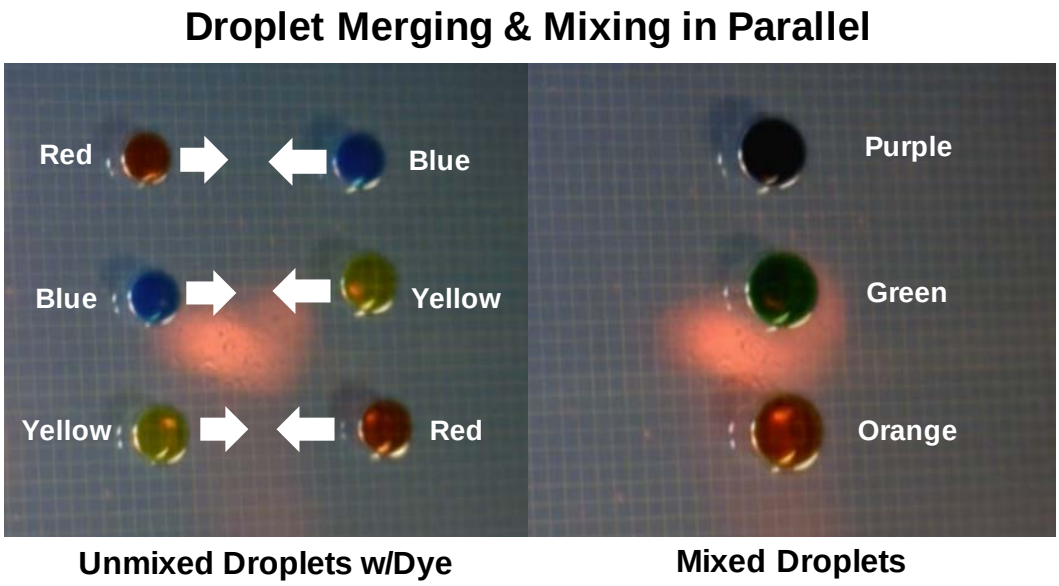

Figure 6.5 Droplet merging and mixing in parallel
Droplets on the co-planar OEW device can be moved and mixed in parallel to create unique droplet mixtures. The image on the left has two columns of droplets made up of different 1 μL aqueous droplets containing colored food dye. The left column contains droplets from top to bottom of red, blue, and yellow coloration. The right column contains droplets from top to bottom of blue, yellow and red coloration. Droplets from both columns are moved toward the center to mix together to create one column of mixed colored droplets of purple (red + blue), green (blue + yellow), and orange (yellow + red).

6.3 Preliminary Integration Example

As a preliminary example of microfluidic integration with our system, we etched microfluidic channels (300 μm x 100 μm) into a Teflon sheet using a CO_2 laser cutter (Universal Laser Systems, Scottsdale, AZ). Shown in Figure 6.6, the Teflon sheet was then mechanically bonded onto the OEW device. 10 mS/m aqueous droplets were dispensed via a syringe into the input of the channel geometry and were outputted at each of the four branches. A droplet was moved from the channel output to the center of the device area via OEW using a square optical pattern. The droplet was then manually extracted from above using a pipette. Although rudimentary, this example was the first demonstration of the capability for microfluidic integration along with open droplet access from above for our co-planar OEW device showcasing the co-planar OEW's flexibility for varied input/output configurations.

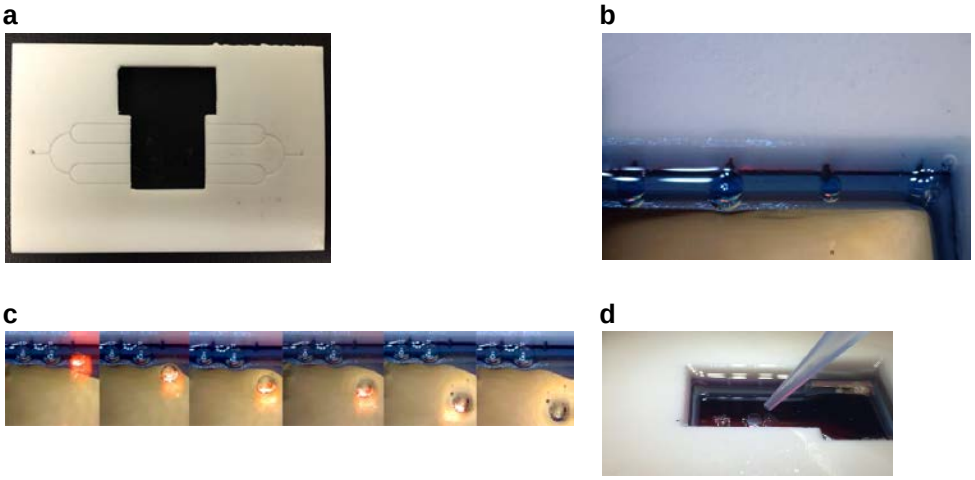

Figure 6.6 Microfluidic and extraction from above prototype demonstration
For an initial prototype, a piece of Teflon is patterned and cut to create basic microfluidic channel geometries (a). This Teflon piece is mounted onto the co-planar OEW device and 10 mS/m aqueous solution is dispensed through the Teflon channels and outputted onto the coplanar OEW device (b). An optical light pattern moves one droplet onto the center of the device area (c). The droplet is later manually extracted from above by a pipette (d).

6.4 From Above Droplet Dispensing Capabilities

One of the main advantages of the co-planar OEW device over previous generations of traditional OEW devices requiring a conductive top cover is the ability to integrate the co-planar device with a wider range of input/output capabilities. Traditional OEW devices with a conductive top plate require that input/output configurations be integrated from the sides of the device in between the OEW chip and the top plate. Although input/output configurations from the sides are feasible, it can also be more challenging and limiting than input/output capabilities without a top cover.

The co-planar OEW design eliminates the need for the top plate, which opens space above the device to implement a multitude of input/output configurations. The co-planar OEW device gives the user the ability to automate the dispensing and collection of droplets on chip from above similar to robotic techniques today while also allowing the scaling down of reaction volumes and microfluidic automation on chip. A major benefit of the open top co-planar OEW device is the ability to integrate the device with outputs from industrial and research machinery to continue downstream droplet processing on the OEW chip. One such example of this is capturing sorted cell droplets outputted by a Fluorescence-Activated Cell Sorter (FACS) machine to continue processing these droplets on the OEW chip for further study. Upstream processes performed by robust and highly developed, high throughput tools like the FACS machine have the ability to analyze various cell responses and products, but the outputted media is often disposed of afterwards or further processing of the media of

interest is transitioned and performed manually. By integrating the OEW platform with these tools, we can capture the sorted or characterized output products automatically and perform further processing on these droplets in an automated platform.

In order to utilize one of the OEW device's main benefit of having more accessible input/output configurations for downstream applications, the ability to dispense from above is demonstrated. A droplet-on-demand dispensing system was acquired (Microfab Technologies, Texas). The dispensing unit is depicted in Figure 6.7. It is composed of a piezoelectric nozzle driver that controls the volume of liquid dispensed by a proprietary controller box and software via a computer. Nozzles supplied by Microfab come in a range of diameters and are interchangeable. Reservoirs of the user's liquid are connected to the nozzle and backflow of the liquid is controlled by the pressure control box. A USB camera (Omron Sentech STC-MB152USB, Kyoto, Japan) is aligned below the output nozzle in line with a strobe light to characterize the droplet as viewed via a computer monitor and to adjust dispensing settings of the drive controller.

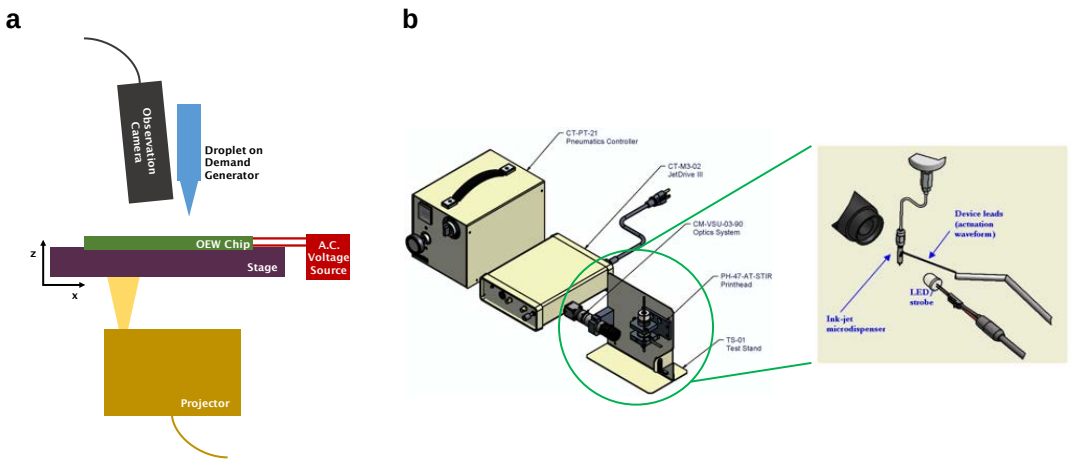

Figure 6.7 Co-planar OEW setup schematic with droplet-on-demand dispenser
A schematic of the co-planar OEW experimental setup is shown (a). The OEW chip sits above a moveable stage and is connected to an AC voltage source. Light patterns produced by a digital light projector is incident on the OEW chip from below. Above the OEW chip, a USB observation camera with built in brightfield illumination is placed next a droplet-on-demand dispenser (Microfab). A schematic of the droplet-on-demand dispenser is shown in (b) [118]. The droplet-on-demand dispenser is composed of a piezoelectric nozzle that dispenses droplets driven by the waveform generator (JetDrive) and is pressure controlled. A side view USB camera and strobe light are used to image and characterize the droplet volume dispensed by the nozzle.

A 50 µm diameter size nozzle was used to dispense individual droplets with volumes of 65 pL at a 120 Hz frequency from the droplet-on-demand system. We can customize the total volume of droplets that are dispensed on a chip by accumulating these individual 65 pL drops to form a larger volume droplet. As Figure 6.8 depicts,

we can dispense a finite number of drops, in this case 100, 1000, 10000 and 100000 individual drops, to make larger individual droplets of 6.5 nL, 65 nL, 6.5 μL and 65 μL, respectively. There are two methods of dispensing droplets on the surface of the activated OEW device. The first method is to dispense droplets on one location on the OEW surface where an optical pattern collects all the individual drops as they accumulate to form their final droplet volume. The final droplet volume is moved via OEW to a location of interest. The second method is to dispense drops directly onto the location of interest as they accumulate to a final droplet volume, using a light pattern and OEW force to attract the dispensed drops to the same location and form a larger droplet with a specified volume. This allows for precise positioning of droplets on the OEW chip. In both methods, OEW is used to accumulate and merge the individual drops being dispensed to form one larger droplet volume. The second method is generally useful when the density of droplets on the OEW surface is high such that the space available to move droplets around the surface is limited.

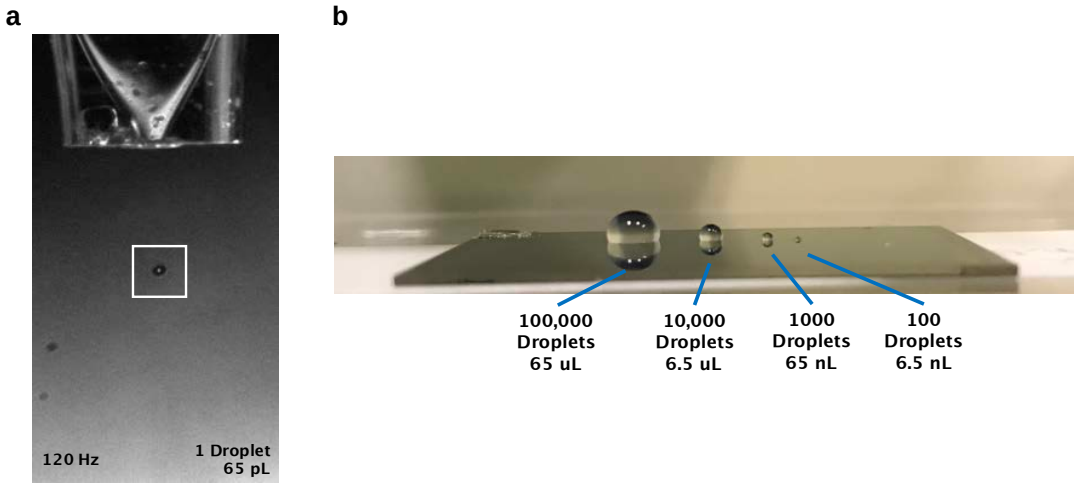

Figure 6.8 Droplet-on-demand dispensing capabilities
A still image from the side view droplet camera (a) shows the droplet-on-demand system's nozzle tip with a 65 pL aqueous droplet being dispensed. These drops can be accumulated in the same area to create a number of specified volumes desired (b). For example, 100 droplets of 65 pL accumulate to form a 6.5 nL final droplet volume.

Droplet dispensing from above and the positioning of droplets using OEW is first demonstrated in Figure 6.9. 65 nL droplets made up of 1000 accumulated drops were dispensed on the right-hand side of the OEW working area and moved via an optical pattern into position to form the University of California, Berkeley's "Cal" logo. 30 droplets in total were created and moved into formation. This demonstration shows the capability for integration from above and the ability for droplets to move freely around the co-planar OEW device plane.

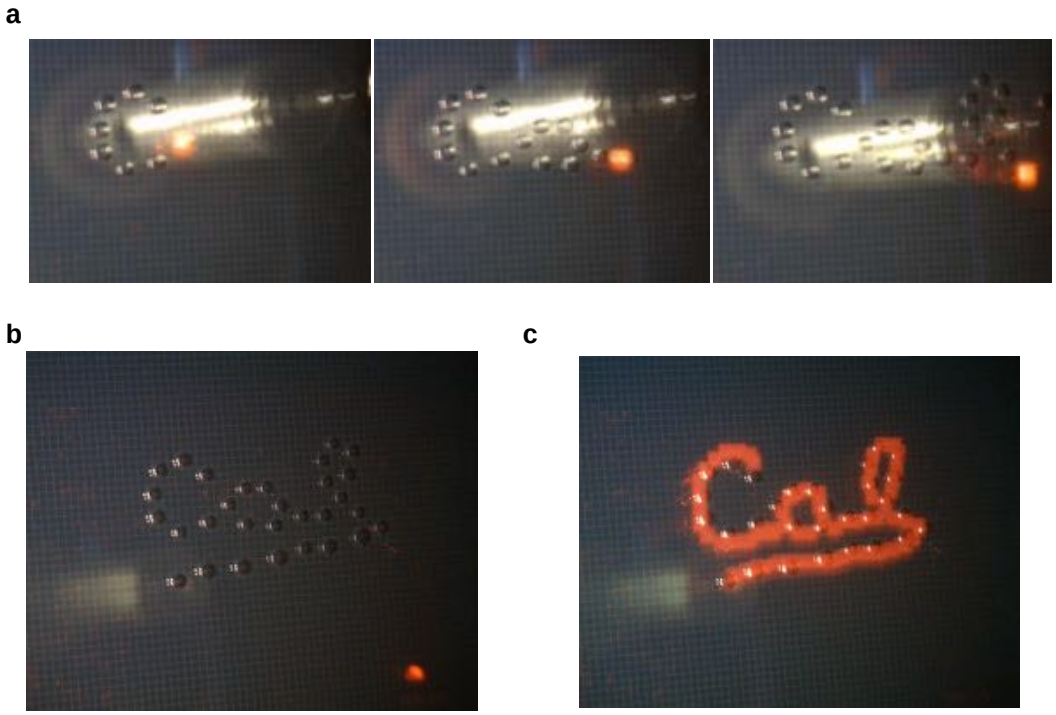

Figure 6.9 "Cal" demonstration
65 nL total volume droplets were dispensed by the droplet-on-demand system from above to the right-hand side on the co-planar OEW device's active region and moved freely device surface via OEW to form the University of California, Berkeley "Cal" Logo (a). The finished Cal logo is shown in (b) and illuminated by an optical light pattern in (c) for clarity.

6.5 Large Scale Array

One benefit of microfluidics is the ability to not only miniaturize the reaction volumes used, but also to increase the number and throughput of droplets that can be processed at the same time. Many biological and chemical assays use microplates, a rectangular array of wells used to hold small volumes of liquids that allow for reactions and experimental processing. The OEW device itself can also act as a microplate with an array of droplets sitting on the OEW surface with each droplet being its own reaction volume. The OEW device can be more flexible than conventional microplates that have a preset number of wells and well sizes since the size of the array (number of droplets) and the reaction volumes of the droplets can be customized on the OEW surface. In order to demonstrate the OEW device's ability to mimic a traditional microwell plate, we integrate the droplet dispensing technique from above by our droplet-on-demand dispensing machine with our OEW device to dispense droplets and situate these droplets into an orderly array. Each location with an individual droplet acts as an individual reaction volume similar to a reaction well in the customary microwell plates. In Figure 6.10 and Figure 6.11, an array of 100 droplets each having a volume of 65 nL were dispensed from above. Each droplet

dispensed was composed of 1000 drops of 65 pL each at a frequency of 120 Hz. In this array, the 100 droplets are fashioned into a 10 x 10 square array. Droplets were dispensed by accumulating each 65 nL droplet volume on an area to the side of the array and utilizing light patterns to move the droplet to a specified location via OEW. The red grid outline encompassing each droplet is created by the light projector from below shining a faint red pattern and is for aiding the visualization and organization the 10 x 10 array.

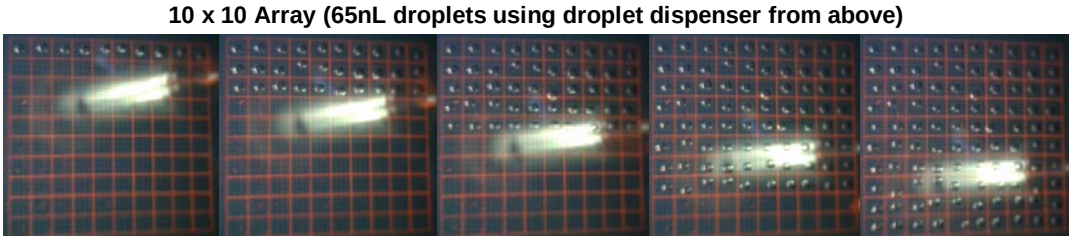

Figure 6.10 10 x 10 droplet array on co-planar OEW sequence
The progression of creating a 10 x 10 droplet array is shown. 65 nL final volume droplets were dispensed by the droplet-on-demand system from above to an area on the right hand side of the co-planar OEW device. Droplets were then moved by OEW and placed into position row by row. The red grid-like pattern is an optical pattern produced by the projector system for visual purposes.

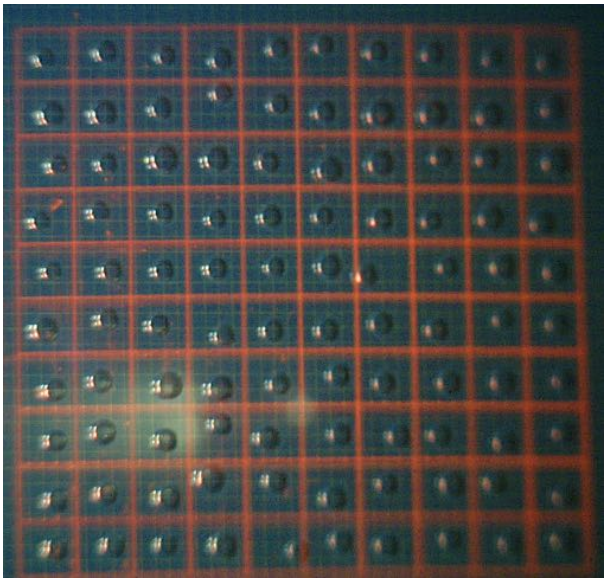

Figure 6.11 Completed 10 x 10 droplet array on co-planar OEW device
A completed 10 x 10 droplet array consisting of 100 individual 65 nL 10 mS/m aqueous droplets is shown. Droplets were dispensed by the droplet-on-demand system from above on the side of the array (not shown) and moved into an array location via OEW.

We can scale up the number of droplets that can be formed and moved to cover the area of our device. The co-planar OEW chip used in these demonstrations has an active OEW area of size 25 mm x 25 mm. Figure 6.12 shows an image of a 17 x 12 droplet array. 204 individual 10 mS/m aqueous droplets of 100 nL were dispensed using the droplet-on-demand system from above. Figure 6.13 and Figure 6.14 demonstrates the ability to increase our droplet array to fill up our whole OEW area with 400 droplets organized in a 20 x 20 array. Each droplet dispensed was composed of 1500 65 pL drops at a frequency 120 Hz to make a cumulative droplet size of 100 nL. The droplet volume for the 20 x 20 array was different than the 10 x 10 array to demonstrate how droplet volumes can vary for each experiment depending on the need. Droplets for the 20 x 20 array were dispensed by using both (1) dispensing individual drops from above and accumulating the full 100 nL droplet on the side of the array and using light patterns via OEW to move the droplet to a specified location and (2) dispensing from directly above the specified target location and using OEW to efficiently collect the individual drops to form the cumulative 100 nL droplet. The second method has an advantage when droplets are tightly spaced near each other.

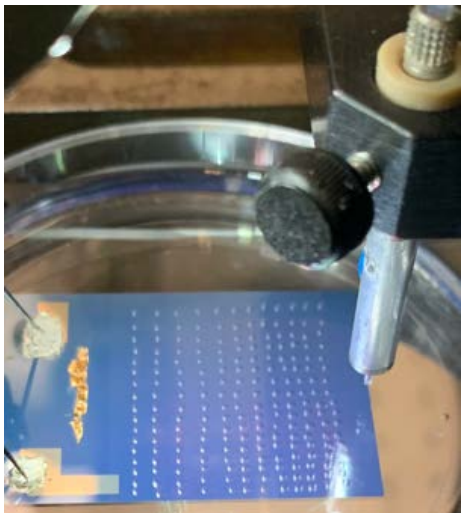

Figure 6.12 17 x 12 droplet array on co-planar OEW device
204 individual aqueous droplets were dispensed from above and placed into an array formation on the co-planar OEW device. Each droplet is 65 nL in size and made of 10 mS/m aqueous water solution.

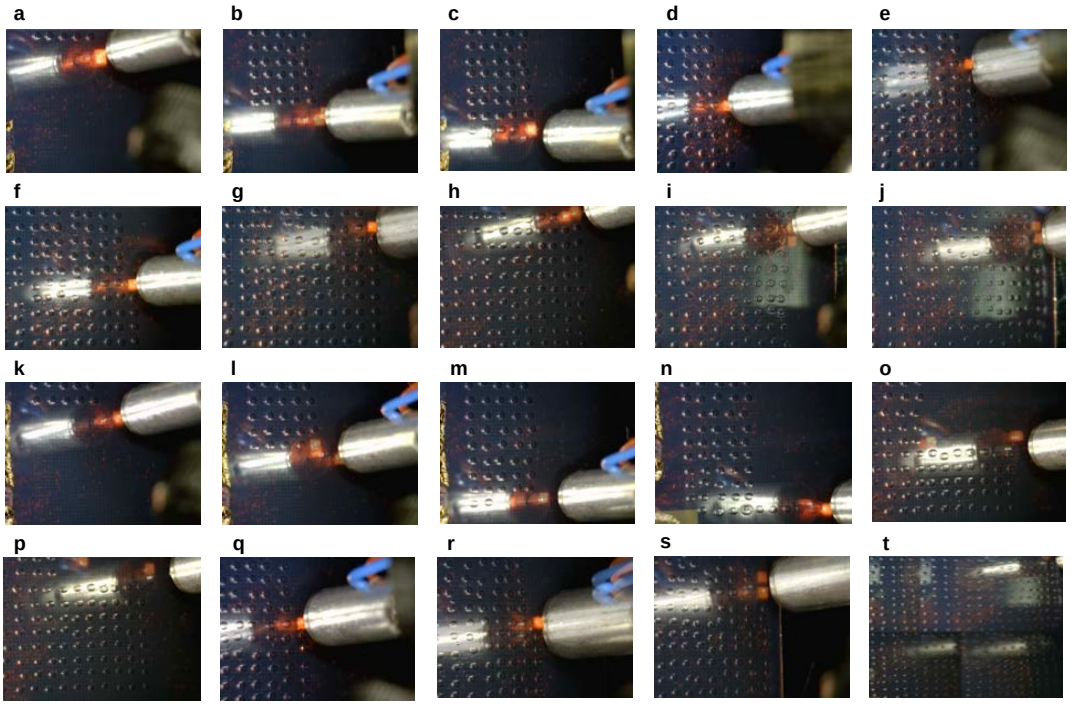

Figure 6.13 Formation of 20 x 20 droplet array on co-planar OEW
The sequence of dispensing and moving 100 nL droplets into a 20 x 20 array formation on the co-planar OEW device is shown (a)-(s). Droplets were dispensed on chip using two different methods. The first involves dispensing droplets to the side of the array and moving droplets across the device surface into its final location. The second involves dispensing droplets in close proximity to its final location and using OEW to collect the drops that form the final droplet volume and reposition the final droplet into its proper location using OEW. Both methods use OEW to collect individual drops to form a final droplet and position them into space, but the second method is preferable when droplets are more packed onto the device surface and for more accurate positioning.

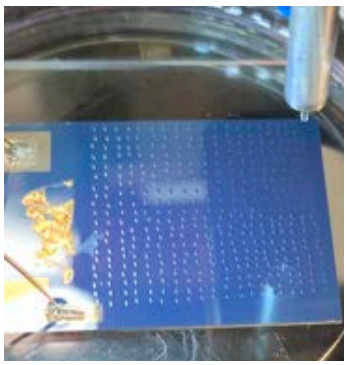

Figure 6.14 Completed 20 x 20 array on co-planar OEW device
A top view of the OEW device in its experimental setup with a completed 20 x 20 array of droplets. 400 100 nL droplets made of 10 mS/m aqueous droplets were dispensed and positioned into place via OEW in conjunction with a droplet-on-demand dispensing from above system.

The co-planar OEW device is versatile platform where droplet arrays of various number of droplets and sizes of individual droplets can be customized and actuated on the device surface. The co-planar device mimics the ability of a microwell plate while affording to bring in more configuration flexibility and further decrease the volume of liquid used. The number of droplets and size of the droplet array we can create on the chip is only limited by the size of the OEW device area. Fabricating larger OEW chips can increase the number of droplets that can be accommodated on its surface.

6.6 Dilution Capabilities

One important ability required in many biological and chemical assay protocols is the ability to dilute the concentration of a reaction volume. Dilutions are often needed in order to create solutions with certain concentrations of various components or to dilute the concentration of stock materials such as proteins, cells or antibodies. Often, dilutions are performed in a serial and stepwise manner, creating a logarithmic scale of dilution to attain a very small dilution concentration. This is because for small concentrations, mechanically trying to extract these volumes in one go is hard to control and can lead to large variance and errors in accuracy.

Competing digital microfluidic platforms such as EWOD have a limited range of dilution resolutions since the electrode is the deterministic factor for the minimum size of the droplet [119]-[121]. One method that is employed to create a dilution using EWOD is to add a volume of solute and the desired volume of dilute to form the desired concentration ratio and then split this merged volume into half as many times as needed until the volume of a single droplet is desired. However, this method results in a large volume of wasted solution. Another method that is used involves mixing one droplet of solute with one droplet of dilute for a 1:1 ratio, splitting the droplet into two, and repeating these two steps until the dilution concentration and volume is reached. However, this situation results in a finite range of dilution ratios allowed such as 1/2, 1/4, 1/8, 1/16, … etc.

Wang et al. [119] created electrode paths of differently sized electrodes to accommodate a larger range and resolution of dilution concentrations. By introducing varying droplet volumes of dilute and solute, these droplets can all be merged and then split as many times as necessary to create the desired droplet dilution concentration and volume. However, this device requires the design and fabrication of this dilution electrode pattern in addition to the pre-planning of the various combinations of electrodes and volumes used to create the specified dilution concentration and volumes.

Our OEW platform can be integrated with our droplet dispensing from above to create a finer resolution and larger range of custom dilution concentrations and volumes to suit any dilution ratio. Due to the fact that our droplet-on-demand system

dispenses many smaller drops to form a larger droplet and the OEW's innate capability to move droplets of various sizes, we can mix droplets of various and unequal volumes to make specified droplet concentrations and volumes. This customization does not come at the expense of wasting excess solution and can accommodate a wide range of volumes without adjusting any design parameters.

To demonstrate this ability, a series of dilution mixtures using colored aqueous droplets by food dye were performed. To demonstrate two different dilution methods, we used 1 μL droplets of blue and yellow food dye infused aqueous droplets that when mixed, form a green color. In the first demonstration (Figure 6.15), we mix one droplet of blue with either 1, 2 or 3 droplets of yellow. The resulting 3 droplets have either a 1:1, 1:2, or 1:3 dilution ratio with differing volumes of 2 μL, 3 μL and 4 μL. As a result, different shades of green color are seen depending on the concentration of blue mixed with yellow. Another demonstration (Figure 6.16) results in droplets with uniform final volumes by keeping the total number of 1 μL droplets mixed the same but changing the number of blue and yellow droplets used. The top merged droplet is a mixture of 3 blue 1 μL droplets with 1 yellow 1 μL droplet. The second merged droplet is a mixture of 2 blue 1 μL droplets and 2 yellow 1 μL droplets. And the third merged droplet is a mixture of 1 blue 1 μL droplet and 3 yellow 1 μL droplets. The resulting final droplets after active mixing all have volumes of 4 μL and have different gradients of green due to the differing ratios and concentrations of blue and yellow droplets that were mixed.

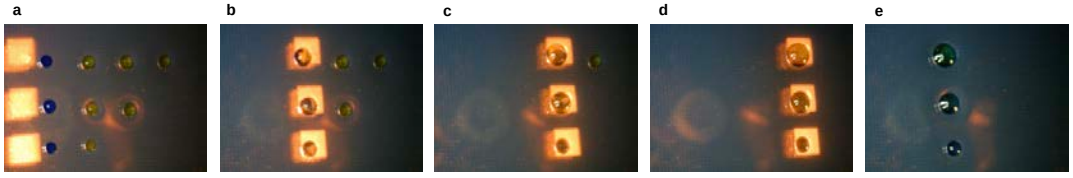

Figure 6.15 Basic dilution demonstration with differing final volumes
Three rows of 1 μL aqueous droplets were dispensed on the OEW surface. Each row contains one initial blue droplet with different number of yellow droplets to merge and mix with (a). For row 1, there contains 3 yellow droplets. Row 2 contains 2 yellow droplets and row three contains 1 yellow droplet. Optical patterns are used to move droplets from each column to merge with the droplets in the next column from the same row (b)-(d). The resulting final droplets are shown in (e) with final volumes of 4 μL, 3 μL, and 2 μL for rows 1, 2, and 3, respectively. Row 1 has a resulting blue to yellow dilution ratio of 1:3. Row 2 has a resulting blue to yellow dilution ratio of 1:2, and row 3 has a resulting dilution ratio of 1:1.

Figure 6.16 Basic dilution demonstration with same final volumes
Three rows of 1 μL aqueous droplets were dispensed on the OEW surface. In each row, differing number of droplets containing blue or yellow die are used (a). For row 1, there contains 3 blue droplets and 1 yellow droplet. Row 2 contains 2 blue droplets and 2 yellow droplets. Row three contains 1 blue droplet and 3 yellow droplets. Optical patterns are used to move droplets from each column to merge with the droplets in the next column from the same row (b)-(d). The resulting final droplets are shown in (e) with final volumes of 4 μL. Row 1 has a resulting blue to yellow dilution ratio of 3:1. Row 2 has a resulting blue to yellow dilution ratio of 1:1, and row 3 has a resulting dilution ratio of 1:3.

To implement this concept with our droplet dispensing input tool to get precise concentrations and an even finer range and smaller droplet volumes, a specified number of blue drops and yellow drops were dispensed and mixed to create various dilution concentrations, which result in different gradients of yellow, blue, and green when mixed. In the 10-droplet array shown in Figure 6.17, we have a coarser range of finite 10% increments of increasing blue concentrations mixed with yellow. In this demonstration, each droplet's final volume is 130 nL and made up of 2000 drops of 65 nL each. The number of blue and yellow drops accumulated to create each final concentration varies according to Equation (6.1). Given a fixed final volume for each cumulative droplet, the Total # of Drops dispensed by the droplet-on-demand dispenser is made up of the combined # Blue Drops and the # Yellow Drops dispensed by the droplet-on-demand system to create specified concentration. The concentration of either blue or yellow in the final droplet volume can be found by dividing the volume of blue or yellow droplets dispensed by the total droplet volume as shown in Equation (6.2).

$$\text{Total \# of Drops} = \text{\# Blue Drops} + \text{\# Yellow Drops} \tag{6.1}$$

$$\text{\% Concentration} = \frac{\text{Volume of Single Color}}{\text{Total Droplet Volume}} \times 100 \tag{6.2}$$

Figure 6.18 demonstrates a 5 x 10 array to showcase a 50-droplet gradient array that has finite 2% increments of increasing blue concentrations mixed with yellow concentrated droplets. 2000 drops were dispensed each having volumes of 6.5 pL to form a final droplet volume of 130 nL. The volumes of blue aqueous droplets and yellow droplets used to create the different concentrations are calculated by Equation (6.2).

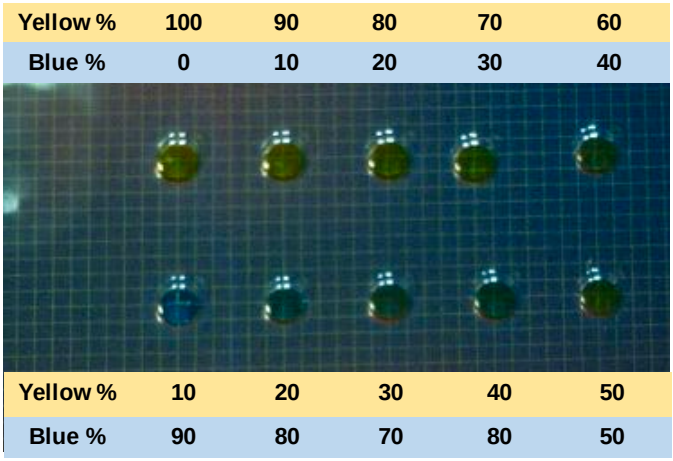

Figure 6.17 10 droplet 10% resolution dilution array
The droplet-on-demand system from above was used to dispense aqueous droplets containing blue or yellow dye. Droplets were dispensed on the co-planar OEW device to an area on the side (not shown) and moved by optical patterns into the desired locations. Variable sized blue and yellow droplets were dispensed depending on the dilution ratio desired but kept a uniform final droplet volume of 130 nL. In this droplet array, dilution resolutions of 10% were achieved.

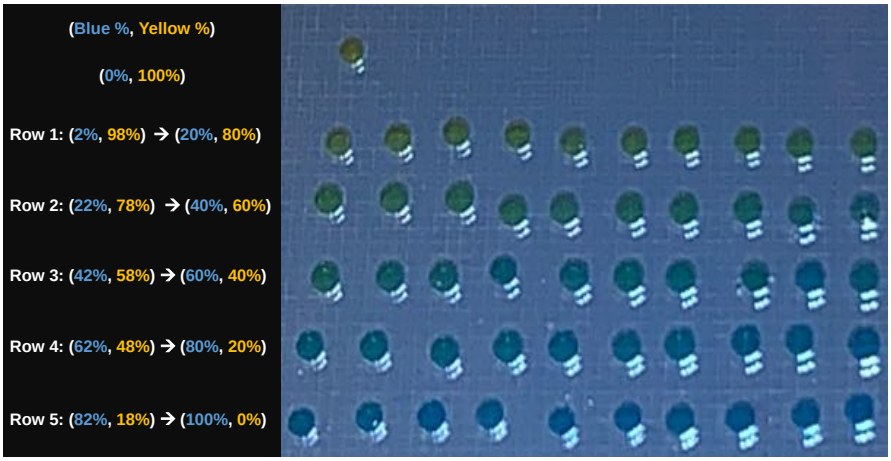

Figure 6.18 5 x 10 dilution array on co-planar OEW device with 2% resolution
The droplet-on-demand system from above was used to dispense aqueous droplets containing blue or yellow due. Droplets were dispensed using two different methods to create 50 custom dilutions in an array formation. First, blue droplets of decreasing volumes were dispensed in one area on the co-planar OEW device and moved into position on the OEW-device (starting from the bottom right of the array and ending at the upper left of the array). Then, yellow droplets of complementary volumes to create a final droplet mixture of 130 nL were dispensed directly above the blue droplets in the array to create a 50 droplet dilution array of varying blue to yellow dilution ratios with 2% resolution. As each row indicates, there is an increase in blue dye concentration (or decrease in yellow dye content) in each final droplet going from left to right and going from Row 1 to Row 5. This array demonstrates the co-planar OEW's integration capability and versatility to create custom and fine resolution dilution mixtures as well as its ability to handle customized and unique droplet mixtures simultaneously without extra design requirements.

The versatility of the OEW device to create various dilutions do not stop there. Depending on the total droplet volume and the desired solution concentration, an almost infinitesimal range of finite dilution concentrations can be created without creating excess waste and with customizable droplet volumes without further change to the OEW design or fabrication process.

6.7 Summary

Biological and chemical applications are composed of complex, multistep protocols involving the manipulation and processing of multiple droplets at the same time. In this chapter, we have demonstrated the co-planar OEW device's capabilities for parallel actuation of multiple droplets simultaneously. Each droplet on the OEW device surface acts as its own microwell reaction chamber. Multiple droplets can move freely around the two-dimensional surface plane in parallel with identical or differing motion paths, allowing for a multitude of processes to occur on chip simultaneously. Droplets can even have variable resulting volumes owing to potentially unique and independent experiments occurring all at once.

The major improvement of the co-planar OEW device over previous generations is its ability for a wider range of input/output functionalities. Dispensing of droplets from above via a droplet-on-demand dispenser demonstrates this system integration flexibility that the co-planar OEW benefits from. Droplets can be dispensed to create large scale arrays covering the whole OEW device area. These droplets can be efficiently made of varying solution dilutions to create unique reactions for applications such as large-scale library screening while being mindful of excess liquid waste. The co-planar OEW device improves upon previous OEW generations by being capable of handle a wider range of applications with ease of use and improved metrics making it a competitive lab-on-a-chip technology platform ready to be used.

7 Conclusion

This dissertation demonstrates the potential of OEW as digital microfluidic platform for lab-on-a-chip applications. The preceding chapters have illustrated the theory, design, and demonstration of OEW devices as well as introduced and demonstrated a novel co-planar OEW device that expands the flexibilities and capabilities of the OEW platform and optofluidics as a whole.

Replacing the top cover electrode in the traditional OEW device through the integration of the metal mesh onto the OEW device itself introduces greater possibilities for macro- to micro- fluidic system integration. The concept and design of the co-planar OEW still maintains OEW's key benefits of continuous movement around the two-dimensional plane without the need for complex individual electrode addressing.

A theoretical model of the co-planar OEW device was developed to better understand how the metal mesh grid affects the performance of this new generation of OEW in comparison to the traditional OEW model. Analysis gathered from the co-planar OEW model was further used to optimize the co-planar OEW device structure design for fabrication. In addition, a theoretical model of the droplet's contact angle was compared to physical observations of the droplet under the OEW effect to confirm the electrowetting effect. As our findings in this work indicate, tuning external experimental conditions such as ambient light or the optical source's contrast ratio and brightness is just as important as optimizing the device's structure design.

With the co-planar OEW device, we have demonstrated the ability for basic droplet manipulations such as rectangular and circular movement, merging of multiple droplets, ability to accommodate and move droplets of varying volumes, and individual droplet operations simultaneously in parallel. The co-planar device improves upon the traditional OEW device's droplet actuation performance with even faster speeds while maintaining its ability to carry out basic droplet manipulations. Higher droplet speeds on the co-planar OEW device achieved despite a marginal reduction in effective force compared to the traditional OEW device can be partly attributed to the reduction in friction due to elimination of the top cover.

As we have previously mentioned, the key benefit of the co-planar OEW over previous generations of OEW devices is its open top, which does not restrict droplets from being sandwiched in between two glass plates, but instead exposes droplets from above for easier access and direct methods for dispensing and extraction. We have demonstrated with a droplet-on-demand dispenser the ability to generate droplets of varying volumes from above our OEW surface and subsequently collect the droplets and move them into position on our device surface. Droplet arrays of up to 20 x 20 arrays have been accomplished on our device surface, but the co-planar OEW device is not limited there. This only suggests that the array size and packing of droplets can

be as great as the OEW area allows for. In addition, the flexibility for greater input/output controls allows the user to accomplish a large range of high-resolution dilution mixtures without excess chemical and reagent waste. All of the features and capabilities demonstrated on this co-planar OEW device reinforces the ability for the OEW platform to accommodate a whole library of reactions to occur on one chip simultaneously, greatly reducing the time to screen for analytes of interest.

By thoroughly studying and comparing the traditional OEW device and the co-planar OEW device in this work through conceptual models and experimentation, we have developed a better understanding of the device's electrical response in addition to the droplet's physical response during OEW operation. We use theoretical expectations and experimental results as feedback to better understand how to optimize our device design as well as operation conditions for future iterations and generations of OEW devices.

As demonstrated by my work and by the work of researchers before me, most basic biological and chemical benchtop techniques can be accomplished via optofluidics and, namely, the OEW platform itself. These functions are realized with added benefits of higher throughput, automation, parallel processing, less chemical volumes needed, and less chemical waste—creating a cost-effective and more time-efficient solution to a multitude of applications. The standout advantages that OEW offers such as continuous droplet movement without complex addressing schemes, the accommodation of varying and unique droplet volumes simultaneously, and low electrical and optical power requirements removes constraints of other microfluidic systems and demonstrates the adaptability of the OEW platform to a wide range of application needs. The co-planar OEW has only expanded this flexibility and range of possibilities with greater system integration capabilities. The future of OEW will be dependent on creating an even more cost-efficient and portable integrated system to aid researchers in making discoveries ranging from uncovering more about the fundamental workings of our biological and chemical world to a number of cures and treatments for diseases. By the time the next pandemic occurs to humankind, fully realized and reliable microfluidic systems including the OEW platform can be readily deployed and utilized in order to seek treatments and vaccines even faster than we can today while also curbing, if not preventing, another public health crisis.

Appendix A
Optoelectrowetting (OEW) Fabrication

The following sections will detail the fabrication process for both the traditional OEW and the co-planar OEW devices. All fabrication of devices were performed in-house at the Marvell Nanofabrication Facility at the University of California, Berkeley campus.

A.1 Traditional OEW Device Fabrication

1. A 6" diameter 700 μm thick glass wafer (Corning Eagle XG) with a 2800 ± 100Å thick layer of ITO is used (Thin Film Devices Inc., Anaheim, CA). The resistivity of the ITO layer is 10 ± 2 ohms/sq.

2. A 1 μm-thick photoconductive a-Si layer is deposited on the ITO coated side of the substrate by plasma-enhanced chemical vapor deposition (PECVD) (Oxford Plasmalab 80plus). The a-Si recipe used is: 400 sccm Ar, 100 sccm 10% SiH4:Ar, at a pressure of 900 mTorr, a temperature of 350°C, and with an RF bias of 100 W.

3. Next, a 150 nm thick layer of Al_2O_3 is deposited by atomic layer deposition (ALD) (Picosun Sunale R150) at 300°C.

4. A 25 nm 0.2% Teflon AF (Dupont, Wilmington, DE) layer is spin-coated on at 3000 rpm for 30s and subsequently baked at 150°C for 30 minutes. Alternatively, to use CYTOP as a hydrophobic coating, see Section A.3.

A.2 Traditional OEW Top Cover Fabrication

1. A 6" diameter 700 μm thick glass wafer (Corning Eagle XG) with a 2800 ± 100Å thick layer of ITO is used (Thin Film Devices Inc., Anaheim, CA). The resistivity of the ITO layer is 10 ± 2 ohms/sq.

2. A 25 nm 0.2% Teflon AF (Dupont, Wilmington, DE) layer is spin-coated on at 3000 rpm for 30s and subsequently baked at 150°C for 30 minutes. Alternatively, to use CYTOP as a hydrophobic coating, see Section A.3.

A.3 Co-planar OEW Device Fabrication

1. A 6" diameter 700 μm thick glass wafer (Corning Eagle XG) with a 2800 ± 100Å thick layer of ITO is used (Thin Film Devices Inc., Anaheim, CA). The resistivity of the ITO layer is 10 ± 2 ohms/sq.

2. A 1 μm-thick photoconductive a-Si layer is deposited on the ITO coated side of the substrate by plasma-enhanced chemical vapor deposition (PECVD) (Oxford Plasmalab 80plus). The a-Si recipe used is: 400 sccm Ar, 100 sccm 10% SiH4:Ar, at a pressure of 900 mTorr, a temperature of 350°C, and with an RF bias of 100 W.

3. Next, a 150 nm thick layer of Al_2O_3 is deposited by atomic layer deposition (ALD) (Picosun Sunale R150) at 300°C.

4. To create the contact to the ITO of the OEW substrate, photolithography is performed to prepare for the etch steps. Photoresist LOR 5A (MicroChem Corp. Westborough, MA) was spun on at 3000 rpm for 45 seconds followed by a bake for 5 minutes at 200°C. Then, 1 μm of I-line photoresist is spun on at 4100 rpm for 30 seconds. The wafer is then soft baked for 90 seconds at 90°C.

5. The photoresist is then exposed (Karl-Suss-MA6 Mask Aligner) and developed with OPD 4262 solution.

6. To etch the Al_2O_3 layer, a 5:1 buffer HF solution is used.

7. To etch the a-Si layer, XeF_2 vapor is used (Xactix Xetch XeF_2 etcher).

8. The residual photoresist is cleaned off before repeating photolithography steps 6 & 7 for the metal mesh grid patterning.

9. 5 nm of titanium followed by 50 nm of Gold is then evaporated onto the wafer surface at a pressure of 10^{-6} Torr (Ultek2 Angled Cooled Chuck E-beam Evaporator).

10. To lift-off the remaining photoresist and excess metal, the wafer is then soaked in Microposit Remover 1165 photoresist stripper (Shipley).

11. Lastly, whole wafers are diced into individual OEW chips (DAD3240 Disco Automatic Dicing Saw).

12. The hydrophobic coating of CYTOP 809A (AGC Chemicals, Japan) dissolved in CT-SOLV180 is spin-coated on at 3000s for 30s.

References

[1] Hatchett, R. J., Mecher, C. E., & Lipsitch, M. (2007). Public health interventions and epidemic intensity during the 1918 influenza pandemic. *Proceedings of the National Academy of Sciences*, *104*(18), 7582-7587.

[2] Bootsma, M. C., & Ferguson, N. M. (2007). The effect of public health measures on the 1918 influenza pandemic in US cities. *Proceedings of the National Academy of Sciences*, *104*(18), 7588-7593.

[3] Lee, V. J., Yap, J., Cook, A. R., Chen, M. I., Tay, J. K., Barr, I., ... & Cui, L. (2010). Effectiveness of public health measures in mitigating pandemic influenza spread: a prospective sero-epidemiological cohort study. *The Journal of infectious diseases*, *202*(9), 1319-1326.

[4] Kaminski, T. S., Scheler, O., & Garstecki, P. (2016). Droplet microfluidics for microbiology: techniques, applications and challenges. *Lab on a Chip*, *16*(12), 2168-2187.

[5] Streck, S., Neumann, H., Nielsen, H. M., Rades, T., & McDowell, A. (2019). Comparison of bulk and microfluidics methods for the formulation of poly-lactic-co-glycolic acid (PLGA) nanoparticles modified with cell-penetrating peptides of different architectures. *International journal of pharmaceutics: X*, *1*, 100030.

[6] Hong, L., Sesen, M., Hawley, A., Neild, A., Spicer, P. T., & Boyd, B. J. (2019). Comparison of bulk and microfluidic methods to monitor the phase behaviour of nanoparticles during digestion of lipid-based drug formulations using in situ X-ray scattering. *Soft Matter*, *15*(46), 9565-9578.

[7] Liu, Y., & Jiang, X. (2017). Why microfluidics? Merits and trends in chemical synthesis. *Lab on a Chip*, *17*(23), 3960-3978.

[8] Streets, A. M., & Huang, Y. (2013). Chip in a lab: Microfluidics for next generation life science research. *Biomicrofluidics*, *7*(1), 011302.

[9] Meltzer, M. I., Cox, N. J., & Fukuda, K. (1999). The economic impact of pandemic influenza in the United States: priorities for intervention. *Emerging infectious diseases*, *5*(5), 659.

[10] Bloom, E., De Wit, V., & Carangal-San Jose, M. J. (2005). Potential economic impact of an avian flu pandemic on Asia.

[11] James, S., & Sargent, T. C. (2006). *The economic impact of an influenza pandemic*. Canada Department of Finance.

[12] Demirguc-Kunt, A., Lokshin, M., & Torre, I. (2020). The sooner, the better: The early economic impact of non-pharmaceutical interventions during the COVID-19 pandemic. *World Bank Policy Research Working Paper*, (9257).

[13] Keogh-Brown, M. R., Wren-Lewis, S., Edmunds, W. J., Beutels, P., & Smith, R. D. (2010). The possible macroeconomic impact on the UK of an influenza pandemic. *Health economics*, *19*(11), 1345-1360.

[14] Borse, R. H., Behravesh, C. B., Dumanovsky, T., Zucker, J. R., Swerdlow, D., Edelson, P., ... & Meltzer, M. I. (2011). Closing schools in response to the 2009 pandemic influenza A H1N1 virus in New York City: economic impact on households. *Clinical Infectious Diseases*, *52*(suppl_1), S168-S172.

[15] Keogh-Brown, M. R., & Smith, R. D. (2008). The economic impact of SARS: how does the reality match the predictions?. *Health policy*, *88*(1), 110-120.

[16] Sander, B., Nizam, A., Garrison Jr, L. P., Postma, M. J., Halloran, M. E., & Longini Jr, I. M. (2009). Economic evaluation of influenza pandemic mitigation strategies in the United States using a stochastic microsimulation transmission model. *Value in Health*, *12*(2), 226-233.

[17] Holm, G., Snape, J. R., Murray-Smith, R., Talbot, J., Taylor, D., & Sörme, P. (2013). Implementing ecopharmacovigilance in practice: challenges and potential opportunities. *Drug safety*, *36*(7), 533-546.

[18] Convery, N., & Gadegaard, N. (2019). 30 years of microfluidics. *Micro and Nano Engineering*, *2*, 76-91.

[19] Gravesen, P., Branebjerg, J., & Jensen, O. S. (1993). Microfluidics-a review. *Journal of micromechanics and microengineering*, *3*(4), 168.

[20] Whitesides, G. M. (2006). The origins and the future of microfluidics. *Nature*, *442*(7101), 368-373.

[21] Streets, A. M., & Huang, Y. (2013). Chip in a lab: Microfluidics for next generation life science research. *Biomicrofluidics*, *7*(1), 011302.

[22] Chiu, D. T., deMello, A. J., Di Carlo, D., Doyle, P. S., Hansen, C., Maceiczyk, R. M., & Wootton, R. C. (2017). Small but perfectly formed? Successes, challenges, and opportunities for microfluidics in the chemical and biological sciences. *Chem*, *2*(2), 201-223.

[23] Manz, A., Graber, N., & Widmer, H. Á. (1990). Miniaturized total chemical analysis systems: a novel concept for chemical sensing. *Sensors and actuators B: Chemical*, *1*(1-6), 244-248.

[24] Thorsen, T., Maerkl, S. J., & Quake, S. R. (2002). Microfluidic large-scale integration. *Science*, *298*(5593), 580-584.

[25] Song, H., Chen, D. L., & Ismagilov, R. F. (2006). Reactions in droplets in microfluidic channels. *Angewandte chemie international edition*, *45*(44), 7336-7356.

[26] Di Carlo, D., Wu, L. Y., & Lee, L. P. (2006). Dynamic single cell culture array. *Lab on a Chip*, *6*(11), 1445-1449.

[27] Mejía-Salazar, J. R., Rodrigues Cruz, K., & Materón Vásques, E. M. (2020). Microfluidic Point-of-Care Devices: New Trends and Future Prospects for eHealth Diagnostics. *Sensors*, *20*(7), 1951.

[28] Wen, N., Zhao, Z., Fan, B., Chen, D., Men, D., Wang, J., & Chen, J. (2016). Development of droplet microfluidics enabling high-throughput single-cell analysis. *Molecules*, *21*(7), 881.

[29] Schneider, T., Kreutz, J., & Chiu, D. T. (2013). The potential impact of droplet microfluidics in biology. *Analytical chemistry*, *85*(7), 3476-3482.

[30] Yeh, E. C., Fu, C. C., Hu, L., Thakur, R., Feng, J., & Lee, L. P. (2017). Self-powered integrated microfluidic point-of-care low-cost enabling (SIMPLE) chip. *Science advances*, *3*(3), e1501645.

[31] Jebrail, M. J., Luk, V. N., Shih, S. C., Fobel, R., Ng, A. H., Yang, H., ... & Wheeler, A. R. (2009). Digital microfluidics for automated proteomic processing. *JoVE (Journal of Visualized Experiments)*, (33), e1603.

[32] Psaltis, D., Quake, S. R., & Yang, C. (2006). Developing optofluidic technology through the fusion of microfluidics and optics. *Nature*, *442*(7101), 381-386.

[33] Clausell-Tormos, J., Lieber, D., Baret, J. C., El-Harrak, A., Miller, O. J., Frenz, L., ... & Holtze, C. (2008). Droplet-based microfluidic platforms for the encapsulation and screening of mammalian cells and multicellular organisms. *Chemistry & biology*, *15*(5), 427-437.

[34] Srinivasan, V., Pamula, V. K., & Fair, R. B. (2004). Droplet-based microfluidic lab-on-a-chip for glucose detection. *Analytica Chimica Acta*, *507*(1), 145-150.

[35] Hua, Z., Rouse, J. L., Eckhardt, A. E., Srinivasan, V., Pamula, V. K., Schell, W. A., ... & Pollack, M. G. (2010). Multiplexed real-time polymerase chain reaction on a digital microfluidic platform. *Analytical chemistry*, *82*(6), 2310-2316.

[36] Chang, Y. H., Lee, G. B., Huang, F. C., Chen, Y. Y., & Lin, J. L. (2006). Integrated polymerase chain reaction chips utilizing digital microfluidics. *Biomedical microdevices*, *8*(3), 215-225.

[37] Wheeler, A. R., Moon, H., Bird, C. A., Ogorzalek Loo, R. R., Kim, C. J. C., Loo, J. A., & Garrell, R. L. (2005). Digital microfluidics with in-line sample purification for proteomics analyses with MALDI-MS. *Analytical Chemistry*, *77*(2), 534-540.

[38] Barbulovic-Nad, I., Au, S. H., & Wheeler, A. R. (2010). A microfluidic platform for complete mammalian cell culture. *Lab on a Chip*, *10*(12), 1536-1542.

[39] Choi, K., Ng, A. H., Fobel, R., & Wheeler, A. R. (2012). Digital microfluidics. *Annual review of analytical chemistry*, *5*, 413-440.

[40] Chiou, P. Y., Moon, H., Toshiyoshi, H., Kim, C. J., & Wu, M. C. (2003). Light actuation of liquid by optoelectrowetting. *Sensors and actuators A: physical*, *104*(3), 222-228.

[41] Chiou, P. Y., Chang, Z., & Wu, M. C. (2008). Droplet manipulation with light on optoelectrowetting device. *Journal of Microelectromechanical Systems*, *17*(1), 133-138.

[42] Chiou, P. Y., Park, S. Y., & Wu, M. C. (2008). Continuous optoelectrowetting for picoliter droplet manipulation. *Applied Physics Letters*, *93*(22), 221110.

[43] Pei, S. N., Valley, J. K., Neale, S. L., Jamshidi, A., Hsu, H. Y., & Wu, M. C. (2010, January). Light-actuated digital microfluidics for large-scale, parallel manipulation of arbitrarily sized droplets. In *2010 IEEE 23rd international conference on micro electro mechanical systems (MEMS)* (pp. 252-255). IEEE.

[44] Chiou, P. Y., Ohta, A. T., & Wu, M. C. (2005). Massively parallel manipulation of single cells and microparticles using optical images. *Nature*, *436*(7049), 370-372.

[45] Hsu, H. Y., Ohta, A. T., Chiou, P. Y., Jamshidi, A., Neale, S. L., & Wu, M. C. (2010). Phototransistor-based optoelectronic tweezers for dynamic cell manipulation in cell culture media. *Lab on a Chip*, *10*(2), 165-172.

[46] Chiou, P. Y., Ohta, A. T., Jamshidi, A., Hsu, H. Y., Chou, J. B., & Wu, M. C. (2006). Light-actuated AC electroosmosis for optical manipulation of nanoscale particles. In *Proc. Solid-State Sens., Actuators, Microsyst. Workshop* (pp. 56-59).

[47] Hsu, H. Y., Ohta, A. T., Chiou, P. Y., Jamshidi, A., Neale, S. L., & Wu, M. C. (2010). Phototransistor-based optoelectronic tweezers for dynamic cell manipulation in cell culture media. *Lab on a Chip*, *10*(2), 165-172.

[48] Ohta, A. T., Chiou, P. Y., Han, T. H., Liao, J. C., Bhardwaj, U., McCabe, E. R., ... & Wu, M. C. (2007). Dynamic cell and microparticle control via optoelectronic tweezers. *Journal of Microelectromechanical Systems*, *16*(3), 491-499.

[49] Valley, J. K., NingPei, S., Jamshidi, A., Hsu, H. Y., & Wu, M. C. (2011). A unified platform for optoelectrowetting and optoelectronic tweezers. *Lab on a Chip*, *11*(7), 1292-1297.

[50] Pei, S. N., Valley, J. K., Wang, Y. L., & Wu, M. C. (2015). Distributed circuit model for multi-color light-actuated opto-electrowetting microfluidic device. *Journal of Lightwave Technology*, *33*(16), 3486-3493.

[51] Pollack, M. G., Fair, R. B., & Shenderov, A. D. (2000). Electrowetting-based actuation of liquid droplets for microfluidic applications. *Applied Physics Letters*, *77*(11), 1725-1726.

[52] Cho, S. K., Moon, H., & Kim, C. J. (2003). Creating, transporting, cutting, and merging liquid droplets by electrowetting-based actuation for digital microfluidic circuits. *Journal of Microelectromechanical systems*, *12*(1), 70-80.

[53] Li, J. (2020). Current commercialization status of electrowetting-on-dielectric (EWOD) digital microfluidics. *Lab on a Chip*, *20*(10), 1705-1712.

[54] Shen, H. H., Fan, S. K., Kim, C. J., & Yao, D. J. (2014). EWOD microfluidic systems for biomedical applications. *Microfluidics and Nanofluidics*, *16*(5), 965-987.

[55] Kothamachu, V. B., Zaini, S., & Muffatto, F. (2020). Role of Digital Microfluidics in Enabling Access to Laboratory Automation and Making Biology Programmable. *SLAS TECHNOLOGY: Translating Life Sciences Innovation*, *25*(5), 411-426.

[56] Nguyen, N. T., Wereley, S. T., & Shaegh, S. A. M. (2019). *Fundamentals and applications of microfluidics*. Artech house.

[57] Shih, S. C., Goyal, G., Kim, P. W., Koutsoubelis, N., Keasling, J. D., Adams, P. D., ... & Singh, A. K. (2015). A versatile microfluidic device for automating synthetic biology. *ACS synthetic biology*, *4*(10), 1151-1164.

[58] Nisisako, T., Torii, T., & Higuchi, T. (2002). Droplet formation in a microchannel network. *Lab on a Chip*, *2*(1), 24-26.

[59] Utada, A. S., Lorenceau, E., Link, D. R., Kaplan, P. D., Stone, H. A., & Weitz, D. A. (2005). Monodisperse double emulsions generated from a microcapillary device. Science, 308(5721), 537-541.

[60] Thorsen, T., Roberts, R. W., Arnold, F. H., & Quake, S. R. (2001). Dynamic pattern formation in a vesicle-generating microfluidic device. Physical review letters, 86(18), 4163.

[61] Adamson, D. N., Mustafi, D., Zhang, J. X., Zheng, B., & Ismagilov, R. F. (2006). Production of arrays of chemically distinct nanolitre plugs via repeated splitting in microfluidic devices. *Lab on a Chip*, *6*(9), 1178-1186.

[62] Clausell-Tormos, J., Lieber, D., Baret, J. C., El-Harrak, A., Miller, O. J., Frenz, L., ... & Holtze, C. (2008). Droplet-based microfluidic platforms for the encapsulation

and screening of mammalian cells and multicellular organisms. *Chemistry & biology*, *15*(5), 427-437.

[63] Mazutis, L., Gilbert, J., Ung, W. L., Weitz, D. A., Griffiths, A. D., & Heyman, J. A. (2013). Single-cell analysis and sorting using droplet-based microfluidics. *Nature protocols*, *8*(5), 870-891.

[64] Zhang, H., Chang, H., & Neuzil, P. (2019). DEP-on-a-chip: Dielectrophoresis applied to microfluidic platforms. *Micromachines*, *10*(6), 423.

[65] Pohl, H. A. (1978). *Dielectrophoresis: The behavior of neutral matter in nonuniform electric fields (Cambridge Monographs on physics)*. Cambridge/New York: Cambridge University Press.

[66] Wixforth, A., Strobl, C., Gauer, C., Toegl, A., Scriba, J., & Guttenberg, Z. V. (2004). Acoustic manipulation of small droplets. *Analytical and bioanalytical chemistry*, *379*(7-8), 982-991.

[67] Leibacher, I., Reichert, P., & Dual, J. (2015). Microfluidic droplet handling by bulk acoustic wave (BAW) acoustophoresis. *Lab on a Chip*, *15*(13), 2896-2905.

[68] Franke, T., Abate, A. R., Weitz, D. A., & Wixforth, A. (2009). Surface acoustic wave (SAW) directed droplet flow in microfluidics for PDMS devices. *Lab on a Chip*, *9*(18), 2625-2627.

[69] Tsuchiya, H., Okochi, M., Nagao, N., Shikida, M., & Honda, H. (2008). On-chip polymerase chain reaction microdevice employing a magnetic droplet-manipulation system. *Sensors and Actuators B: Chemical*, *130*(2), 583-588.

[70] Gijs, M. A. (2004). Magnetic bead handling on-chip: new opportunities for analytical applications. *Microfluidics and nanofluidics*, *1*(1), 22-40.

[71] Mousa, N. A., Jebrail, M. J., Yang, H., Abdelgawad, M., Metalnikov, P., Chen, J., ... & Casper, R. F. (2009). Droplet-scale estrogen assays in breast tissue, blood, and serum. *Science Translational Medicine*, *1*(1), 1ra2-1ra2.

[72] Abdelgawad, M., & Wheeler, A. R. (2009). The digital revolution: a new paradigm for microfluidics. *Advanced Materials*, *21*(8), 920-925.

[73] Teh, S. Y., Lin, R., Hung, L. H., & Lee, A. P. (2008). Droplet microfluidics. *Lab on a Chip*, *8*(2), 198-220.

[74] Abdelgawad, M., & Wheeler, A. R. (2009). The digital revolution: a new paradigm for microfluidics. *Advanced Materials*, *21*(8), 920-925.

[75] Cho, S. K., Moon, H., & Kim, C. J. (2003). Creating, transporting, cutting, and merging liquid droplets by electrowetting-based actuation for digital microfluidic circuits. *Journal of Microelectromechanical systems*, *12*(1), 70-80.

[76] Moon, H., Cho, S. K., Garrell, R. L., & Kim, C. J. C. (2002). Low voltage electrowetting-on-dielectric. *Journal of applied physics*, *92*(7), 4080-4087.

[77] Yi, U. C., & Kim, C. J. (2006). Characterization of electrowetting actuation on addressable single-side coplanar electrodes. *Journal of Micromechanics and Microengineering*, *16*(10), 2053.

[78] Pollack, M. G., Shenderov, A. D., & Fair, R. B. (2002). Electrowetting-based actuation of droplets for integrated microfluidics. *Lab on a Chip*, *2*(2), 96-101.

[79] Yi, U. C., & Kim, C. J. (2006). Characterization of electrowetting actuation on addressable single-side coplanar electrodes. *Journal of Micromechanics and Microengineering*, *16*(10), 2053.

[80] Wheeler, A. R. (2008). Putting electrowetting to work. *Science*, *322*(5901), 539-540.

[81] Rival, A., Jary, D., Delattre, C., Fouillet, Y., Castellan, G., Bellemin-Comte, A., & Gidrol, X. (2014). An EWOD-based microfluidic chip for single-cell isolation, mRNA purification and subsequent multiplex qPCR. *Lab on a Chip*, *14*(19), 3739-3749.

[82] Chang, J. H., Kim, D. S., & Pak, J. J. (2011). Simplified ground-type single-plate electrowetting device for droplet transport. *Journal of Electrical Engineering & Technology*, *6*(3), 402-407.

[83] Yuan, Y., & Lee, T. R. (2013). Contact angle and wetting properties. In *Surface science techniques* (pp. 3-34). Springer, Berlin, Heidelberg.

[84] Young, T. (1805). III. An essay on the cohesion of fluids. *Philosophical transactions of the royal society of London*, (95), 65-87.

[85] Lippmann, G. (1875). *Relations entre les phénomènes électriques et capillaires* (Doctoral dissertation, Gauthier-Villars).

[86] Mugele, F., & Baret, J. C. (2005). Electrowetting: from basics to applications. *Journal of physics: condensed matter*, *17*(28), R705.

[87] Baird, E., Young, P., & Mohseni, K. (2007). Electrostatic force calculation for an EWOD-actuated droplet. *Microfluidics and Nanofluidics*, *3*(6), 635-644.

[88] Li, Y., Parkes, W., Haworth, L. I., Stokes, A. A., Muir, K. R., Li, P., ... & Walton, A. J. (2008). Anodic Ta2O5 for CMOS compatible low voltage electrowetting-on-dielectric device fabrication. *Solid-State Electronics*, *52*(9), 1382-1387.

[89] Chang, J. H., Choi, D. Y., Han, S., & Pak, J. J. (2010). Driving characteristics of the electrowetting-on-dielectric device using atomic-layer-deposited aluminum oxide as the dielectric. *Microfluidics and Nanofluidics*, *8*(2), 269-273.

[90] Lin, Y. Y., Evans, R. D., Welch, E., Hsu, B. N., Madison, A. C., & Fair, R. B. (2010). Low voltage electrowetting-on-dielectric platform using multi-layer insulators. *Sensors and Actuators B: Chemical*, *150*(1), 465-470.

[91] Mazutis, L., Gilbert, J., Ung, W. L., Weitz, D. A., Griffiths, A. D., & Heyman, J. A. (2013). Single-cell analysis and sorting using droplet-based microfluidics. *Nature protocols*, *8*(5), 870-891.

[92] Köster, S., Angile, F. E., Duan, H., Agresti, J. J., Wintner, A., Schmitz, C., ... & Weitz, D. A. (2008). Drop-based microfluidic devices for encapsulation of single cells. *Lab on a Chip*, *8*(7), 1110-1115.

[93] Mousa, N. A., Jebrail, M. J., Yang, H., Abdelgawad, M., Metalnikov, P., Chen, J., ... & Casper, R. F. (2009). Droplet-scale estrogen assays in breast tissue, blood, and serum. *Science Translational Medicine*, *1*(1), 1ra2-1ra2.

[94] Clausell-Tormos, J., Lieber, D., Baret, J. C., El-Harrak, A., Miller, O. J., Frenz, L., ... & Holtze, C. (2008). Droplet-based microfluidic platforms for the encapsulation and screening of mammalian cells and multicellular organisms. *Chemistry & biology*, *15*(5), 427-437.

[95] Srinivasan, V., Pamula, V. K., & Fair, R. B. (2004). Droplet-based microfluidic lab-on-a-chip for glucose detection. *Analytica Chimica Acta*, *507*(1), 145-150.

[96] Hua, Z., Rouse, J. L., Eckhardt, A. E., Srinivasan, V., Pamula, V. K., Schell, W. A., ... & Pollack, M. G. (2010). Multiplexed real-time polymerase chain reaction on a digital microfluidic platform. *Analytical chemistry*, *82*(6), 2310-2316.

[97] Chang, Y. H., Lee, G. B., Huang, F. C., Chen, Y. Y., & Lin, J. L. (2006). Integrated polymerase chain reaction chips utilizing digital microfluidics. *Biomedical microdevices*, *8*(3), 215-225.

[98] Wheeler, A. R., Moon, H., Bird, C. A., Ogorzalek Loo, R. R., Kim, C. J. C., Loo, J. A., & Garrell, R. L. (2005). Digital microfluidics with in-line sample purification for proteomics analyses with MALDI-MS. *Analytical Chemistry*, *77*(2), 534-540.

[99] Barbulovic-Nad, I., Au, S. H., & Wheeler, A. R. (2010). A microfluidic platform for complete mammalian cell culture. *Lab on a Chip*, *10*(12), 1536-1542.

[100] Köster, S., Angile, F. E., Duan, H., Agresti, J. J., Wintner, A., Schmitz, C., ... & Weitz, D. A. (2008). Drop-based microfluidic devices for encapsulation of single cells. *Lab on a Chip*, *8*(7), 1110-1115.

[101] Wang, Y., Zhao, Y., & Cho, S. K. (2007). Efficient in-droplet separation of magnetic particles for digital microfluidics. *Journal of Micromechanics and Microengineering*, *17*(10), 2148.

[102] Shen, H. H., Fan, S. K., Kim, C. J., & Yao, D. J. (2014). EWOD microfluidic systems for biomedical applications. *Microfluidics and Nanofluidics*, *16*(5), 965-987.

[103] Tsuchiya, H., Okochi, M., Nagao, N., Shikida, M., & Honda, H. (2008). On-chip polymerase chain reaction microdevice employing a magnetic droplet-manipulation system. *Sensors and Actuators B: Chemical*, *130*(2), 583-588.

[104] Fair, R. B., Khlystov, A., Srinivasan, V., Pamula, V. K., & Weaver, K. N. (2004, December). Integrated chemical/biochemical sample collection, pre-concentration, and analysis on a digital microfluidic lab-on-a-chip platform. In *Lab-on-a-chip: platforms, devices, and applications* (Vol. 5591, pp. 113-124). International Society for Optics and Photonics.

[105] Chuang, H. S., Kumar, A., & Wereley, S. T. (2008). Open optoelectrowetting droplet actuation. *Applied Physics Letters*, *93*(6), 064104.

[106] Park, S. Y., Teitell, M. A., & Chiou, E. P. (2010). Single-sided continuous optoelectrowetting (SCOEW) for droplet manipulation with light patterns. *Lab on a Chip*, *10*(13), 1655-1661.

[107] Luk, V. N., Mo, G. C., & Wheeler, A. R. (2008). Pluronic additives: a solution to sticky problems in digital microfluidics. *Langmuir*, *24*(12), 6382-6389.

[108] Shih, S. C., Gach, P. C., Sustarich, J., Simmons, B. A., Adams, P. D., Singh, S., & Singh, A. K. (2015). A droplet-to-digital (D2D) microfluidic device for single cell assays. *Lab on a Chip*, *15*(1), 225-236.

[109] Ahmadi, F., Samlali, K., Vo, P. Q., & Shih, S. C. (2019). An integrated droplet-digital microfluidic system for on-demand droplet creation, mixing, incubation, and sorting. *Lab on a Chip*, *19*(3), 524-535.

[110] Mazutis, L., Gilbert, J., Ung, W. L., Weitz, D. A., Griffiths, A. D., & Heyman, J. A. (2013). Single-cell analysis and sorting using droplet-based microfluidics. *Nature protocols*, *8*(5), 870-891.

[111] Wu, H., Li, H., Umar, A., Wang, Y., & Zhou, G. (2018). Bifunction-Integrated Dielectric Nanolayers of Fluoropolymers with Electrowetting Effects. *Materials*, *11*(12), 2474.

[112] Berry, S., Kedzierski, J., & Abedian, B. (2007). Irreversible electrowetting on thin fluoropolymer films. *Langmuir*, *23*(24), 12429-12435.

[113] Koo, B., & Kim, C. J. (2013). Evaluation of repeated electrowetting on three different fluoropolymer top coatings. *Journal of Micromechanics and Microengineering*, *23*(6), 067002.

[114] Chae, J. B., Kwon, J. O., Yang, J. S., Kim, D., Rhee, K., & Chung, S. K. (2014). Optimum thickness of hydrophobic layer for operating voltage reduction in EWOD systems. *Sensors and Actuators A: Physical*, *215*, 8-16.

[115] Berge, B. (1993). Electrocapillarity and wetting of insulator films by water. *Comptes Rendus De L Academie Des Sciences Serie Ii*, *317*(2), 157-163.

[116] Wu, H., Hayes, R. A., Li, F., Henzen, A., Shui, L., & Zhou, G. (2018). Influence of fluoropolymer surface wettability on electrowetting display performance. *Displays*, *53*, 47-53.

[117] Bahadur, V., & Garimella, S. V. (2006). An energy-based model for electrowetting-induced droplet actuation. *Journal of Micromechanics and Microengineering*, *16*(8), 1494.

[118] [Main components of a basic set-up for ink-jet dispensing] Microfab Technologies Inc. http://www.microfab.com/images/stories/BasicSetup/BasicSetup_Components.jpg

[119] Wang, Y. B., Huang, J. H., Lee, M. S., Huang, C. Y., Huang, C. S., Yamashita, I., ... & Hsu, W. (2017). An EWOD-based micro diluter with high flexibility on dilution ratio. *Microsystem Technologies*, *23*(8), 3645-3651.

[120] Gong, J. (2008). All-electronic droplet generation on-chip with real-time feedback control for EWOD digital microfluidics. *Lab on a Chip*, *8*(6), 898-906.

[121] Park, S., Wijethunga, P. A., Moon, H., & Han, B. (2011). On-chip characterization of cryoprotective agent mixtures using an EWOD-based digital microfluidic device. *Lab on a Chip*, *11*(13), 2212-2221.